

DEVELOPMENT AND APPLICATION OF REACTIVE POTENTIALS FOR THE  
ATOMISTIC SIMULATION OF MATERIAL SURFACES AND INTERFACES

By

BRYCE D. DEVINE

A DISSERTATION PRESENTED TO THE GRADUATE SCHOOL  
OF THE UNIVERSITY OF FLORIDA IN PARTIAL FULFILLMENT  
OF THE REQUIREMENTS FOR THE DEGREE OF  
DOCTOR OF PHILOSOPHY

UNIVERSITY OF FLORIDA

2010

© 2010 Bryce D. Devine

To Jocelyn

## ACKNOWLEDGMENTS

In an article describing potential development, Prof. Don Brenner states that this sort of work takes a person with peculiar perseverance. However, from my perspective, that is not necessarily true. What it takes is someone optimistically naïve enough to begin in the first place and who is supported and nurtured by those with a peculiar sort of patience. I could not imagine completing this work and my studies without the constant and blessed support of my wife, Jocelyn. Through this time, I have had the encouragement of new solutions and to keep me motivated Jocelyn had no such encouragement. Only a withering promise that I will finish this soon and yet her support has not wavered. In the end this work is ours together. Any achievement is Jocelyn's as much as mine. Gratitude and accolades can not begin to recompense what she has given for me. Perhaps the best I can do is promise to never do anything like this again.

Along with Jocelyn, I also tried the patience of my advisor, Prof. Sinnott. This is not a trivial task, for her patience is legendary. Her technical expertise, gift for teaching and constant encouragement were invaluable to this effort. I thank her sincerely for chance to work on these projects within this group. I will cherish and build upon the knowledge I have found here. I also had to good fortune to work with Prof Phillipot, whose expertise and experience were a constant source of new ideas and new directions. Prof. Sinnott and Prof. Phillipot both set a lofty standard of scientific professionalism. The example they provide is inspirational and was as much an asset to this project as their guidance and insight.

Several members of the University of Florida Computational Materials Science Focus Group have helped considerably in this work. Drs. Alan McGaughey, Jianguo Yu and Inkook Jang wrote many of the subroutines upon which I based my code. Coding is

an ungrateful job. They each spent years working through the intricacies of the codes. It is labor for which the only acknowledgement they will receive is an esoteric listing in the source code. Ray Shan has been a tremendous partner in developing these models. Without our daily discussions, I doubt these projects would be finished. Some of this work also could not be finished without the assistance and expertise of Donghwa Lee and Travis Kemper and the suggestions of Dr. Tao Liang to all of whom I am grateful.

Lastly, funding for much of this work was graciously provided by the National Science Foundation and the Department of Defense. All work was performed on the computers operated by the Computational Materials Science Focus Group at the University of Florida. With out this resource and the dedicated graduated student who maintain it, we would accomplish very little.

## TABLE OF CONTENTS

|   | <u>Page</u> |
|---|-------------|
| ACKNOWLEDGMENTS.....  | 4           |
| LIST OF TABLES.....   | 8           |
| LIST OF FIGURES.....  | 10          |
| ABSTRACT .....  | 11          |
| 1 ANALYTICAL POTENTIALS IN COMPUTATIONAL MATERIAL SCIENCE.....  | 14          |
| 1.1 The Promise of Multiphase Atomistic Simulations .....   | 14          |
| 1.2 Analytical Potentials for Multi-Material and Multi-phase Simulations .....  | 16          |
| 1.3 Variable Charge Reactive Potentials .....   | 18          |
| 1.4 An Overview of the Dissertation.....  | 20          |
| 2 THE THEORETICAL FOUNDATION OF CHARGE OPTIMIZED MANY-BODY<br>POTENTIALS .....  | 25          |
| 2.1 The Quantum Mechanics of Inter-Atomic Interactions .....  | 25          |
| 2.2 Wavefunction Theory (WFT).....  | 29          |
| 2.3 Density Functional Theory (DFT) of Inter-Atomic Interactions .....  | 48          |
| 2.4 A Self-Consistent Classical Electrostatic Potential.....  | 57          |
| 3 A MULTILEVEL COMPUTATIONAL ANALYSIS OF FLUOROCARBON<br>POLYATOMIC DEPOSITION ON DIAMOND .....                         | 85          |
| 3.1 The Computational Study of Polyatomic Deposition Reactions .....  | 85          |
| 3.2 Computational Details.....  | 90          |
| 3.3 Simulation Results .....  | 95          |
| 3.4 Discussion of Results.....  | 103         |
| 3.5 Concluding Remarks.....   | 109         |
| 4 METHODOLOGY FOR ATOMISTIC SIMULATIONS OF COPPER OXIDATION<br>USING A CHARGE OPTIMIZED MANY-BODY (COMB) POTENTIAL..... | 116         |
| 4.1 Current Theoretical Models of Copper Oxidation .....  | 116         |
| 4.2 Computational Methodology .....   | 119         |
| 4.3 Potential Parameterization.....   | 121         |
| 4.4 Results and Discussion.....   | 125         |
| 4.5 Concluding Remarks.....   | 136         |
| 5 CHARGE OPTIMIZED POTENTIALS FOR ALUMINUM AND ALUMINUM<br>OXIDE SYSTEMS: SUCCESSES, CHALLENGES AND OPPORTUNITIES.....  | 149         |

|  |            |
|--|------------|
| 5.1 Background and Motivation .....  | 149        |
| 5.2 Challenges with Current Theoretical Models for Alumina .....   | 150        |
| 5.2 Parameterization of the COMB Potential .....   | 155        |
| 5.5 Results and Discussion.....  | 159        |
| 5.5 Concluding Remarks.....  | 165        |
| <b>6 CURRENT CAPABILITIES AND FUTURE POSSIBILITIES OF CHARGE<br/>OPTIMIZED MANY BODY POTENTIALS.....</b> | <b>179</b> |
| 6.1 The COMB Code .....  | 183        |
| 6.2 The Fitting Problem.....   | 185        |
| 6.3 Future Applications .....  | 186        |
| LIST OF REFERENCES .....   | 188        |
| BIOGRAPHICAL SKETCH.....   | 198        |

## LIST OF TABLES

| <u>Table</u>   | <u>page</u> |
|--|-------------|
| 3-1 Geometric parameters for CF <sub>2-3</sub> radicals and cations. ....                      | 113         |
| 3-2 Classical MD predicted reactions between CF <sub>3</sub> and diamond (111).....            | 113         |
| 3-3 DFT-MD predicted reactions between CF <sub>3</sub> and the diamond (111) .....             | 113         |
| 3-4 Reaction enthalpies (in eV) between CF <sub>3</sub> and adamantane (C <sub>10</sub> )..... | 114         |
| 3-5 Reaction enthalpies (in eV) between CF <sub>3</sub> and C <sub>22</sub> .....              | 115         |
| 3-6 Reaction enthalpies (in eV) between CF <sub>3</sub> and a periodic diamond slab. ....      | 115         |
| 4-1 Atomic and electrostatic potential parameters.....   | 144         |
| 4-2 Bond dependent potential parameters.....   | 144         |
| 4-3 Coefficients for Legendre polynomials.....   | 145         |
| 4-4 Properties of metallic copper .....  | 145         |
| 4-5 Ionization potentials and electron affinities (in eV) for Cu and O .....                   | 146         |
| 4-6 Properties of molecular oxygen .....   | 146         |
| 4-7 Properties of Cu <sub>2</sub> O (Cuprous Oxide) .....                                      | 147         |
| 4-8 Properties of monoclinic CuO .....   | 147         |
| 4-9 $\Delta H_f$ (in eV) of copper oxides .....  | 148         |
| 4-10 $\Delta H_{Ads}$ (in eV) of O <sub>2</sub> on Cu(100) surface .....                       | 148         |
| 5-1 Atomic and electrostatic potential parameters.....   | 174         |
| 5-2 Interaction dependent potential parameters .....   | 174         |
| 5-3 Coefficients for Legendre polynomials.....   | 175         |
| 5-4 Properties of metallic aluminum.....   | 176         |
| 5-5 Ionization potentials and electron affinities (in eV) for Al and O .....                   | 177         |
| 5-6 Properties of $\alpha$ -Al <sub>2</sub> O <sub>3</sub> .....                               | 177         |

5-7 Interfacial separation distance,  $D_o$  (in Å) and  $W_{sep}$  (in  $\text{J}\cdot\text{m}^{-2}$ )..... 178

## LIST OF FIGURES

| <u>Figure</u>   | <u>page</u> |
|---|-------------|
| 1-1 Si nano-cluster in amorphous SiO <sub>2</sub> . .....                         | 23          |
| 1-2 “The Modeler’s Toolbox” .....   | 24          |
| 2-1 The interaction energy between two charged atoms. ....                        | 83          |
| 2-2 Self energy functions for O and Cu.....                                       | 84          |
| 3-1 Target systems are used for calculation of reaction enthalpies .....          | 111         |
| 3-2 Impact sites on the diamond(111) surface.....                                 | 112         |
| 3-3 The geometry of the transition state .....                                    | 112         |
| 4-1 Crystal structures for the two low energy oxide phases.....                   | 137         |
| 4-2 Surface charge in metallic copper.. ....                                      | 137         |
| 4-3 The bond dissociation energy of O <sub>2</sub> anions. ....                   | 138         |
| 4-4 The energy per unit volume of the three low energy phases .....               | 139         |
| 4-5 O <sub>2</sub> is placed on the Cu(100) surface in the six orientations ..... | 140         |
| 4-6 The relaxed reconstructed Cu(100) surface. ....                               | 141         |
| 4-7 The Cu <sub>2</sub> O(111)  Cu(100) interface.....                            | 142         |
| 4-8 Planar average charge density .....   | 143         |
| 5-1 The crystal structure of $\alpha$ -Al <sub>2</sub> O <sub>3</sub> (A) .....   | 167         |
| 5-2 The Al-O-Al bond angle distribution in corundum .....                         | 168         |
| 5-3 The energy vs. volume of several aluminum oxide phases. ....                  | 169         |
| 5-4 A closed packed plane of Al atoms.....  | 170         |
| 5-5 A second layer of Al atoms in the FCC metal .....                             | 171         |
| 5-6 The interfaces with the highest (A) and lowest (B) values .....               | 172         |
| 5-7 The charge density (blue line) and separation distance .....                  | 173         |

Abstract of Dissertation Presented to the Graduate School  
of the University of Florida in Partial Fulfillment of the  
Requirements for the Degree of Doctor of Philosophy

DEVELOPMENT AND APPLICATION OF REACTIVE POTENTIALS FOR THE  
ATOMISTIC SIMULATION OF MATERIAL SURFACES AND INTERFACES

By

Bryce D. Devine

December 2010

Chair: Susan Sinnott

Major: Materials Science and Engineering

Interest in atomic scale computational simulations of multiphase systems has grown substantially in recent years as our ability to simulate multi-million atom systems has become commonplace. The main limitation is now the lack of a theoretical framework that can smoothly model atoms in dissimilar bonding conditions such as across a metal-metal oxide interface. Recently developed charge optimized many body potential (COMB) have addressed several of the technical challenges to atomistic simulations of systems composed of multiple phase and multiple materials interacting together.

The COMB formalism merges variable charge electrostatic interactions with a bond order potential that has the capacity to adaptively model metallic, covalent and ionic bonding in the same simulation cell. Presented here is the development of an inter-atomic COMB potential energy function from its basis in quantum mechanics up through its adaptation and parameterization for two challenging simulation problems: the oxidation and oxide island formation on copper surfaces and the aluminum-aluminum oxide interface. In theory, COMB is an analytical extension of tight binding theory to a fully classical determination of inter-atomic interactions. In practice, it is

found that several empirically derived functions are also necessary to adapt the potential to systems of interest. In this work, these additional functions are chosen to replicate interactions that are lost in the approximations made in the derivation of the COMB potential. The resulting COMB formalism accurately reproduces key observables in both materials such as mechanical properties, phase order, formation enthalpies, surface energies, and defect formation enthalpies. The performance of the potentials indicates that the COMB potential holds significant promise in extending our abilities to simulate multiphase systems.

Molecular dynamics simulations of the oxidation of the Cu (100) surface using the COMB potential reveal a fairly low occurrence of reactions. Single point calculations of O<sub>2</sub> on this surface predict that molecular dissociation only occurs when both O atoms are close to adjacent four fold hollow sites. The molecule dissociates to form a c(2x2) surface at low temperature and low oxygen coverage. At room temperature and with higher coverage, the surface reconstructs to a missing row  $(\sqrt{2} \times 2\sqrt{2})R45^\circ$  configuration. These findings are consistent with experimental observations.

Similarly COMB based molecular dynamics simulations of variations of crystalline Al(111)|Al<sub>2</sub>O<sub>3</sub>(0001) interfaces predict atomically sharp interfaces that are stable through the melting of the Al metal. The potential does not clearly distinguish differences in interfacial adhesion with different orientations of the metal to the oxide. This is inconsistent with first principles calculations and warrants further investigation.

One consideration with advances in computational power and improved algorithms is first principles based methods may be adequate to model multiphase systems. This possibility is explored through a multilevel study of fluorocarbon

deposition on diamond using both classical molecular dynamics (MD) using the reactive empirical bond order potential (REBO) and density functional theory based MD (DFT-MD). The comparison highlights that classical methods are still several orders of magnitude more efficient than current DFT methods, thus yielding better statistics, but DFT models are more reliable in their predictions. In this study, it is found that  $\text{CF}_3$  and  $\text{CF}_3^+$  react differently when deposited with energy of 50 eV. It is also found that  $\text{CF}_3$  can add directly to the hydrogen terminated diamond surface when coupled with the simultaneous evolution of HF. The single step addition reaction is only predicted with DFT due to short interaction distances in REBO. The results strongly suggest an improved REBO potential that includes charge optimized electrostatic interactions and better represents the long interaction distances in key transition states would greatly benefit our understanding of this commercially relevant process.

CHAPTER 1  
ANALYTICAL POTENTIALS IN COMPUTATIONAL MATERIAL SCIENCE

**1.1 The Promise of Multiphase Atomistic Simulations**

As engineering progresses at the nanometer length scale, computational simulations are finding an increasingly significant role in the design and optimization of new electronic and mechanical devices. This is due in part to the confluence of two favorable trends. First, as the size of devices decreases, the total number of atoms in the structure is reduced. In a nano-scale device, the total number of atoms is on the order of tens of millions to billions. At the same time, with the relentlessly consistent year over year increase in computer performance, it now fairly routine to conduct entirely atomistic simulations on systems composed of tens on millions of atoms. Multibillion atom simulations are possible on the current generation of the most powerful supercomputers. If we hold to our current course of progress, in a relatively short time life-size simulations of entire nano-devices will become routine rather than leading edge.

While increases in computer power expands the accessible length scale across all levels of theory, the bulk of computational work for life-size systems defaults to empirical atomistic methods in which interactions between all atoms in the systems are explicitly described with classical Newtonian mechanics. Such methods are highly efficient yet provide atomic scale detail regarding the structure and energies of critical features, such as interfaces, and the atomic scale processes that affect material performance throughout the device. In reality, inter-atomic interactions are best described with quantum mechanics based methods that consider all electrons in the systems. Quantum-based methods are generally regarded to be more accurate with a

higher degree of reliability in their predictions than atomistic potential. However, electronic structure calculations are limited by their computational demand to systems of just a few thousand atoms. At the other end of the length scale in materials simulations are meso-scale methods which look at materials properties at the micro-scale. Such methods lack the atomic scale detail that is highly valuable to materials selection and optimization at the nano-scale.

To illustrate this point, Figure 1-1 shows an image from an atomistic simulation of a silicon nano-cluster embedded in an amorphous silica matrix. The colors correspond to the coordination of the individual atoms. Normally coordinated atoms in the silica matrix are not visible for clarity. It has been discovered recently that systems with nano-clusters such as this exhibit several intriguing optical properties including the ability to emit light<sup>1-3</sup>. While the commercial significance of a source of solid state lighting made from some of the cheapest and most abundant materials on earth is easily appreciated, the technological barriers to developing a commercially viable device are huge and quite daunting. As it is currently, there is no clear agreement on how emission occurs in the material. One school of thought proposes quantum confinement effects within the cluster or at the surface give rise to emission<sup>4-6</sup>, while others attribute it to under-coordinated defects at the interface and within the amorphous matrix<sup>7-9</sup>. It is nearly impossible to answer the question solely through experimentation. There is currently no reliable experimental technique that can resolve phenomena at buried interfaces at the atomic scale in situ. Unfortunately, the system is quite challenging for theoretical methods as well. The nano-cluster in Figure 1-1 is 4 nm in diameter which is a realistic size for the material. The simulation cell contains ~60,000 atoms between the cluster

and the matrix. The system size is minimal for a cluster of that size, yet the system is nearly 6 times larger than what can be studied through quantum based methods. Continuum based models lack the atomic scale detail necessary to answer the critical questions such as what is the structure and coordination at the interface. The ideal method to study this system is an atomistic analytical potential designed to model both phases simultaneously.

Naturally, life-size atomistic simulations of any device most likely involve multiple interfaces. In most cases, such simulations include a surface, which is at least an interface between a solid and a vacuum. More realistically, devices are multifunctional and involve the integration of several materials that contribute different functionality to the overall operation. Therein lays the crux with the present state-of-the-art of atomistic simulations. Currently, what is lacking is a theoretical methodology that can simultaneously model multiple phases and all types of chemical bonding: ionic, covalent, metallic and van der Waals interactions.

## **1.2 Analytical Potentials for Multi-Material and Multi-phase Simulations**

In this dissertation, the classical methodology that describes inter-atomic interactions is called a potential as is the convention of materials scientists and solid state physicists; in molecular systems, the methodology is conventionally referred to as a force field. While describing molecular interactions is a goal of this work, the majority of the systems we seek to model are in the solid state and so I will stick with the conventions of the solid-state community.

Typically a potential is designed and parameterized to describe one type of chemical bonding. Over time, this has led to several categorizations of potentials based on the type of material for which they are applicable: Buckingham for ionic

materials,<sup>10</sup> Tersoff potentials for covalent bonding<sup>11, 12</sup> or the Embedded Atom Method (EAM) for metallic systems<sup>13</sup> are well documented examples. The obvious limitation with this scheme of development is that none of these methods can seamlessly model several bonding environments, such as what occurs in a heterogeneous interface between dissimilar materials.

Recently, this limitation has been breached by several advances in potential development. While the goal of a universal method applicable to all bond types has not yet been realized, significant progress has been made based on two key developments. The first is a rather new class of models called variable charge potentials in which the partial charges of individual atoms are not fixed but instead are determined in a self-consistent manner based on the principle of electronegativity equilibration (Qeq).<sup>14</sup> Essentially, variable charge potentials describe the electrostatic interactions between atoms as a balance between the Coulombic interaction between charge and the cost to form a charge on an atom. This allows for the simultaneous handling of an atom in various oxidation states within the same classical simulation.

Examples in the literature can be found that apply Qeq type electrostatic schemes to all bond types depending on the type of short range potential with which the scheme is coupled.<sup>15-20</sup> The Qeq methods describe only the electrostatic portion of the total energy in a system and must be added to a non-electrostatic potential to describe short range contributions to the total energy. For example, Streitz and Mintmire coupled a Qeq scheme to a Finnis-Sinclair<sup>21</sup> potential for metals to model aluminum/alumina interfaces.<sup>22</sup> Recently, bond order type potentials<sup>23</sup> and especially reactive bond order potentials<sup>16, 24, 25</sup> that describe bond breaking and new bond formation in covalent

materials, have been shown to have the flexibility to model several bond types from metallic to purely covalent with varying degrees of covalency in between. This is demonstrated by the work of Iwaski<sup>15</sup> and later Yu *et al.*<sup>18</sup> who applied a Tersoff type bond order potential to various transition metals. Coupling of a Qeq electrostatic scheme with a bond order potential provides a means to extend the method to ionic type bonding. Such an approach was developed by Yasukawa<sup>17</sup> who paired Qeq with a Tersoff potential. More recently Yu *et al.* developed their charge optimized many body (COMB) formalism based on the work of Yasukawa.<sup>18</sup> The initial version of COMB fixed a few instabilities in the Yasukawa's potential. More recently, Shan *et al.* corrected a few of the instabilities in the original COMB formalism.<sup>26</sup> In particular, they parameterized a version of the potential for hafnium and the various phases of hafnium oxide, which, due to their complex crystallography, are difficult materials to simulate.<sup>26</sup>

Recently an article by Phillpot and Sinnott discussed the promise of variable charge bond order potentials for multiphase simulations.<sup>26</sup> The capabilities that this approach offers materials modelers is illustrated in Figure 1-2, which is published in that article. The figure presents the three main bonding types to which most current potentials are limited: metallic, ionic and covalent, and the technological problems we can address with a multiphase atomistic potential.

### **1.3 Variable Charge Reactive Potentials**

In addition to the extensibility to new materials systems, variable charge potentials offer several advantages over traditional atomistic potentials in cases where bonds are broken and formed. Currently the main application of reactive potential is for hydrocarbon system where the reactive empirical bond order potential (REBO) has been used extensively.<sup>24, 25</sup> REBO is an extension of the Tersoff potential<sup>11, 12</sup> designed

to model bond breaking in hydrocarbon systems. The main limitation of REBO is its lack of a description for electrostatic interactions which restricts its use to charge neutral covalently bound systems. The ReaxFF force field is another reactive potential based on an extended Tersoff formalism that was originally designed for hydrocarbon systems.<sup>16</sup> ReaxFF includes variable charge electrostatics and has been extended to both metallic and ionic systems.<sup>19</sup> The main limitation with ReaxFF is its scalability, which limits its practical application to systems with just a few thousand atoms. However, the success of ReaxFF in modeling mixed bond states further supports the concept of combining variable charge electrostatics with a bond order potential to develop a multiphase potential.

Reactive potentials are often noted for their efficiency which is often the first consideration in choosing an atomistic level of theory. Variable charge techniques add several key characteristics to extend the applicability of reactive potentials, the first and foremost of which is the ability to model various oxidation states. Take, for example, an ionic system described with a fixed charge model. In such a scheme, each atom has a set charge regardless of the local environment in which it exists. The charge is the same whether an atom is bound in the solid, at the surface or liberated to infinite distance. In a fixed charged ionic model, the energy to completely atomize the system is actually the ionization energy defined as the energy required for break the material into infinitely separated ions. The more chemically meaningful measure is the enthalpy of formation, which is the energy difference between the final material and its constitutive elements in their standard reference states. The enthalpy of formation is unobtainable from a fixed charge potential since the standard reference states for

elements are charge neutral. A variable charge potential is the only atomistic method capable of calculating formation enthalpies relative to the standard reference state in ionic materials.

The other main application for empirical methods is in cases where higher fidelity methods are not applicable. In computational materials science, the most frequently applied quantum mechanics based methodology is Kohn-Sham density functional theory (DFT),<sup>27, 28</sup> which is especially well suited for metals and heavier atoms in the solid state. In several instances, we seek to look at a problem for which DFT is prone to error. Bond dissociation is a typical example where static correlation effects, which DFT misses<sup>29</sup>, contribute significantly to the total energy at extended bond lengths. An empirical potential can be parameterized to a much higher level of theory that captures such effects and efficiently model larger systems that are not tractable by any other means.

#### **1.4 An Overview of the Dissertation**

The most reliable analytical potentials are derived from the quantum physics that govern chemical bonding. This is the case for most of the generally used potentials for materials simulations such as EAM and Tersoff's bond order. While it is possible to produce a potential based on empirical observations, chance are good that it will have limited applicability beyond what it was parameterized for. The second chapter reviews the quantum physics that describe chemical bonding as it pertains to potential development. A COMB potential formalism is derived through classical approximations to the quantum physics based interatomic interactions. The intent to illustrate the connectivity between the derived classical potential energy function and DFT.

Chapter 3 of this work compares the application of a reactive empirical potential and DFT to the simulation of the deposition reactions on diamond. This is an area of study where atomistic simulations have provided significant insight into the reactions that govern deposition products. The work highlights the strengths and limitations of the various methods and supports the further development of COMB type potentials.

The Chapters 4 and 5 cover the development and application of COMB potentials for two relevant materials problems. Chapter 4 presents a potential designed to model the oxidation of copper and the formation and growth of copper oxide islands on the metallic surface. Metal oxidation is a commercially and technologically significant process for which copper has been a model system.<sup>30-34</sup> More recently, it has been found that the size and shape of nanometer sized oxide islands grown on the copper surface can be influenced by the conditions under which they form.<sup>35-37</sup> The overall goal is that with a bit more insight into the mechanism and physics that govern island formation we can find a means to dictate the size and shape of these nano-scaled structures. To date, the limitation for simulations of these systems has been the lack of an atomistic method to apply to the problem.

Chapter 5 presents a potential for the simulation of aluminum/alumina interfaces. Due to its technological significance, this material system has been the subject of several development efforts.<sup>36, 38, 39</sup> Many potentials fail to predict the correct ground state crystal structure of  $\alpha$ -alumina, which limits their reliability in predicting interfacial structures. There are currently two potentials that predict the corundum structure as the ground state. The ReaxFF formalism has been adapted to the aluminum and alumina.<sup>40</sup> The scalability limitations of ReaxFF limit its use to small interfacial systems. The other

model is the compressible ion model (CIM)<sup>41</sup>, which includes the polarization effects that are believed to stabilize the corundum structure.<sup>39</sup> However, the model does not include variable charges, which precludes its use from interfacial simulations.

The Chapter 6 summarizes the current state of the art COMB potentials and the areas for future development. This is an ongoing and active research with several projects seeking to extend the parameterization to more complicated system, such as hydrocarbons and rare earth oxides. The intent is to close with a summary of finding and a review of the tools that have been developed to assist in these efforts.

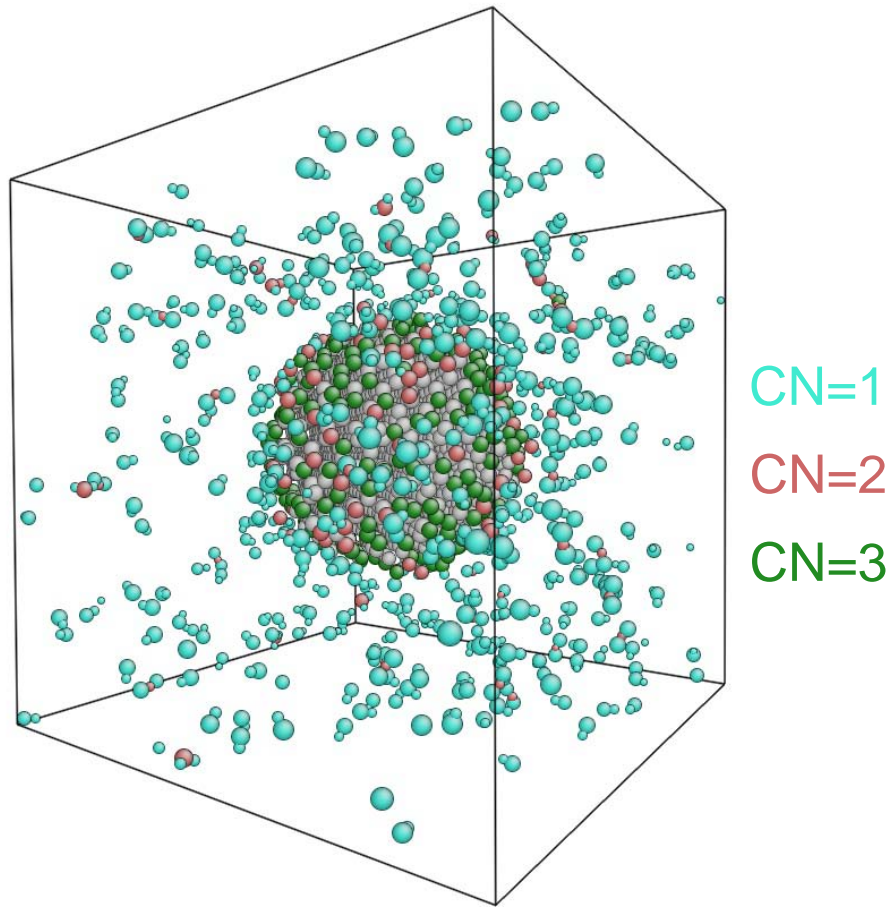


Figure 1-1. Si nano-cluster in amorphous  $\text{SiO}_2$ . This snapshot from an atomistic simulation shows the interface Si nano-cluster embedded in amorphous  $\text{SiO}_2$ . Atoms are colored based on coordination number (CN). Normally coordinated atoms are not visible.

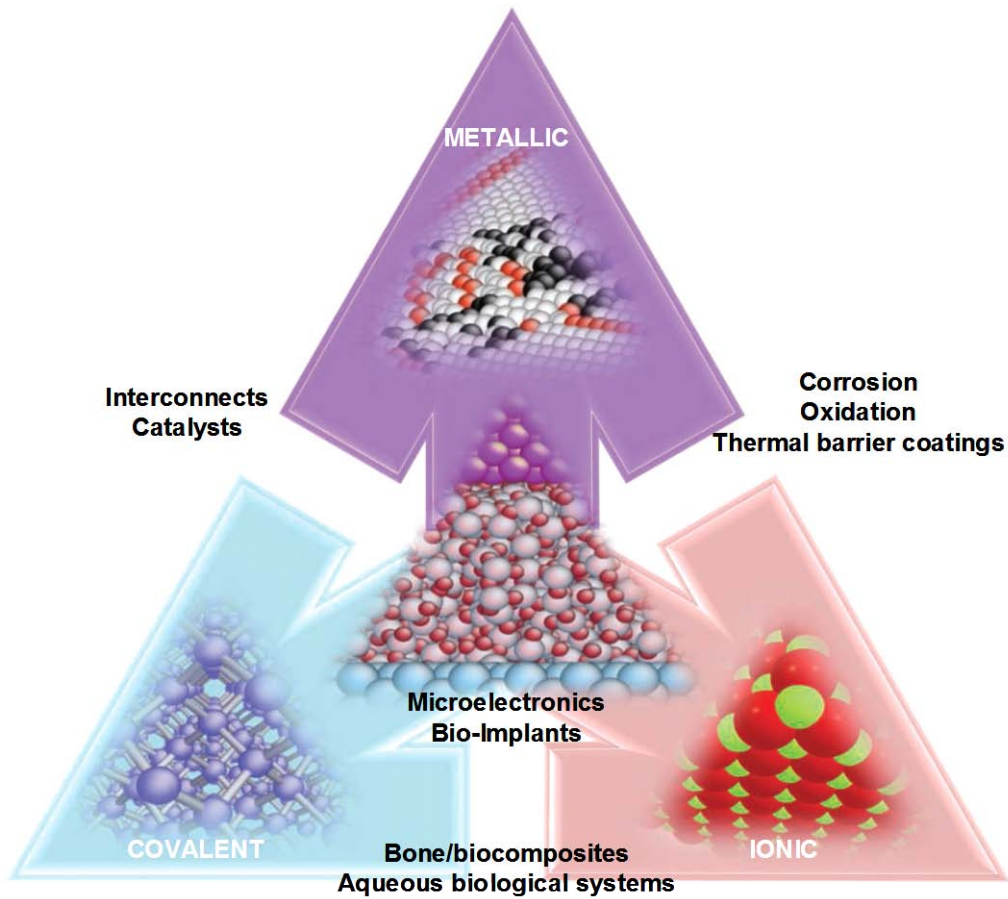


Figure 1-2. "The Modeler's Toolbox" as describe by Sinnott and Phillpot in a recently published article discussing simulations of multiple material systems. The image illustrates the technical problems that can be addressed with a potential, such as COMB, that has the capability of modeling more than one bond type. Reprinted with permission from S. R. Phillpot and S. B. Sinnott, *Science* **325**, 1634 (2009).

## CHAPTER 2 THE THEORETICAL FOUNDATION OF CHARGE OPTIMIZED MANY-BODY POTENTIALS

### 2.1 The Quantum Mechanics of Inter-Atomic Interactions

A main goal of the work with COMB is to develop a potential formalism with the flexibility to model dissimilar materials and with the transferability to describe the varying bonding environments simultaneously. The most promising approach to accomplish that objective is to begin with a potential that is derived by making classical approximations to the quantum physics involved in inter-atomic interactions. This is essentially how Abell and Pettifor derived their respective analytical bond order potentials from tight binding density functional theory (TB-DFT).<sup>23, 42</sup> This style of potential is perhaps the most flexible formalism in common use today and has been adapted with slight modification to covalently bound semiconductors,<sup>11, 36</sup> hydrocarbons,<sup>16, 24, 25, 43</sup> ionic material<sup>19, 44</sup> and metals.<sup>15, 18</sup> Tersoff's version of the Abell formalism is one of the most reliable potentials for Si and other semiconductors.<sup>11, 12</sup> Brenner built upon the Abell-Tersoff formalism to develop the Reactive Bond Order Potential (REBO)<sup>24</sup> and its second generation<sup>25</sup> for hydrocarbon systems. The reactive term in the name indicates that this potential has the flexibility to model bond breaking in carbon systems. Similarly, the ReaxFF force field, which too is based on Tersoff's model, has been extended to a wide range of materials spanning nearly all regions of the periodic table.<sup>16</sup> Pettifor's analytical bond order formalism was originally developed to distinguish single double and triple bonds as well as radicals in carbon materials<sup>42</sup> but has since been adapted to more complex covalently bound systems such as GaAs and SiC and metals.<sup>35, 36, 45-48</sup> Brenner has shown how the embedded atom methods (EAM) originally designed for metallic systems are algebraically equivalent to Abell's model.<sup>13</sup>

Recent versions of EAM extend this formalism further to covalent systems such as Si and C.<sup>49, 50</sup> All together, the analytical bond order formalism and its derivatives have been adapted to the most comprehensive list of materials of any current potential formalism.

While the analytical bond order formalism has demonstrated the flexibility to model many systems, historically it has lacked the transferability to simultaneously model several phases. Variable charge schemes address this limitation. The flexibility of the bond order formalism is attributable to its theoretical origins in DFT.<sup>21, 51</sup> Adding additional electrostatic interactions poses the risk that the additional interactions may compromise the flexibility of the formalism. However, as with the bond order formalism, variable charge schemes are shown here to have a theoretical basis in DFT as well. The coupling of the two methods can be viewed as incorporating a few of the contributions to the bond energy that are disregarded in bond order formalism. In a review of the development of the REBO potential, Brenner proposes that transferability and flexibility are best achieved when a potential replicates the essential quantum physics of chemical bonding.<sup>52</sup> Finnis emphasizes this point in a similar review of Pettifor's bond order formalism and in his book where he derives many of the most effective interatomic potentials from TB-DFT.<sup>21</sup> The coupling of a variable charge electrostatic potential with a bond order potential follows this same approach.

When developing a potential, it is always tempting to add additional functions in an ad hoc manner to correct aberrant predictions or improve the behavior of the potential. While corrections are in most cases unavoidable, they often have unintended consequences and must be chosen with care. In his review, Brenner suggests four

characteristics of effective potentials that must be balanced while developing the functional form of the potential:

**Flexibility:** The potential should be able to reproduce a wide range of materials properties such as cohesive energies, surface energies, defect formation energies, etc.

**Accuracy:** The potential should reproduce the properties in the fitting database within the designed tolerance.

**Transferability:** The parameter set should be applicable to a wide range of bonding environments and other phases of the material.

**Computational Efficiency:** The appeal of empirical potentials over more transferable first principles methods is the speed of the calculations and scalability to larger systems. There is a lower bound on the efficiency of an empirical potential where, if it is nearly as costly as first principles calculation, there is little reason to spend the effort fitting and developing it.

When we add functions to improve performance of the potential for one phase we naturally risk compromising the transferability to other phases. This especially pertinent when designing potentials for interfaces where the parameters must be transferable to several phases in a broad range of coordination environments. Take for example, a graded interface between an oxide and a close-packed metal. In the interface region, coordination ranges from 12 nearest neighbors in the pure metal to substantially less in the stoichiometric oxide. Between these boundaries, in the interface region, there is no constraint on stoichiometry. Furthermore, variable charge electrostatics also lifts any constraint on charge neutrality at the interface; the system as a whole can be constrained to be charge neutral, but in the interface region, non-neutrally charged local

phases may develop. Achieving transferability to all these unusual and unexpected possible phases is a delicate task that requires well chosen functional forms. Success is most likely when the additional functions are chosen to replicate the interactions as described by the underlying quantum physics.

Transferability of a potential also depends on the fitting process. A tempting assumption is that transferability can be achieved solely by fitting to a comprehensive database. While fitting is a critical part of the potential development process, where accuracy and the flexibility to describe a wide range of phases are necessary for reliable results, it is often quite possible to achieve an accurate fit to properties that should be indistinguishable by the potential. A typical example is the ability of an EAM potential to stabilize a face centered cubic (FCC) crystal structure relative to a hexagonal close packed (HCP) arrangement. The physics that an EAM potential describes cannot distinguish between these phases. However, with careful fitting of the cutoff distance, the FCC structure can be stabilized relative to HCP. In such a case, transferability is achieved by fitting a convenient cutoff that selects the interactions that give a decent result rather than accurately describing the energy per interaction. It is doubtful that such a potential will be transferable to the unusual bonding situations that arise at surfaces and interfaces or to the metal-metal interactions in an oxide. The point here is that while fitting is a critical phase of the development, it is possible to fit the correct behavior for the wrong reasons. Transferability is best achieved by beginning with a well designed functional form that replicates the underlying physics and fitting that potential to a well chosen data set.

## 2.2 Wavefunction Theory (WFT)

### 2.2.1 The time independent Schrödinger equation

The simplest description of a material at the quantum level is as a system of non-relativistic electrons acting in response to an external potential  $V_{\text{ext}}$  comprised of the positively charged nuclei. One way to describe the physics of the electrons is through wave mechanics, where properties of the chemical system are described by a wavefunction.<sup>53</sup> Observable properties of the system, such as energy, are found when an appropriately chosen operator acts upon the wavefunction. In the case of non-relativistic electrons, the energy of the system is given by the equation:

$$\hat{H}\psi = E\psi \quad . \quad (2-1)$$

This is the time independent Schrödinger equation in its most basic form. Here  $E$  is the total energy of the system and the wavefunction,  $\psi(r_i, s_i)$  is an eigenfunction of position and spin for each electron in the system. Equation 2-1 is an eigenvalue equation where an operator,  $\hat{H}$  in this case, acts on the wavefunction to yield a scalar eigenvalue,  $E$ .

The Hamiltonian operator in Equation 2-1,  $\hat{H}$ , is the operator that gives the total energy for the system. When written out explicitly the Hamiltonian is:

$$\begin{aligned} \hat{H} = & -\sum_i \frac{\hbar^2}{2m_e} \nabla_i^2 - \sum_I \frac{\hbar^2}{2m_I} \nabla_I^2 - \sum_i \sum_I \frac{e^2 Z_I}{4\pi\epsilon_0 |r_i - R_I|} + \frac{1}{2} \sum_i \sum_{j \neq i} \frac{e^2}{4\pi\epsilon_0 |r_i - r_j|} \\ & + \frac{1}{2} \sum_I \sum_{J \neq I} \frac{e^2 Z_I Z_J}{4\pi\epsilon_0 |R_I - R_J|} \end{aligned} \quad (2-2)$$

where,  $i$  and  $j$  sum over electrons located at position  $r_i \equiv (x_i, y_i, z_i)$ ,  $I$  and  $J$  sum over nuclei at positions  $R_I$ ,  $m_e$  is the mass of an electron,  $m_I$  is the mass of the nuclei,  $Z$  is the atomic number,  $e$  is the charge of one electron,  $\epsilon_0$  is the vacuum permittivity. The term

$\hbar$  is Planck's constant divided by  $2\pi$  and the term  $\nabla^2$  is the Laplacian operator defined in Cartesian coordinates as:

$$\nabla_i^2 = \frac{\partial^2}{\partial x_i^2} + \frac{\partial^2}{\partial y_i^2} + \frac{\partial^2}{\partial z_i^2} . \quad (2-3)$$

The energy operator contains components for both the kinetic and potential energy of the electron and nuclei. The last three terms in Equation 2-2 describe the potential energy and are essentially the same as the classical electrostatic interactions. The factor of  $\frac{1}{2}$  in the last two terms accounts for double counting since the summations run over each interaction twice. At the quantum level, the kinetic energy is not equivalent to its classical analog, but, instead is determined as the eigenvalue of the kinetic energy operator<sup>54</sup>:

$$T = -\frac{\hbar^2}{2m} \nabla^2 . \quad (2-4)$$

The wave function,  $\psi$ , is an obtuse concept. Essentially, it is a mathematical function whose arguments are the positions and spins ( $r,s$ ) of the electrons. The spin,  $s_i$ , introduces two components for the description of each electron, conventionally referred to as  $\alpha(s_i)$  and  $\beta(s_i)$  or rather the “spin up” and “spin down” component for each electron. The main effect from spin is that the wavefunction is anti-symmetric, meaning the wavefunction changes sign when the positions of two electrons are exchanged.<sup>55, 56</sup>

The product of the wavefunction with its complex conjugate,  $(\psi^*\psi)$  represents a probability density. As an eigenfunction,  $\psi$  could be multiplied by any scalar quantity and still return a true solution, thus, giving an infinite number of solutions to Equation 2-1. In practice, the wavefunction is crafted to be orthonormal, meaning the components

are orthogonal to one another and the wavefunction is multiplied by a unique normalization constant that satisfies the condition:

$$\int \psi_i \psi_j dr = \delta_{ij} \quad (2-5)$$

where,  $\delta_{ij}$  is the Kronecker delta function, which is equal to one when  $i=j$  and zero otherwise. Equation 2-5 uses shorthand notation where  $dr$  indicates integration over all spatial components and summation of the spin components,  $s$ . The normalization of the wavefunction leads to a representation of the electron density at any position,  $r_i$ , as:

$$\rho(r_i) = N \int |\psi|^2 dr . \quad (2-6)$$

$N$  in Equation 2-6 is the number of electrons.

### 2.2.2 The Born-Oppenheimer approximation

The complexity Equation 2-2 can be reduced with a few key approximations. First, since in most circumstances the mass of the nuclei are significantly larger than the mass of an electron and the electrons move at a significantly higher velocity than the nuclei, the motion of the nuclei may be neglected when determining the energy of the electrons. This approximation, which is referred to as the Born-Oppenheimer approximation, drops the second and fifth terms from Equation 2-2. With this approximation, the equation yields a total electronic energy,  $E^{el}$ , for the system rather than the actual total energy for the system.<sup>57</sup>

A fundamental hypothesis of quantum mechanics is that there has to exist a lowest energy state for the system called the ground state,  $E_0$ , which is described with the corresponding ground state wavefunction,  $\psi_0$ .<sup>58</sup> If this were not true then an infinitely low energy could be achieved by simply packing the electrons in closer to the nuclei while maintaining the kinetic energy at a constant value. A related approximation, the

adiabatic approximation, assumes that under normal conditions, on the time scale of nuclear motion, electrons relax to the ground state instantaneously.<sup>59</sup> Under the adiabatic approximation, the energy of any arrangement of nuclei can be determined with the ground state configuration of electrons.

The two approximations introduce inconsequential error in most circumstances, yet have several significant ramifications in regards to empirical potentials. Together the two approximations allows us to clearly separate electronic and nuclear motions, which, in turn, allows us to derive an empirical potential for inter-atomic forces based upon the ground state configuration of the electronic structure for any arrangement of nuclei. For any given set of nuclear positions, there is one unique ground state electronic configuration. Consequently a finite difference in energy can be determined for various stresses and perturbations on the system. Without the approximations, any derived potential would be based on a one or several most probable configurations rather than the unique ground state.

The appropriateness of approximation is contingent of course on the definition of normal conditions. In most applications we are concerned with low energy processes around standard conditions. The Born-Oppenheimer approximation sets an upper bound in energies below which it is valid. Processes that involve high nuclear velocities or sufficiently high energies to allow excited electronic states to participate are somewhat spurious. This limitation carries through to any empirical potential derived from the ground state configuration. For most applications involving static calculations or low energy dynamics around standard temperature, the approximation is very reasonable. In computational materials we can run into difficulties when we look at very

high energy processes such as high energy depositions or radiation bombardment in which case results may be unreliable.

The separation of nuclear and electronic motions allows us to simplify the expression of the Hamiltonian in Equation 2-2. First we can drop all nuclear-nuclear interactions from the calculation. Secondly, we can define the potential generated by the field of the positively charged nuclei and all other potentials that are not dependent upon the electrons as an external potential,  $V_{ext}$ :

$$V_{ext}(r) = \sum_I \frac{-Z_I}{|r - R_I|} . \quad (2-7)$$

The external potential and any other potential acting on the electrons can be defined as an operator that gives the expectation value of the electron-nuclear energy contribution to the total electronic energy of the system. The expectation value for the electron-nuclear Coulombic attraction is determined by operating  $\hat{V}_{ext}$  on the wavefunction, pre-multiplying by the complex conjugate of the wavefunction and integrating over all special components:

$$E_{eZ} = \int \psi^* \hat{V}_{ext} \psi dr . \quad (2-8)$$

The interaction can also be described as the interaction between the  $V_{ext}(r)$  and electron density as defined in Equation 2-6 which will be used later:

$$E_{eZ} = \int \rho(r) V_{ext}(r) dr . \quad (2-9)$$

### 2.2.3 The variational principle

If the correct wavefunction is known, then any observable value of the system can be determined by operating on the wavefunction with the appropriate operator. The trick is finding the appropriate wavefunction for the system. To so do, we can exploit

the idea that there exists a lowest energy ground state, which sets a lower bound on any trial solutions. The best solution, therefore, corresponds to the lowest energy, which set up a constrained minimization problem to determine the ground state configuration. This concept, called the variational principle,<sup>60</sup> is an essential concept in most quantum mechanical calculations and is well described in the standard text books. I will use the proof by Cramer to illustrate.<sup>58</sup>

A normalized trial wavefunction,  $\Phi$ , can be expressed as a sum of basis functions multiplied by an expansion coefficient,  $C_i$ . As an example, a trial wavefunction can be constructed as a linear combination of orthonormal single particle wavefunctions,  $\Psi_i$ :

$$\Phi = \sum_i C_i \Psi_i . \quad (2-10)$$

Since  $\Phi$  is normalized, the basis functions and coefficients are constrained to satisfy the orthonormal condition meaning

$$\begin{aligned} \int \Phi^2 dr &= \sum_{ji} c_i c_j \int \Psi_i \Psi_j dr = 1 \\ &= \sum_{ji} c_i c_j \delta_{ij} \\ &= \sum_i c_i^2 \end{aligned} \quad (2-11)$$

To find the energy of any particular state, both sides of Equation 2-2 can be multiplied with a trial wavefunction and integrated over all spatial components:

$$\int \Phi \hat{H} \Phi dr = \int \Phi E_i \Phi dr . \quad (2-12)$$

Since  $E$  is a scalar, it can be moved out of the integral. Using the orthonormal condition, Equation 2-12 can be recast in terms of the coefficients,  $C_i$ .

$$\begin{aligned}
\int \Phi \hat{H} \Phi dr &= \sum_{ij} c_i c_j \int \psi_j \hat{H} \psi_i dr = \sum_{ij} c_i c_j E_i \int \psi_j \psi_i dr \\
&= \sum_{ij} c_i c_j E_i \delta_{ij} \\
&= \sum_i c_i^2 E_i
\end{aligned}
\tag{2-13}$$

The results of Equations 2-11 and 2-13 can be used to construct an expression for the energy of any state relative to the ground state as:

$$\int \Phi \hat{H} \Phi dr - E_0 \int \Phi^2 dr = \sum_{ij} c_i^2 (E_i - E_0).
\tag{2-14}$$

The left hand side of Equation 2-14 is always greater than or equal to zero since  $c^2 \geq 0$  for all real values of  $c$ , and  $(E_i - E_0) \geq 0$  by the definition of  $E_0$ . This sets up the following inequality:

$$\int \Phi \hat{H} \Phi dr - E_0 \int \Phi^2 dr \geq 0.
\tag{2-15}$$

With rearrangement, Equation 2-15 becomes:

$$\frac{\int \Phi \hat{H} \Phi dr}{\int \Phi^2 dr} \geq E_0.
\tag{2-16}$$

In the example above, the wavefunction describes a single particle, but this is not a limitation of the method. The variational principle applies to single particle wave functions as well as many electron wavefunctions describing many atom systems. Also, in this example, the trial wavefunction was composed of a linear combination of orthonormal wavefunctions. This too is not a constraint of the principle but rather a convenient condition chosen for illustrative purposes.

#### 2.2.4 Antisymmetry and determinant wavefunctions

In the example provided in Section 2.2.3, the trial wavefunction is composed of a linear combination of basis functions that approximates the actual wave function. A

similar approach can be used to construct a many electron wavefunction. The choice of a trial wavefunction must consider that each electron has both spatial and spin components. A trial wavefunction,  $\Psi(x_1, \dots, x_n)$ , that captures both components can be constructed as linear combination of single particle wavefunctions  $\psi_a(x_i)$  composed as a product of spatial and spin components:

$$\psi_a(x_i) = \phi_a(r_i)\alpha(s_i). \quad (2-17)$$

In Equation 2-17, the arguments  $x_i$  refer to spin-orbitals that include both spatial,  $\phi_a(r)$  and spin components,  $\alpha(s)$ . The spin component arises as a consequence of Dirac's relativistic quantum mechanics<sup>61</sup> and result in the wavefunction being antisymmetric, meaning the wavefunction changes sign with the interchange of any electron pair:

$$\Psi(x_i, x_j, x_k) = -\Psi(x_i, x_k, x_j). \quad (2-18)$$

The antisymmetric nature of the wavefunction also leads to Pauli's exclusion principle, which states, in basic terms, that no two electrons can be described with the same identical quantum numbers.<sup>62</sup> A first choice to consider for a trial wavefunction would be product of spin and spatial components. To preserve orthonormality in  $\Psi(x)$ , the spin components must also satisfy the conditions:

$$\begin{aligned} |\alpha(s_i)\alpha(s_i)| &= |\beta(s_i)\beta(s_i)| = 1 \\ |\alpha(s_i)\beta(s_i)| &= 0 \end{aligned} \quad (2-19)$$

Normalization must also consider integrating over all spin orbital states:

$$\int |\Psi|^2 dx_1 \dots dx_n = 1. \quad (2-20)$$

The electron density when determined according to Equation 2-20 must also include the spin components such that the density at position  $r_1$  is:

$$\rho(r_1) = N \int |\Psi|^2 ds_1 dx_2 \dots dx_n = 1 . \quad (2-21)$$

An effective means of maintaining antisymmetry in the wavefunction was developed by Slater who represented the many electron wavefunction as determinant.<sup>63</sup> This approach exploits the property of determinants that the sign of the determinant changes when two rows or two columns are exchanged. For example the wavefunction for a system composed of two electrons with the same spin in different single particle states can be represented as:

$$\begin{aligned} \Psi(x_1, x_2) &= \sqrt{\frac{1}{2}} \begin{vmatrix} \phi_a(r_1)\alpha(s_1) & \phi_b(r_1)\alpha(s_1) \\ \phi_a(r_2)\alpha(s_2) & \phi_b(r_2)\alpha(s_2) \end{vmatrix} \\ &= \sqrt{\frac{1}{2}} [\phi_a(r_1)\phi_b(r_2) - \phi_b(r_1)\phi_a(r_2)]\alpha(s_1)\alpha(s_2) \end{aligned} \quad (2-22)$$

The electron density for the system can be constructed using Equation 2-21 with integration over both spatial and spin components:

$$\begin{aligned} \rho(r_1) &= 2 \int |\Psi|^2 ds_1 dx_2 \\ &= \int |\phi_a(r_1)\phi_b(r_2) - \phi_b(r_1)\phi_a(r_2)|^2 dr_2 \times |\alpha(s_1)|^2 |\alpha(s_2)|^2 . \\ &= |\phi_a(r_1)|^2 + |\phi_b(r_1)|^2 \end{aligned} \quad (2-23)$$

Equation 2-23 shows the prefactor of  $2^{-1/2}$  is normalization constant. In a similar manner, the wavefunction for a system of two electrons with opposite spins occupying the same orbital is given as:

$$\begin{aligned} \Psi(x_1, x_2) &= \sqrt{\frac{1}{2}} \begin{vmatrix} \phi_a(r_1)\alpha(s_1) & \phi_a(r_1)\beta(s_1) \\ \phi_a(r_2)\alpha(s_2) & \phi_a(r_2)\beta(s_2) \end{vmatrix} \\ &= \sqrt{\frac{1}{2}} \phi_a(r_1)\phi_a(r_2) [\alpha(s_1)\beta(s_2) - \alpha(s_2)\beta(s_1)] \end{aligned} \quad (2-24)$$

For more than two electrons, the determinant is expanded with an additional column for each new single particle wavefunction and an additional row for each new electron:

$$\begin{aligned} & \Psi(x_1, \dots, x_n) \\ &= \sqrt{\frac{1}{N!}} \begin{vmatrix} \phi_0(r_1)\alpha(s_1) & \phi_0(r_1)\beta(s_1) & \dots & \phi_{N/2-1}(r_1)\alpha(s_1) & \phi_{N/2-1}(r_1)\beta(s_1) \\ \vdots & \vdots & & \vdots & \vdots \\ \phi_0(r_N)\alpha(s_N) & \phi_0(r_N)\alpha(s_N) & \dots & \phi_{N/2-1}(r_n)\alpha(s_N) & \phi_{N/2-1}(r_n)\beta(s_N) \end{vmatrix} \end{aligned} \quad (2-25)$$

The notation gets a bit cumbersome at this point. The nomenclature and short hand used by Finnis helps matters.<sup>21</sup> One convenient condition for illustrative purposes is to only consider closed shell system where each orbital is doubly occupied. The Energy for the system is given as:

$$E = 2 \sum_{n=0}^{N/2-1} \varepsilon_n . \quad (2-26)$$

The prefactor of 2 is the occupancy. Similarly, the electron density for the many electron wavefunction is given by:

$$\rho(r) = 2 \sum_{n=0}^{N/2-1} |\psi_n|^2 . \quad (2-27)$$

The Slater determinant introduces an electron correlation energy called exchange correlation, where the Coulomb interaction between electrons with parallel spins is reduced compared to the repulsion between electrons with opposite spins.<sup>64</sup> This can be illustrated by solving the Coulomb integral between two electrons described by the wavefunction in Equations 2-22 and 2-24. In the case where electrons have the same spins, the repulsion between them is:

$$\begin{aligned}
& \frac{1}{2} \int \psi \frac{1}{|r_1 - r_2|} \psi dx_1 dx_2 \\
&= \frac{1}{2} \left[ \int |\phi_a(r_1)|^2 |\alpha(s_1)|^2 \frac{1}{|r_1 - r_2|} |\phi_b(r_2)|^2 |\alpha(s_2)|^2 dx_1 dx_2 \right. \\
&\quad - 2 \int \phi_a(r_1) \phi_b(r_1) |\alpha(s_1)|^2 \frac{1}{|r_1 - r_2|} \phi_a(r_2) \phi_b(r_2) |\alpha(s_2)|^2 dx_1 dx_2 \\
&\quad \left. + \int |\phi_a(r_2)|^2 |\alpha(s_2)|^2 \frac{1}{|r_1 - r_2|} |\phi_b(r_1)|^2 |\alpha(s_1)|^2 dx_1 dx_2 \right] \\
&= \int |\phi_a(r_1)|^2 \frac{1}{|r_1 - r_2|} |\phi_b(r_2)|^2 dr_1 dr_2 - \int \phi_a(r_1) \phi_b(r_1) \frac{1}{|r_1 - r_2|} \phi_a(r_2) \phi_b(r_2) dr_1 dr_2 \\
&= J_{ab} - K_{ab}
\end{aligned} \tag{2-28}$$

$J_{ab}$  represents the Coulomb integral between single particle states and,  $K_{ab}$  the exchange integral between states. The same calculation for two electrons with opposite spins occupying the same spatial state:

$$\begin{aligned}
& \frac{1}{2} \int \psi \frac{1}{|r_1 - r_2|} \psi dx_1 dx_2 \\
&= \frac{1}{2} \left[ \int |\phi_a(r_1)|^2 |\alpha(s_1)|^2 \frac{1}{|r_1 - r_2|} |\phi_a(r_2)|^2 |\beta(s_2)|^2 dx_1 dx_2 \right. \\
&\quad - 2 \int |\phi_a(r_1)|^2 \alpha(s_1) \beta(s_1) \frac{1}{|r_1 - r_2|} |\phi_a(r_2)|^2 \alpha(s_2) \beta(s_2) dx_1 dx_2 \\
&\quad \left. + \int |\phi_a(r_2)|^2 |\alpha(s_2)|^2 \frac{1}{|r_1 - r_2|} |\phi_a(r_1)|^2 |\beta(s_1)|^2 dx_1 dx_2 \right] \\
&= J_a
\end{aligned} \tag{2-29}$$

Comparing the two results shows how the Coulombic interaction between electrons is reduced when spins are parallel. The exchange correlation only affects the interaction between electrons with the same spin.

### 2.2.5 The Hartree-Fock (HF) method

The first useful method for approximating the solution to the many electron Schrödinger equation based on the variational principle was developed by Hartree.<sup>65</sup>

The Hartree method does not solve the true Schrödinger equation but instead solves the equation for non-interacting electrons. In the Hartree approximation, the electron-electron interaction is approximated with an external potential that represent the mean field of the electron density of the system. The external potential augments the electron-nuclear potential to give an effective potential,  $V_{\text{eff}}$ , acting on the electrons.

This mean field approximation simplifies the many body calculation in two ways. First the many body Hamiltonian can be treated as a sum of single particle Hamiltonians,  $H_i$ :

$$\left( \sum_{i=1}^N \hat{H}_i \right) \psi = E \psi . \quad (2-30)$$

Secondly, the single particle Hamiltonian is reduced to a potential and kinetic energy term:

$$\hat{H}_i = \hat{T}_i + V_{\text{eff}}(r_i) . \quad (2-31)$$

$V_{\text{eff}}$  contains both the external potential from the nuclear point charges and the potential due to the mean field of the other electrons:

$$V_{\text{eff}}(r) = V_{\text{ext}}(r) + \int \frac{\rho(r')}{|r - r'|} dr' \quad (2-32)$$

where,  $\rho(r')$  is the electron density due to all other electrons. The second integral on the right of Equation 2-32 is defined as the Hartree potential  $V_H(r)$ . Since  $V_H(r)$  depends on the existing electron density; the Hartree Hamiltonian must operate on a wave function upon which it depends. This means that the problem must be worked iteratively, with successive iterations giving improved wavefunctions, which in turn, can be used in the next iteration. If all goes well, both the wavefunction and the energy converge to invariant points where the difference in energy between iterations is suitably small that the solution can be considered converged.

The Hartree method is outdated but introduces a few significant innovations that are still indicative of quantum calculations. The method introduces an iterative solution based on the variational principle. This same technique remains in use for all methods that are solved variationally, which constitutes the vast majority of first principles calculations. The iterative nature of the calculations is also the root of the heavy computational expense of first principles methods. The Hartree method also makes use of the mean field approximation which has also carried on in various forms in today's methods. The main criticism of the method is the Hartree energy does not include the effects of electron correlation. We can at least address exchange correlation by using Slater determinant wavefunctions. This model is called the Hartree-Fock (HF)<sup>66</sup> method for which the Hamiltonian,  $F$ , is modified to include the exchange interactions:

$$\hat{F} = \hat{T} + \hat{V}_{ext} + \hat{G}. \quad (2-33)$$

The operator  $\hat{G}$  contains all the electron-electron interactions and is defined as:

$$\hat{G} = 2\hat{J} - \hat{K}. \quad (2-34)$$

$\hat{J}$  and  $\hat{K}$  are the Coulomb and exchange operators. The final Hartree-Fock energy,  $E_{HF}$  is found by operating  $\hat{F}$  on a Slater determinant wavefunction:

$$E_{HF} = 2 \sum_{n=0}^{N/2-1} \langle n | -\frac{1}{2} \nabla^2 | n \rangle + \int \rho(r) V_{eff}(r) dr - \frac{1}{2} \int \rho(r) V_H(r) dr + E_x. \quad (2-35)$$

The second term on the right of Equation 2-35 is the energy of interaction between each electron and the effective core potential defined in Equation 2-32. The third term corrects for the double counting of the interaction between each electron with the Hartree potential that is included in Equation 2-32. The first term in Equation 2-35 is the kinetic energy of each single particle state written in Dirac notation.

The Dirac style of notation simplifies the expression of many electron integrals.<sup>53</sup>

The style is also called “bracket” notation where the “ket”,  $|n\rangle$ , represent the single particle state  $\phi_n$ . The scalar product of  $|n\rangle$  with the “bra”,  $\langle n|$ , results in the complex conjugate of the single particle state. One other useful scalar product is between  $|n\rangle$  and a vector in real space  $\langle r|$ :

$$\langle r|n\rangle = \theta_n(r). \quad (2-36)$$

The last term in Equation 2-35 is the exchange energy defined as:

$$E_x = - \sum_{n=0}^{N/2-1} \sum_{m \neq n}^{N/2-1} \int \frac{\langle n|r\rangle\langle r|m\rangle\langle m|r'\rangle\langle r'|n\rangle}{|r-r'|} dr dr'. \quad (2-37)$$

The integration in Equation 2-37 runs over four indices, which means the method scales as  $N^4$  for  $N$  basis functions. This limiting factor restricts the method to small systems. Still,  $E_{\text{HF}}$  captures the essential qualities of chemical bonding. The main deficiency is that only exchange correlation is explicitly included in the result. However, post HF methods can correct for other correlation effects with chemical accuracy in small systems.

## 2.2.6 Key aspects of chemical bonding in molecular orbital theory

Wave function theory (WFT) gives the energy of a system of electrons based on molecular wavefunctions, also called molecular orbitals, which, in turn, are formed from a linear combination of local single particle orbitals. This molecular orbital based view is referred to as molecular orbital theory. Many of the properties we associate with chemical bonding: orbital hybridization, bond orders, partial charges and polarization to name a few, can be explained from the perspective of WFT in the context of molecular

orbital theory. A few of these key aspects of chemical bonding have to be refined a bit further to substantiate the approximations made in the empirical COMB formalism.

Since this work deals mainly with the development of variable charge potentials, the first useful concept to explore is the idea of partial atomic charge. WFT provides a means of determining the partial charge of each atom based on the degree to which the local atomic basis functions contribute to the molecular wavefunction. In Dirac notation, a single particle orbital can be described as  $|I\mu\rangle$  where the index  $I$  refers to the atom and  $\mu$  refers to a single particle orbital on that atom. As shown previously, a single particle state can be expanded as a linear combination of basis functions, in which case, expansion coefficients follow the same indexing:

$$|n\rangle = \sum_{I\mu} C_{I\mu}^n |I\mu\rangle. \quad (2-38)$$

The total number of electrons in the system can be summed up in terms of the expansion coefficients as:

$$N = \sum_{n=0}^{electrons} \left( \sum_{I\mu} f_n |C_{I\mu}^n|^2 + \sum_{I\mu J\nu, I \neq J} f_n C_{I\mu}^n C_{J\nu}^n S_{I\mu J\nu} \right). \quad (2-39)$$

In Equation 2-29,  $f_n$  is the number of electrons in each orbital ranging for zero to two.  $S$  is the overlap integral between basis functions:

$$S_{I\mu J\nu} = \langle I\mu | J\nu \rangle. \quad (2-40)$$

The notation in equations such as Equation 2-29 can get complicated. One useful concept is the density matrix<sup>30</sup> whose elements are defined as:

$$\rho^{I\mu J\nu} = \sum_{n=0}^{occupied} f_n C_{I\mu}^n C_{J\nu}^n. \quad (2-41)$$

Using the density matrices, Equation 2-39 can be rewritten as:

$$N = \sum_{n=0}^{electrons} \left( \sum_{I\mu} \rho^{I\mu I\mu} + \sum_{I\mu J\nu, I \neq J} \rho^{I\mu J\nu} S_{I\mu J\nu} \right). \quad (2-42)$$

The charge of each atom depends arbitrarily on how the contributions of the second summation in Equation 2-42 are divided between atoms. The simplest approach was proposed by Mulliken, who divided the second term evenly between all of the atoms upon which the basis functions resides.<sup>67-70</sup> The Mulliken charge at each site is then:

$$q_I = \sum_{\mu} \rho^{I\mu I\mu} + \sum_{J\nu} \rho^{I\mu J\nu} S_{I\mu J\nu}. \quad (2-43)$$

The method runs into problems when the orbitals are not orthonormal. Often the basis functions on individual atoms are constrained to be orthonormal. However, enforcing the same constraint on the set of molecular orbitals for the system is not mathematically convenient and often not beneficial. In such a case, the summations in Equation 2-43 do not equal N. Several schemes to address this concern have been proposed, all of which transform the orbitals into an orthonormal basis set. How this transformation is performed differentiates methods such as the Löwdin population analysis<sup>71</sup> and the natural population analysis (NPA).<sup>72</sup> While these methods maintain charge conservation, the various processes of rendering an orthonormal basis set alters the absolute value of charge. Consequently, results of various methods are not comparable to one another.

The Mulliken population analysis and its modifications have several other critical deficiencies, which restricts their overall general utility. First, as is apparent in Equation 2-43, the charges depend upon the basis functions so that charges calculated with different basis sets are not comparable to one another. Consequently, the analysis does not provide an absolute value for charge, but instead yields a relative charge subject to

the conditions of the calculation. Secondly, splitting contributions evenly between atoms is a rather crude approximation. One could imagine in a real system, with differences in electronegativity between atoms, that the distribution is more complex. For these reasons, partial charges are not useful by themselves as quantitative charge values within a material. Their best use is to compare changes in the relative partial charges in response to some change in the system. Occasionally, a variable charge potential will be touted for reproducing the partial charge generated by a Mulliken or similar population analysis. Such claims are somewhat specious, since the actual value of the charge can vary with the basis set used, and, while, relative trends in the population of orthogonalized, single particle basis functions may provide qualitative insight, there is no way to ensure relative values quantitatively represent change in the actual charge distribution in real systems.

Another concept that is useful for this work and can be derived from the density matrix is the bond order ( $BO$ ), which is a measure of the number of chemical bond that exists between a pair of atoms.<sup>73</sup> The range of values begins at zero when no bond exists, and increases by one for each additional bond formed between atoms. Bond strength generally increases with bond order. For example the carbon-carbon triple bond has a bond enthalpy of 8.51eV and a bond order of three versus 3.69 eV for the C-C single bond with a bond order of one. Hence, it is a critical concept to model when crafting a reactive analytical potential, especially for hydrocarbons where materials properties and chemistry are greatly influenced by the bond order. From WFT, the bond order is simply a sum of the off diagonal matrix elements of the density matrix:

$$BO = \sum_{n=0, I \neq J}^{occupied} f_n C_{I\mu}^n C_{J\nu}^n \cdot \quad (2-44)$$

An example used by Finnis to illustrate this concept is the bonding between diatomic hydrogen.<sup>21</sup> Each H atom contains one electron in one s-orbital,  $\phi_A$  and  $\phi_B$ , which combine to form a bonding molecular orbital,  $\psi_a$  and an antibonding orbital,  $\psi_b$ :

$$\begin{aligned}\psi_a &= \frac{1}{\sqrt{2}}(\phi_A + \phi_B) \\ \psi_b &= \frac{1}{\sqrt{2}}(\phi_A - \phi_B)\end{aligned}\tag{2-45}$$

In the ground state,  $\psi_a$  is occupied with 2 electrons, so  $f_0=2$  and  $\psi_b$  is vacant,  $f_1=0$ . The coefficients for the bonding state,  $C_A^0$  and  $C_B^0$  are equal to  $2^{-1/2}$ . For the antibonding state, the coefficients are  $C_A^1 = 2^{-1/2}$  and  $C_B^1 = -2^{-1/2}$ . Putting these values into Equation 2-44 gives a  $BO=1$  for the ground state meaning a single bond exists between atoms in the ground state. When one electron is promoted into  $\psi_b$  so that  $f_0=1$  and  $f_1=1$ , then  $BO=0$  and no bond exists.

This example also illustrates the essence of chemical bonding, where as atoms interact, the basis functions on each atom combine to form molecular orbitals. The molecular orbitals are both higher and lower in energy than the atomic states. The orbitals are populated from lowest energy states first. If more electrons are found in states lower in energy than the atomic states, then it is energetically favorable to form a bond.

The splitting of states continues as more atoms interact until, in condensed matter, the states broaden into bands.<sup>74</sup> Within a crystal, if we consider the exclusion principle, each band constitutes a single particle spin. The bands represent the distribution of energy states within the solid phase which can be described using the density of states

(DOS). If the single particle states,  $|n\rangle$  and energies,  $\varepsilon_n$ , are known, the global DOS for the system,  $D(\varepsilon)$  is defined as:

$$D(\varepsilon) = \sum_n \delta(\varepsilon - \varepsilon_n) \quad (2-46)$$

where,  $\delta$  is the delta function. The function  $D(\varepsilon)$  represents the number of states with energies in the range of  $\varepsilon+d\varepsilon$ . The band energy,  $E^{Band}$ , is the sum of the energies of the states given by the integral:

$$E^{Band} = \sum_n f_n \varepsilon_n = 2 \int_{-\infty}^{E_F} D(\varepsilon) \varepsilon d\varepsilon. \quad (2-47)$$

At zero temperature, the upper limit of the integral is the Fermi energy,  $E_F$ . The factor of two accounts for a closed shell system with each state being doubly occupied electron of opposite spin.

A local DOS for each orbital on any atom can be defined as a function that measures the relative contribution of each state of energy,  $\varepsilon$ , to the total DOS of the orbital. This is achieved by first defining the relative weight of each of molecular orbital:

$$D^{I\mu J\nu}(\varepsilon) = \sum_n C_{I\mu}^n C_{J\nu}^n \delta(\varepsilon - \varepsilon_n). \quad (2-48)$$

The global DOS is then the sum if:

$$D(\varepsilon) = \sum_{I\mu J\nu} D^{I\mu J\nu}(\varepsilon) S_{J\nu I\mu}. \quad (2-49)$$

The local DOS for orbital  $I\mu$  can be pulled from Equation 2-49 as:

$$D_{I\mu}(\varepsilon) = \sum_{J\nu} D^{I\mu J\nu}(\varepsilon) S_{J\nu I\mu}. \quad (2-50)$$

With an orthogonal basis,  $D_{l\mu}(\varepsilon)$  is simply  $D^{l\mu\mu}(\varepsilon)$ , the sum of which over  $\mu$  gives the  $D_l(\varepsilon)$  for each atom. The local DOS provides a route to approximating bond energies in condensed matter, which will be used to derive the short range contributions in COMB.

### 2.3 Density Functional Theory (DFT) of Inter-Atomic Interactions

The main limitation with the single particle HF methods is the error in the correlation energy. This error can be corrected with any of several post HF methods. The post HF corrections are naturally expensive and scale rather poorly with the number of electrons,  $N^4$  for the minimally useful methods.<sup>58</sup> Unfortunately, the accuracy of the methods only improves in direct proportion with the expense to the point where the most trusted post HF methods, coupled-cluster theory, scales as  $N^8$  where  $N$  is the number of basis functions. The poor scalability restricts the calculations for fairly small systems containing at the most a few dozen atoms. Typical calculations are performed on systems on the order of one to ten atoms.

One solution to the many-body correlation problem was advanced by Thomas and Fermi who found that for a system containing  $N$  electrons, there exist a unique functional of the electron density,  $E[\rho(r)]$ , which, when minimized with respect  $\rho(r)$  gives the true ground state energy of the system.<sup>75, 76</sup> A functional is a function that takes a function as its arguments. In this theory, the energy functional takes the electron density as its argument hence the name density functional theory. The appeal of this theory is the many body correlation effects are inherently included in the electron density. The resulting ground state energy is the exact ground state energy that can be solved as long as the appropriate functional is known. Unfortunately, the exact functional is not known and the theory in its current state relies on empirically derived

approximate functionals, thus yielding an approximate solution to the exact ground state energy. Still DFT includes correlation effects in a comparatively efficient manner, so can be applied to larger systems with reasonable cost. Systems of several hundred atoms are tractable on current computer systems. This has led to the acceptance DFT as the predominant first principles method in computational materials science, especially when electron rich atoms such as metals are involved in the calculation.

### 2.3.1 The Kohn-Sham Functional

Modern empirical potentials for materials stem primarily from DFT and follow an evolutionary development along the lines of tight binding theory (TB-DFT). Tight binding theory is semi-empirical density functional theory, where approximations are made to the total energy functional to increase the efficiency of the calculation. The theory encompasses of a wide range successively sever approximations, which result in correspondingly faster calculations, but at the cost of progressively limited transferability. Extrapolating this trend to its limit leads to fully classical empirical potentials.

The most useful tight binding energy functionals for deriving empirical potentials are themselves based on the Kohn-Sham functional which can be broken down into its component energy functionals as:<sup>27, 28</sup>

$$E^{KS}[\rho] = T_s[\rho] + E_H[\rho] + E_{xc}[\rho] + E_{eZ}[\rho] + E_{ZZ} \quad (2-51)$$

The main challenge with energy functionals preceding the Kohn-Sham approach was in dealing with the functional derivative of the kinetic energy. Previous methods approximated the kinetic energy, which proved to be a significant source of error. The Kohn-Sham approach works around the approximations to the kinetic by introducing a

reference system of non-interacting electrons with a density of  $\rho$ . The kinetic energy for this reference system is given by the functional,  $T_s[\rho]$ , which is the first term in Equation 2-51.  $T_s[\rho]$  does not yield the true kinetic energy, but rather the kinetic energy of a reference system. The actual kinetic energy functional requires a correction term,  $T[\rho]=T_s[\rho]+\Delta T[\rho]$ , which is assumed to be included in the  $E_{xc}[\rho]$ . The other functionals give, from left to right, the Hartree energy, the exchange and correlation energy, the electron-nuclear interaction and the nuclear-nuclear interaction. The annotation is modified for simplicity where  $\rho(r)$  is abbreviated as just  $\rho$ , which will be used when appropriate from here on.

The ground state for any energy functional is determined by finding the minimum in the energy functional with respect to electron density. In a manner similar to functions, the critical points for a functional correspond to point where the functional derivative is equal to zero. The ground state density is, therefore that which corresponds to the point where the functional derivative of  $E^{KS}$  with respect to density is zero with the constraint that total charge in the system is conserved:

$$\frac{\partial E^{KS}}{\partial \rho} = \frac{\delta T_s}{\delta \rho} + V_H(r) + V_{xc}(r) + V_{ext}(r) = \mu . \quad (2-52)$$

$\mu$  is the Lagrange multiplier used to enforce the constraint of charge conservation meaning the following condition is satisfied:

$$\int \rho(r) dr = N . \quad (2-53)$$

$\mu$  is an important concept that essentially represents the change in energy with electron density or in terms of charge, the change in energy as an electron is added or removed

from the system. The other potentials in Equation 2-52:  $V_H(r)$ ,  $V_{xc}(r)$  and  $V_{ext}(r)$ , are the functional derivatives of the corresponding energy functionals.

Solving the Kohn-Sham equation requires a bit of clever manipulation. The solution requires defining a reference system of non interacting electrons as:

$$\frac{\delta T_s}{\delta \rho} + V_{eff}(r) = \mu , \quad (2-54)$$

When  $V_{eff}$ , the effective potential acting on the electrons is defined as:

$$V_{eff}(r) = V_H(r) + V_{xc}(r) + V_{ext}(r) . \quad (2-55)$$

Equations 2-52 and 2-54 are equivalent and are solved with the same ground state density and kinetic energy. However, by choosing a system of non-interacting electrons as the reference system the, exchange and correlation contributions can be dropped and  $V_{eff}$  becomes essentially an external potential,  $V_{ext}$ . This sets up an eigenvalue problem which can be solved variationally:

$$\left( -\frac{1}{2}\nabla^2 + V_{eff}(r) \right) \psi_{KS}(r) = \epsilon_n \psi_{KS}(r) , \quad (2-56)$$

Eigenvalue equations in this context are referred to as the Kohn-Sham equations. The wavefunctions,  $\psi_{KS}$  are the single particle Kohn-Sham orbitals that correspond to the ground state solution of the Kohn –Sham equations. The electron density is given by:

$$\rho(r) = \sum_n f_n |\psi_n(r)|^2 \quad (2-57)$$

The summation runs over all electrons. The term  $f_n$  is an integer that represent the orbital population ranging from zero to two. The main advantages of this solution are that the ground state density and kinetic energy are determined via a self-consistent solution to a single particle eigenvalue problem. The problem a sequence of iteration

since  $V_{eff}$  is dependent on  $\rho$ . Most other approximations are gathered together in the  $E_{xc}$ . The method does not side step the challenges with the exchange and correlation functional but rather lumps all approximations together into one empirically parameterized functional.

Finnis reworked  $E^{KS}$  into a form that is useful for deriving empirical potentials.<sup>21</sup>

First, the potentials such as  $V_{eff}$  can be interpreted as operators  $\hat{V}_{eff}$  giving the following expressions:

$$T_s = \sum_n f_n \langle n | \hat{T} | n \rangle, \quad (2-58)$$

$$\int \rho(r) V_{eff}(r) dr = \sum_n f_n \langle n | \hat{V}_{eff} | n \rangle. \quad (2-59)$$

Combining the two expression gives:

$$T_s = \sum_n f_n \langle n | \hat{T} + \hat{V}_{eff} | n \rangle - \int \rho(r) V_{eff}(r) dr. \quad (2-60)$$

Replacing  $V_{eff}$  with its components gives Finnis's form of the functional:

$$E^{KS}[\rho] = \sum_n f_n \langle n | \hat{T} + \hat{V}_{eff} | n \rangle - \frac{1}{2} \int \rho V_H(r) dr - \int \rho V_{xc}(r) dr + E_{xc}[\rho] + E_{zz}. \quad (2-61)$$

The second term in the equation corrects for double counting of the Hartree energy since it is counted twice in the Hamiltonian. The third term subtracts any exchange and correlation contributions from the Hamiltonian and includes them in  $E_{xc}$ .

### 2.3.2 The Hellman-Feynman theorem and inter-atomic forces

If we intend to use the potential for dynamic simulations or optimizations then we have to deal with forces acting on the atoms, which in quantum mechanics, are found through the Hellmann-Feynman theorem.<sup>77</sup> The principle of the theorem states that

change in the energy due to change in some factor that alters the external potential is given by:

$$\frac{\partial E}{\partial R} = \left\langle \psi_0 \left| \frac{\partial V_{ext}}{\partial R} \right| \psi_0 \right\rangle. \quad (2-62)$$

The change in energy is not dependent upon the change in electron density at all; only the change in the external potential. As an example, provided by Finnis,<sup>21</sup> consider a system in the ground state where the energy is given by some functional,  $E[\rho]$ . If the external potential is altered with some small perturbation, such as a small change in interatomic displacements, the resulting change in energy to first order is:

$$dE[\rho(r)] = \int \frac{dF[\rho(r)]}{d\rho} d\rho dr + \int d\rho(r) V_{ext}(r) dr + \int \rho(r) dV_{ext}(r) dr + dE_{ZZ}(r). \quad (2-63)$$

For clarity,  $F[\rho]$  represents all other components of the functional derivative. With the adiabatic approximation, the electron density is minimized to the ground state for each small perturbation in the  $V_{ext}$ . Since  $\rho(r)$  is minimized, all terms that depend on  $d\rho(r)$  add up to zero leaving:

$$dE[\rho(r)] = \int \rho(r) dV_{ext}(r) dr + dE_{ZZ}(r). \quad (2-64)$$

Equation 2-64 restates the Hellmann-Feynman theorem, where the change in energy is not dependent upon change in the electron density.

$$\frac{dE[\rho(r)]}{dV_{ext}(r)} = \rho(r) + \frac{dE_{ZZ}}{dV_{ext}(r)}. \quad (2-65)$$

This theorem greatly simplifies the task of calculating inter-atomic forces. Once the ground state density is known, the forces acting on the nuclei in response to the ground state charge distribution can be solved through classical electrostatics. The self

consistent quantum calculation is only necessary to find the ground state electron density distribution.

### 2.3.3 The second order Kohn Sham functional

The Hellmann-Feynman theorem can also be turned around to derive functionals that yield the change in energy and electron density in response to a change in  $V_{ext}$  by introducing a scalar parameter,  $\lambda$ , that determines the external potential over the range of the change between  $V_{ext1}$  and  $V_{ext2}$ .<sup>21, 78</sup>  $\lambda$  ranges from zero to one. The potential in terms of  $\lambda$  is:

$$V_{est} = V_{est} + \lambda(V_{est2} - V_{est1}). \quad (2-66)$$

The Hellmann-Feynman equation that corresponds to this condition is:

$$dE[\rho(r)] = \int \rho(r, \lambda)(V_{ext2}(r) - V_{ext1}(r))d\lambda dr + dE_{ZZ}. \quad (2-67)$$

Integration with respect to  $\lambda$  gives the energy functional. However, solving the integral requires an approximation for the dependence of  $\rho(r)$  on  $\lambda$ . The first order approximation is to disregard any dependence  $\rho(r)$  on  $\lambda$ ,<sup>78</sup> which yields the following first order functional:

$$E^{(1)}[\rho(r), V_{ext2}] = E^{(1)}[\rho(r), V_{ext1}] + \int \rho_1(r)(V_{ext2}(r) - V_{ext1}(r))dr + E_{ZZ2} - E_{ZZ1}. \quad (2-68)$$

The error in the approximation varies linearly with  $\delta V_{ext}$  and so is only reliable for small variations in  $V_{ext}$ . However, the functional does not depend on a change in electron density, and, so, can be solved efficiently in situations where it is applicable.

An approximation to second order can be made by assuming the dependence of  $\rho(r)$  on  $\lambda$  is linear.<sup>21, 78</sup> The resulting functional is essentially obtained by replacing  $\rho_1(r)$  in the first order functional with the mean density  $\frac{1}{2}[\rho_1(r) + \rho_2(r)]$ :

$$E^{(2)}[\rho(r), V_{ext2}] = E^1[\rho(r), V_{ext1}] + \int \rho_1(r)(V_{ext2}(r) - V_{ext1}(r))dr + E_{ZZ2} - E_{ZZ1} \\ + \frac{1}{2} \int (\rho_2(r) - \rho_1(r))(V_{ext2}(r) - V_{ext1}(r))dr \quad (2-69)$$

The Kohn-Sham analog to the second order functional is given as:

$$E^{(2)}[\rho^{in}(r)] = \sum \langle n | \hat{H}^{in} | n \rangle + E_{XC}^{in}[\rho^{in}(r)] - \int \rho^{in} [V_{XC}^{in}(r) + \frac{1}{2} V_H^{in}(r)] dr + \frac{1}{2} \int C_{in}(r, r') \delta\rho \delta\rho' \quad (2-70)$$

The superscript “in” indicates a reference input density,  $\rho^{in}$ . Functions and functionals that are dependent upon  $\rho^{in}$  are also tagged with the “in” superscript. The first term on the right of Equation 2-70 is the sum of the single particle Kohn-Sham eigenvalues. The premise of the second order functional is that the energy is determined as function of  $\rho(r)$ , where  $\rho(r)$  is  $\rho^{in}(r)$  plus a small, continuous change in  $\rho(r)$ ,  $\rho(r) = \rho^{in}(r) + \delta\rho(r)$ .

Likewise, the single particle states are assumed to change smoothly with small changes in  $\rho(r)$ . The first term is a sum of the eigenvalues found by operating the following

Hamiltonian on the single particles states,  $|n\rangle$ :

$$\hat{H}^{in} = \hat{T} + V_{ext} + V_H^{in} + V_{ex}^{in}. \quad (2-71)$$

Harris analyzed Equation 2-70 further focusing on the last term, which is comprised of the second order terms resulting from the expansion of the  $E_H[\rho(r)]$  and  $E_{xc}[\rho(r)]$ .<sup>79</sup>

$$C_{in}(r, r') = \frac{1}{|r - r'|} + \left. \frac{\delta^2 E_{xc}[\rho(r)]}{\delta\rho\delta\rho'} \right|_{\rho^{in}}. \quad (2-72)$$

Solving the second order functional requires solving a Kohn-Sham equation of the form

$$(\hat{T} + \hat{V}_{eff}^{(2)})|n\rangle = \varepsilon_n |n\rangle. \quad (2-73)$$

The effective potential in this case is:

$$V_{eff}^{(2)} = V_{ext}(r') + V_H^{in}(r') + V_{XC}^{in}(r') + \frac{1}{2} \int C_{in}(r, r') \delta\rho(r') dr'. \quad (2-74)$$

Equation 2-74 indicates that the quantity defined in Equation 2-72 represents the change in the Hartree and exchange and correlation potentials due to change in the electron density.

Equation 2-70 is a convenient functional from which to begin the derivation of a classical potential that gives the energy as a function of change in the nuclear positions. The functional requires a self consistent step to arrive at the ground state density. However, the error in the energy is shown to be third order, so small variations around the true variational solution are tolerable.

### 2.3.4 The first order Kohn-Sham functional

Harris, Foulkes and Haydock found a first order approximation of the second order Kohn-Sham functional can be made by basically dropping the second derivative term from Equation 2-70.<sup>78, 79</sup>

$$E^{HF}[\rho^{in}] = \sum \epsilon_n + E_{XC}^{in}[\rho^{in}] - \int \rho^{in} [V_{XC}^{in}(r) + \frac{1}{2} V_H^{in}(r)] dr + E_{ZZ}[\rho^{in}]. \quad (2-75)$$

The appeal of this functional is that it is not variational. The eigenvalues are determined once based on the input density and so determining the energy only requires one step to solve the Kohn-Sham equation. Furthermore, the error in energy is second order in terms of the difference between the input and exact charge densities. With a careful choice of  $\rho^{in}$  and  $V_{XC}$ , the functional can actually be more accurate than the full self-consistent solution. The second order error is satisfactory for many applications considering the efficiency gained by avoiding a self consistent iterative procedure. The consequence of not being variational is the calculated energy may be higher or lower

than the actual ground state energy. There is no lower bound. Hence the results are only as reliable their validation allows.

## 2.4 A Self-Consistent Classical Electrostatic Potential

The purpose of an analytical potential is to determine the energy and forces acting on the nuclei as a function of the position of the nuclei. The first and second order functionals can serve as a starting point to derive an empirical potential with a foundation in density functional theory. The first order Harris-Foulkes functional provides a theoretical basis for several fixed charge, many-body potentials. Brenner has shown how the Abel-Tersoff and REBO potentials have their theoretical origins in this functional.<sup>52</sup> Likewise, Finnis has derived Pettifor's analytical bond order potential,<sup>21, 42</sup> the Finnis-Sinclair potential<sup>21</sup> and a basic ionic potential starting with the Harris-Foulkes functional.<sup>21</sup>

The second order functional provides a basis for a self-consistent tight binding model, in which several electrostatic analytical potentials have their theoretical basis. In particular, models that include change in the electrostatic interactions in response to the local environment, such as a polarizable core shell models,<sup>80</sup> can be derived from the second order functional. The dynamic charge potential central to this work also has its origins in the second order functional as well.

If the input charge density in second order Kohn Sham functional is equal to the exact Kohn Sham ground state charge density, the functional may be re-written as:

$$E^{(2)}[\rho^{in}(r)] = E^{HF}[\rho(r)] + \frac{1}{2} \int C_{in}(r, r') \delta\rho \delta\rho' . \quad (2-76)$$

The first order portion of the functional is equivalent to  $E^{HF}$ , the first order Harris-Foulkes functional. Equation 2-76 breaks the task of calculating the energy into two parts. The

Harris-Foulkes functional gives a non-self consistent solution to the energy that is only dependent upon the input charge density. The last term on the right of Equation 2-30 gives the change in the Hartree and exchange and correlation energies to second order. Together both terms provide a basis for a reactive analytical potential. Equation 2-76 also allows the derivation to be separated into self consistent and non-self consistent components of the potential.

#### 2.4.1 Self consistent electrostatic energy contributions

Ideally, a density function that can capture the change in energy with respect to electron density with one atom specific variable would solve the problem in as efficient a manner as possible. The partial charge on each atom can represent the change in density as long as the density distribution is rigid, meaning its volume and shape are fixed. Such a function is provide by Streit and Mintmire in their electrostatic plus model (ES+):<sup>22</sup>

$$\rho_i(r; q_i) = Z_i \delta(r - r_i) + (q_i - Z_i) f_i(r - r_i). \quad (2-77)$$

$Z$  is an effective core charge ranging between 0 and the total number of valence electrons in the atom.  $f(r)$  is a function that describes the radial charge distribution.

If we also neglect the change in  $E_{xc}$  and any covalent effects, then the change in energy as a function of charge is a sum of the change in energy in each atom. With this rigid ion approximation, the change in energy becomes the sum of the Coulombic interactions between charge densities.

$$E^{es}[\rho(r)] = \frac{1}{2} \int \frac{\rho(r)\rho(r')}{|r - r'|} dr dr'. \quad (2-78)$$

With rigid charge density distributions, Equation 2-78 can be thought of as the classical electrostatic interaction between charge densities the sum of which gives the total electrostatic energy,  $E^{es}$ , of the system.

Solving the Coulombic integral with the charge density function of Equation 2-78 yields several electrostatic potentials. The columbic interaction between charge densities,  $E^{qq}$  is given as the integral over charge density distribution functions,  $f(r)$ :

$$E^{qq} = \frac{1}{8\pi\epsilon_0} \sum_i \sum_j q_i \hat{J}_{ij}^{qq} q_j$$

$$\hat{J}_{ij}^{qq} = \iint \frac{f_i(r_i) f_j(r_j)}{|r_i - r_j - r|} dr_i dr_j$$
(2-79)

$\epsilon_0$  is the vacuum permittivity. The energy contribution due to the electron-nuclear interactions,  $E^{Zq}$ , is determined as the Coulombic attraction integrals between the valence charge and the effective core charge:

$$E^{qZ} = \frac{1}{4\pi\epsilon_0} \sum_i \sum_j q_i \hat{J}_{ij}^{qZ} Z_j$$

$$\hat{J}_{ij}^{Zq}(r_{ij}; Z_i, q_j) = \int \frac{f_i(r_i)}{|r_i - r|} dr_i - \iint \frac{f_i(r_i) f_j(r_j)}{|r_i - r_j - r|} dr_i dr_j$$
(2-80)

The energy due to nuclear-nuclear interactions is given by:

$$E^{ZZ} = \frac{1}{8\pi\epsilon_0} \sum_i \sum_{j \neq i} Z_i \hat{J}_{ij}^{ZZ} Z_j$$

$$J_{ij}^{ZZ}(r_{ij}; Z_i, Z_j) = \iint \frac{f_i(r_i) f_j(r_j)}{|r_i - r_j - r|} dr_i dr_j - \int \frac{f_i(r_i)}{|r_i - r|} dr_i - \int \frac{f_j(r_j)}{|r_j - r|} dr_j + \frac{1}{r}$$
(2-81)

When the core charge is approximated as a point charge and the densities are rigid,  $E^{ZZ}$  is a constant with respect to charge. Therefore, we can assume  $E^{ZZ}$  is included in the core-core interaction of the Harris-Foulkes energy.

Lastly, since the summations run over all atoms, there are intra-atomic Coulombic interactions between the valence and the core on the same atom,  $J_{ii}^{Zq}$  and the electron-electron interaction on the same atom,  $J_{ii}^{qq}$ . These one-centered integrals comprise the electrostatic self energy. With the rigid atom approximation, the self energy becomes a sum of atomic self energies,  $V^{self}$ :

$$E^{self} = \sum_i V_i^{self} = \frac{1}{4\pi\epsilon_0} \sum_i \left( J_{ii}^{qZ} q_i + \frac{1}{2} q_i J_{ii}^{qq} q_i \right). \quad (2-82)$$

Incorporating Equations 2-80 to 2-82 in Equation 2-76 gives a second order functional as:

$$E^{(2)}[\rho^{in}(r), Q] = E^{HF}[\rho^{in}(r)] + E^{self} + E^{qq} + E^{qZ}. \quad (2-84)$$

The choice of charge distribution function is somewhat arbitrary. Ideally, the function should be computationally efficient yet reliably reproduce properties of the material. The simplest approximation would be to use a point charge for the density distribution, which is common in potentials for ionic materials when efficiency is paramount. However, the point charge approximation has significant error when atoms are separated by close distances and goes to infinite values as atoms approach too closely together. This Coulomb catastrophe is avoided with spherical charge densities, which, instead, go to finite values as densities overlap. The effect of using spherical density functions as opposed to point charges is illustrated in Figure 2-1 which plots the interaction between two charged atoms versus separation distance. In Figure 2-1, dashed lines represent a point charge model and solid lines represent Coulomb integrals over spherical charge distributions. The charge on each atom is fixed at  $\pm 1$  with like charges giving positive values and opposite charges giving negative values.

The functions are nearly equivalent at long separation distances, but deviate near the typical range for bond lengths in solids. The point charge model goes to infinity at close separation which leads to a catastrophic failure of the model.

Spherical distribution functions have been shown to be effective in tight binding models and are the mathematically convenient.<sup>52</sup> A rigid spherical charge density simplifies the electrostatic portion of the Equation 2-76. Spherical densities also simplify evaluation of the Harris-Foulkes energy, which will be addressed in the next section. Considering these advantages, spherical densities strike the best balance between efficiency, reliability and performance. Streit and Mintmire's spherical density function is mathematically convenient and has been shown to perform well in analytical potentials.<sup>22, 40</sup> The function has one atom specific variable,  $\xi$ , which controls the radial rate of decay of the charge density:

$$f(|r - r_i|) = \xi_i^3 \pi^{-1} \exp(-2\xi_i |r - r_i|). \quad (2-84)$$

Incorporating Streit and Mintmire's density distribution function into the interaction integrals yields the following exponentially decaying functions. When  $\zeta_i = \zeta_j$ :

$$J_{ij}^{qq}(r) = \frac{1}{r_{ij}} - \exp(-2\xi r_{ij}) \left( \frac{1}{r_{ij}} + \frac{11}{8} \xi + \frac{3}{4} \xi^2 r_{ij} + \frac{1}{6} \xi^3 r_{ij}^2 \right), \quad (2-85)$$

and, when  $\zeta_i \neq \zeta_j$ ,

$$J_{ij}^{qq}(r) = \frac{1}{r_{ij}} - \frac{\xi_i \xi_j^4 \exp(-2\xi_i r_{ij})}{(\xi_i + \xi_j)^2 (\xi_i - \xi_j)^2} - \frac{\xi_j \xi_i^4 \exp(-2\xi_j r_{ij})}{(\xi_j + \xi_i)^2 (\xi_j - \xi_i)^2} - \frac{(3\xi_i^2 \xi_j^4) \exp(-2\xi_i r_{ij})}{r_{ij} (\xi_i + \xi_j)^3 (\xi_i - \xi_j)^3} - \frac{(3\xi_j^2 \xi_i^4) \exp(-2\xi_j r_{ij})}{r_{ij} (\xi_j + \xi_i)^3 (\xi_j - \xi_i)^3}. \quad (2-86)$$

The charge-nuclear interaction integral yields:

$$\int \frac{f_i(r_i)}{|r_i - r|} dr_i = \frac{1}{r_{ij}} - \xi_j \exp(-2\xi_j r_{ij}) - \frac{1}{r_{ij}} \exp(-2\xi_j r_{ij}). \quad (2-87)$$

The charge-charge interaction,  $J^{qq}$  has an  $r^{-1}$  term. Summations over  $r^{-1}$  functions are conditionally convergent, which leads to problems in calculating the total energy. A few techniques have been developed to deal with such summations. For this work, the sum is solved via a direct Wolf summation over charge neutral spheres.<sup>81</sup> The direct Wolf summation is computationally efficient and is easily incorporated into parallel codes. The technique adds an additional  $q^2$  dependent self energy term. This additional atomic self energy is assumed to be included in the self Coulomb interaction,  $J_{ij}^{qq}$ ; otherwise, the self energy is unnecessarily dependent upon parameterization of the long range summation.

The self energy terms in the rigid atom model comprise the energy to form a charge on each atom, which as shown by Rappe and Goddard,<sup>14</sup> may be approximated through a Taylor series expansion of the energy as a function of charge:

$$V_i^{Self}(q_i) = E_i^0 + \frac{\partial E}{\partial q_i} q_i + \frac{1}{2} \frac{\partial^2 E}{\partial q_i^2} q_i^2 \dots \quad (2-88)$$

Truncating at second order and solving at neutral charge as well as  $q=1$  and  $q=-1$  gives the following relationships:

$$V_i^{Self}(0) = E_i^0 \quad (2-89)$$

$$V_i^{Self}(+1) = E_i^0 + \frac{\partial E}{\partial q_i} + \frac{1}{2} \frac{\partial^2 E}{\partial q_i^2} \quad (2-90)$$

$$V_i^{Self}(-1) = E_i^0 - \frac{\partial E}{\partial q_i} + \frac{1}{2} \frac{\partial^2 E}{\partial q_i^2} \quad (2-91)$$

$V^{Self}(1)$  is defined as the first ionization potential (IP) and  $V^{Self}(-1)$  is the negative of the electron affinity (EA). From the above equation we can get:

$$\frac{\partial E}{\partial q_i} = \frac{1}{2}(IP + EA) = \chi_i \quad (2-92)$$

$$\frac{\partial^2 E}{\partial q_i^2} = (IP - EA) = J_{ii}^{qq}, \quad (2-93)$$

The first derivative of energy with respect to charge is the equivalent to the Mulliken electronegativity,  $\chi$ . With the rigid atom approximation,  $\chi$  is equivalent to one centered electron-nuclear interaction,  $J^{qZ}$ . The second derivative of energy with respect to charge is  $J_{ii}$ , the Coulombic interaction between valence electrons in the same atom. Equations 2-92 and 2-93 establish a way of determining  $V^{Self}$  directly from calculated or experimentally measured ionization potentials and electron affinities. When the expansion is truncated at second order, the resulting function is quadratic and exactly represents the first ionization potential and electron affinity. For many elements, the higher ionization potentials vary significantly from the quadratic solution. Additional higher order terms may be added to the function to fit higher oxidation states. In Equation 2-82, where  $V^{Self}$  is defined as the one centered integrals, the value is divided the vacuum permittivity  $(4\pi\epsilon_0)^{-1}$ . When the coefficients are derived from empirical values, such as with Equations 2-92 and 2-93, the permittivity is assumed to be included in the measured value and is not included explicitly in the equation.

Equation 2-88 provides a classical approximation to the change in energy with respect to the partial charge on each atom. The self consistent problem is reduced to determining the partial charge on each atom that corresponds to the ground state electron density configuration.

## 2.4.2 Dynamic charge equilibration

As defined previously, the electronegativity is the partial derivative of energy with respect to charge  $(\partial E/\partial q_i)_{q_j}$ . In Equation 2-52, the partial derivative of energy with respect to electron density is set equal to  $\mu$ , the Lagrangian multiplier that enforces the constraint of charge conservation. With the rigid atom approximation, where variation in electron density is only a function of charge, the derivative with respect to electron density can be truncated to the derivative with respect to partial charge. Likewise, it has been shown by Parr, that the electronegativity is also equivalent  $\partial E/\partial \rho(r)$  when the  $\rho(r)$  is the self consistent Kohn-Sham density.<sup>30</sup> By Equation 2-52, the ground state corresponds to the condition where the electronegativities are equal to  $\mu$  at all sites, provided that the total charge in the system is conserved. Likewise, the distribution of partial charges that corresponds to the ground state electron density distribution satisfies the condition that electronegativity is equal at all sites. The partial charges are selected as those that satisfy this unique electronegativity equilibration condition (EE) with the constraint that total charge is conserved.

The most computationally effective means of enforcing the constraint is through an extended Lagrangian method similar to that of Rick *et al.*,<sup>82</sup> where the constraint of charge conservation is enforced with an undetermined multiplier. The Lagrangian for the system is:

$$L = \sum_{i=1}^N \frac{1}{2} m_i \dot{r}_i^2 + \sum_{i=1}^N \frac{1}{2} M_{Q_i} \dot{Q}_i^2 - E^{HF} [\rho^{in}(r)] - E^{self} - E^{qq} - E^{qZ} - \Lambda_i \sum_{i=1}^N Q_i . \quad (2-94)$$

Here,  $M_q$  is a fictitious mass of each charge,  $m$  is the mass of each atom,  $\Lambda$  is the undetermined multiplier.

From the Lagrangian, we can derive equations of motion for both the real space coordinates and the dynamic charges as:

$$m_i \ddot{r}_i = \frac{-\partial E(Q, r)}{\partial r_i}, \quad (2-95)$$

$$M_Q \ddot{Q}_i = \frac{-\partial E(Q, r)}{\partial Q_i} - \Lambda = -\chi_i - \Lambda. \quad (2-96)$$

Since the total charge is conserved and therefore a constant motion, it follows that:

$$\sum_i \ddot{Q}_i = 0. \quad (2-97)$$

Solving the above two equations shows  $\Lambda$  to be the negative mean electronegativity for the system:

$$\Lambda = \frac{-1}{N} \sum_i \chi_i. \quad (2-98)$$

This leads to an equation of motion in charge space as:

$$M_Q \ddot{Q}_i = \bar{\chi} - \chi_i. \quad (2-99)$$

Equation 2-99 sets up a scheme to determine the partial charge on each atom concurrently with the spatial coordinates during the course of a dynamic simulation.

The charge equations of motion and be solved following each real space projection of the atomic positions using standard numerical integration algorithms. For this work, a velocity Verlet algorithm<sup>83</sup> is used to integrated both the real and charge space equations of motion.

In this scheme, the total energy of system is not conserved. The total force on each atom can be determined as the negative total derivative of the potential at each site. As an example, the component of force in the x direction acting one any atom is given by:

$$f_x = -\frac{dE}{dx} = -\sum_i \frac{\partial E}{\partial q_i} \frac{\partial q_i}{\partial x} - \frac{\partial E}{\partial x}. \quad (2-100)$$

When electronegativity equilibration condition is exactly satisfied so that  $\partial E/\partial q_i = \mu$  at all sites and the total charge on the system is equal to zero, the first term on the right of Equation 2-100 is equal to zero since:

$$\frac{\partial E}{\partial q_i} \frac{\partial q_i}{\partial r} = \mu \frac{\partial}{\partial x} \sum_i q_j = 0. \quad (2-101)$$

Therefore, if the electronegativity and charge conservation conditions are rigidly satisfied, we do not have to determine derivatives of charge with respect to position. In the scheme presented here, the EE condition is never exactly satisfied. The exact solution requires, first, a linear derivative of the energy with respect to charge and, secondly, solving N linear equations for the charge on each atom. The formalism presented here does not have a linear first derivative. With dynamic charges, fluctuation about the time average leads to a non-conserved condition at each time step. Although absolute energy conservation is not achievable with such a scheme, conservation within reasonable limits is possible by iteratively projecting the charges with damped velocities at each time step until the electronegativity at each site is nearly equal within a determined tolerance:

$$M_Q \ddot{Q}_i = \bar{\chi} - \chi_i + \nu \dot{q}_i. \quad (2-102)$$

$\nu$  is an empirically optimized damping factor. The solution in Equation 2-101 only applies to charge neutral systems. It's a convenient to maintain the constraint of charge neutrality for that reason and also because it avoids discontinuities in the energy when determined over periodic cells.

### 2.4.3 Analytical bond order potentials for multiphase simulations

Remaining part of the basic potential formalism requires an analytical approximation for the Harris-Foulkes energy. As noted earlier, the analytical bond order potential formalism has been shown to adeptly apply to many different bonding environments. The transferability of that potential comes in part from its origins in the Harris-Foulkes functional as shown by Brenner.<sup>52</sup> A review of Brenner's derivation highlights the approximations taken to achieve a purely analytical potential that emulates the underlying quantum physics of chemical bonding.

Abell derived a general form of an empirical potential to describe the attractive electronic energy contribution to inter-atomic interactions as a sum of bond energies:<sup>23</sup>

$$E_i^{el} = -\sum_{j \neq i} b_{ij} V^A(r_{ij}). \quad (2-103)$$

The function describes short range bond interactions and so is summed over nearest neighbors. The term  $b_{ij}$  is an empirical correction term that modifies the bond energy based on bond order. Abell was able to show that the bond order is most dependent upon the local coordination number of the atoms,  $Z$  and to first approximation  $b \propto Z^{1/2}$ . Higher local coordination yields a lower bond order and hence a weaker bond.

To be useful the attractive bond order potential must be combined with a short range repulsion term which approximates the short range repulsion between neighboring electron densities as atoms begin to overlap. The choice of functions for short range repulsions is somewhat arbitrary. Historically, functional forms are selected based on their accuracy in reproducing the empirical bond data and mathematical efficiency. Abell employed exponential functions for both the short range attraction and repulsive contribution to give an inter-atomic potential:

$$E_{coh} = \sum_i E_i ,$$

$$E_i = \sum_{j \neq i} [A_{ij} \exp(-\alpha_{ij} r_{ij}) - B_{ij} b_{ij} \exp(-\beta_{ij} r_{ij})]. \quad (2-104)$$

$A$ ,  $\alpha$ ,  $B$ , and  $\beta$  are fitted parameters.  $E_{coh}$  is the cohesive energy defined as the energy gained per atom when separate charge neutral atoms are bound into a cohesive solid state:

$$E_{coh} = \frac{1}{N} \left( \sum_{i=1}^N E_i - E^{Tot}(crystal) \right). \quad (2-105)$$

To derive energy per atom as given in Equation 2-105, the Harris-Foulkes functional (Equation 2-76) can be simplified by again using rigid, charge neutral, spherically symmetric charge densities centered on each atom as an approximation to the input density. In this case, as shown by Foulkes and Haydock,<sup>78</sup> the nuclear-nuclear and Hartree energies can be reduced to the sum of the Hartree energies of separate atomic densities, which is a constant,  $C_H$ , and the a sum of pairwise screening potentials between each atom:

$$\sum C_H + \frac{1}{2} \sum_i \sum_{j \neq i} V_{ij}(r_{ij}). \quad (2-106)$$

Equation 2-107 should be corrected for non pair-additive contributions due to the exchange and correlation functional,  $V_{np}$ . However, Foulkes and Haydock<sup>78</sup> demonstrate that in regions of minimal overlap between multiple atoms, a pairwise correction term is suitable, in which case  $V_{np}$  can be added to  $V_{ij}$  in Equation 2-107.

Foulkes and Haydock also show that with spherical charge densities,  $V_{xc}$  can be approximated with the expression:<sup>78</sup>

$$V_{xc}(r) = \sum_i V_i(r) + U(r). \quad (2-107)$$

$V(r)$  is an additive atomic potential and  $U(r)$  is a non-additive term that corrects for non-linearity in the exchange and correlation functional.  $U(r)$  is a small contribution to the total energy and may be neglected. If  $U(r)$  is neglected, the energy for the system given by the Harris-Foulkes functional can be approximated as a sum of pairwise interactions plus the sum of single particle eigenvalues based on the input charge density:

$$E_{tot} = \sum_i \sum_{j \neq i} \theta(r_{ij}) + \sum_n \varepsilon_n . \quad (2-108)$$

As pointed out in Equation 2-47 in section 2.2.6, the sum of the energies of the single particle states,  $\varepsilon_n$ , is the band energy,  $E^{band}$ , which is related to the global DOS,  $D(\varepsilon)$ , by Equation 2-47. With the 1<sup>st</sup> order functional, the band energy can also be defined in terms of  $H^{in}$  as:

$$E^{band} = \sum_{I\mu J\nu} \rho^{I\mu J\nu} H_{I\mu J\nu}^{in} . \quad (2-109)$$

The bond energy,  $E^{bond}$ , can be defined in a similar way as the inter-atomic contribution to the band energy:

$$E^{bond} = \sum_{I\mu J\nu, J \neq I} \rho^{I\mu J\nu} H_{I\mu J\nu}^{in} . \quad (2-110)$$

A comparison of Equation 2-110 to the definition of bond order given in Equation 2-44 reveals importance of bond order in determining the bond energies. As with the  $E^{band}$ , the bond energies may also be defined as a function of the local DOS for each single particle state:

$$E^{bond} = 2 \sum_{J\nu} \int_{-\infty}^{\varepsilon_F} (\varepsilon - H_{I\mu J\nu}^{in}) D_{J\nu}(\varepsilon) d\varepsilon . \quad (2-111)$$

Since the objective is an approximation of the energy per bond and knowing that the global DOS can be recovered as a sum of the local densities of state, the

appropriate approach is to approximate the local DOS for each eigenstate.  $D_{J\nu}(\varepsilon)$  is a distribution function, the shape of which can be characterized by its moments,<sup>84</sup> defined for the  $p^{\text{th}}$  moment as:

$$\mu_p^{J\nu} = \int_{-\infty}^{\varepsilon_F} \varepsilon^p D_{J\nu}(\varepsilon) d\varepsilon. \quad (2-112)$$

Comparing equations 2-112 with 2-47 shows the moments related directly to the Hamiltonian through

$$\mu_p = \sum_n \varepsilon_n^p = \sum_n \langle n | \hat{H}^p | n \rangle, \quad (2-113)$$

and for  $\mu_p^{J\nu}$ :

$$\mu_p^{J\nu} = \langle J\nu | \hat{H}^p | J\nu \rangle. \quad (2-114)$$

The moments are a measure of the shape of the DOS.<sup>84</sup> The first moment is the center of gravity of the distribution given as:

$$\mu_1 = \int_{-\infty}^{\varepsilon_F} (\varepsilon - \varepsilon_{Atomic}) D_I(\varepsilon) d\varepsilon = \sum_I (\varepsilon - \varepsilon_{Atomic}) D_I(\varepsilon) = 0. \quad (2-115)$$

With orthogonal orbitals and neglecting charge transfers, the choice of centering the distribution around the energy of the individual atomic orbital,  $\varepsilon_{atomic}$ , sets the first moment to zero. The second moment gives the width of the DOS<sup>84</sup> defined as:

$$\mu_2 = \sum_I (\varepsilon - \varepsilon_{Atomic})^2 D_I(\varepsilon). \quad (2-116)$$

The third moment characterizes the degree of skewness in the distribution and the fourth moment relates to the tendency to form a gap in the DOS. The cohesive energy of the solid relative to the free atoms is mainly related to the spread of the orbital energies, which is represented by the second moment. In fact, it can be shown that with approximations, the orbital energies on each atom are proportional to the square root

of  $\mu_2^I$ .<sup>84</sup> This relationship means the orbital energies can be found without having to determine the higher moments and without having to solve any Schrodinger equations. All that is needed is  $\mu_2^I$  and the equation of the line that relates  $(\mu_2^I)^{1/2}$  to the orbital energies.

The advantage of this method is the moments can be determined without explicitly knowing the DOS through the moments theorem,<sup>84</sup> which states that the  $p^{th}$  of the local DOS on each atom,  $D_I(\varepsilon)$ , is determined by the sum of all paths between  $p$  neighboring atoms that start and end on  $I$ . For the second moment, the path is just two hops: one to and one back from each neighbor. In other words, the second moment can be determined as the number of nearest neighbors,  $Z$ , and the orbital energies are proportional to the square root of  $Z$ . This approximation is referred to as the second moment approximation and forms a basis for several coordination dependent potential energy functions.

With perfect crystalline systems, the coordination on each site is clearly defined. The calculation of  $Z$  in disordered systems or when defects or interfaces are present gets more ambiguous as clear demarcations between neighbor shells disappear. A flexible definition of what is considered a neighboring atom is required in such circumstances. Finnis and Sinclair found one solution by replacing the sum over neighbors with the sum of function that decays exponentially with distance between atoms.<sup>21</sup>

$$E_I \propto - \left[ \sum_{J \neq I} e^{-\beta r} \right]^{1/2} \quad (2-117)$$

$\beta$  is an empirical parameter. Multiplying Equation 2-117 by an empirical proportionality constant,  $B$ , yields a potential energy function for the bond energy per atom. A short range pairwise repulsive term is needed to balance the bond energy which, when combined with the bond energy gives the Finnis-Sinclair potential energy function:

$$E_{coh}^{F-S} = \sum_I \sum_{J \neq I} A e^{-\alpha r} - \sum_I B \left[ \sum_{J \neq I} e^{-\beta r} \right]^{\frac{1}{2}}. \quad (2-118)$$

$A$ ,  $B$ ,  $\alpha$  and  $\beta$  are empirical parameters. As shown by Brenner, with a little manipulation, Equation 2-118 can be recast in a form similar to the Abell bond order potential energy function.<sup>85</sup>

$$E_I = \sum_{J \neq I} \left\{ B e^{-\beta/2r} \left[ 1 + \sum_{K \neq I, J} e^{-\beta(r'-r)} \right]^{-1/2} \right\}. \quad (2-119)$$

In this form, the bond order,  $b_{IJ}$  is:

$$b_{IJ} = \left[ 1 + \sum_{K \neq I, J} e^{-\beta(r'-r)} \right]^{-1/2}. \quad (2-120)$$

A significant improvement to the Abell bond order potential was made by Tersoff by including the effects of bond angles and symmetry in the bond order expression.<sup>11</sup>

$$b_{IJ} = \left\{ 1 + \left[ \beta_i \sum_{k \neq i, j} g(\theta) \zeta(r_{ij}, r_{ik}) \right]^{\eta_i} \right\}^{-\frac{1}{2\eta_i}}. \quad (2-121)$$

$\beta$  and  $\eta$  are empirical parameters.  $g(\theta)$  is a function that depends on the bond angle.

$$g(\theta) = 1 + \frac{c^2}{d^2} + \frac{c^2}{d^2 + (h - \cos \theta)^2}. \quad (2-122)$$

$\zeta$  is a function that penalizes differences in bond lengths  $r_{ij}$  and  $r_{ik}$ .

$$\zeta(r_{ij}, r_{ik}) = \exp[\alpha^m (r_{ij} - r_{ik})^m]. \quad (2-123)$$

$c$ ,  $d$ ,  $h$ ,  $\alpha$  and  $m$  are empirical parameters. The Tersoff formalism is one of the most effective models for modeling covalently bound systems. In COMB, the Tersoff formalism is used as the short range potential energy function. When atoms have zero charge, the bond energy is equivalent to the Tersoff bond energy. Additional modifications are included in COMB for charged states, which will be discussed in the next section.

#### **2.4.4 Beyond the rigid atom approximation**

The model presented to this point is basically self consistent variable charge electrostatic potential coupled to charge independent short range potential energy function. This approach is equivalent to models such as Streitz and Mintmire's ES+ which exhibit deficiencies that hinder their wide spread application. The SM potential, for example, can not model covalent systems and does not predict the ground state energy for alumina, the material it was originally designed to model.<sup>86</sup> The limitation of models of this type is due to the rigid ion approximation, which divides the potential energy function into separate electrostatic and bond energy contributions. The bond energy contribution is independent of charge and so is not altered with change in charge. Consequently, the bond energy does not change dramatically enough to clearly distinguish ionic, metallic and covalent bonding. At best the bond energy is fit as a compromise between two bonding environments. Such is the case with the SM potential, which is fit to balance metallic and ionic bonding for aluminum. In the COMB formalism, where the goal is to simulate multiphase interfaces, the rigid ion approximation is too severe. The performance of the potential is greatly improved by

incorporating a few additional changes in the potential energy due to change in the electron density distribution.

#### 2.4.4.1 Charge dependent short range energy contributions

A change in the partial charge on an atom indicates a change in the population of the frontier orbitals. This directly affects the bond order, which is a reflection of the relative population of the frontier bonding and anti-bonding states. The change in charge also changes the effective ionic radii, which influence both short range repulsion and the bond energy. A recent potential by Yasukawa addresses these changes in bond energy with charge.<sup>17</sup> The Yasukawa formalism is equivalent to Tersoff's potential at neutral charge, where, the short range energy is composed of a repulsive pair interaction,  $V^R$ , an attractive pair interaction,  $V^A$ , and dispersion interactions,  $V^{vdw}$ : The potential deviates from a pure Tersoff potential in that the magnitude and radial decay of the pair interactions vary with charge. Charge dependent correction functions,  $D_i(q_i)$ , are added to the exponential decay coefficient of the short range repulsive energy to reflect the change in atomic radius with charge. A similar correction is added to the short range attraction, to reflect the change in overlap with charge:

$$V^R(r_{ij}, q_i, q_j) = F_c(r_{ij})A_{ij} \exp\left\{-\lambda_{ij}r_{ij} + \frac{1}{2}[\lambda_i D_i(q_i) + \lambda_j D_j(q_j)]\right\}, \quad (2-124)$$

$$V^A(r_{ij}) = F_c(r_{ij})b_{ij}B_{ij}B_{ij}^*(q_i, q_j) \exp\left\{-\alpha_{ij}r_{ij} + \frac{1}{2}[\alpha_i D_i(q_i) + \alpha_j D_j(q_j)]\right\}. \quad (2-125)$$

In Equations 2-124 and 2-125,  $A_{ij}$ ,  $B_{ij}$ ,  $\alpha_{ij}$  and  $\lambda_{ij}$  are Tersoff parameters that are determined for each bond type. The change in short range contributions,  $D_i(q_i)$ , is specific to each element type according to:

$$D_i(q_i) = D_{U_i} + |b_{D_i}(Q_{U_i} - q_i)|^{n_{D_i}}, \quad (2-126)$$

$$b_{D_i} = (D_{L_i} - D_{U_i})^{\frac{1}{n_{D_i}}} / (Q_{U_i} - Q_{L_i}), \quad (2-127)$$

$$n_{D_i} = \frac{\ln D_{U_i} - \ln(D_{U_i} - D_{L_i})}{\ln Q_{U_i} - \ln(Q_{U_i} - Q_{L_i})}, \quad (2-128)$$

$D_U$  and  $D_L$  are parameters that reflect the change in atomic radius with charge.

Likewise,  $Q_U$  and  $Q_L$  are the atomic charges that correspond to the limits of the valence shell.

The short range attraction contribution is further modified with the function  $B_{ij}^*(q_i, q_j)$  that decreases the bond order with increasing charge:

$$B_{ij}^*(q_i, q_j) = (B_i^* B_j^*)^{\frac{1}{2}}, \quad (2-129)$$

$$B_i^* = \left[ a_{B_i} - |b_{B_i} (q_i - Q_{O_i})|^{n_{B_i}} \right], \quad (2-130)$$

$$b_{B_i} = \frac{|a_{B_i}|^{\frac{1}{n_{B_i}}}}{\Delta Q_i}, \quad (2-131)$$

$$a_{B_i} = \left( 1 - \left| \frac{Q_{O_i}}{\Delta Q_i} \right|^{n_{B_i}} \right)^{-1}, \quad (2-132)$$

$$\Delta Q_i = \frac{1}{2} (Q_{U_i} - Q_{L_i}), \quad (2-133)$$

$$Q_{O_i} = \frac{1}{2} (Q_{U_i} + Q_{L_i}). \quad (2-134)$$

The bond order term,  $b_{ij}$  is equivalent to Tersoff. Also, as in Tersoff, the short range pairwise interactions are terminated by multiplying with a cutoff function,  $F_c(r)$ :

$$F_C(R, R_S, S_S) = \begin{cases} 1 & r \leq R_S \\ \frac{1}{2} \left[ 1 + \cos \left( \pi \frac{r - R_S}{S_S - R_S} \right) \right] & R_S < r \leq S_S \\ 0 & r \geq S_S \end{cases} \quad (2-135)$$

In Equation 2-135, the interactions are terminated smoothly between two cutoffs,  $R_S$  and  $S_S$ .

With these modifications, the bond energy goes to zero when the charge on each atom corresponds to a filled valence shell. In such cases the attraction between atoms is described entirely by the electrostatic functions, reflecting a purely ionic state. With charges between the valence shell limits,  $b_{ij}$  contributes a varying degree of covalency to the bond energy, with a maximum contribution at zero charge.

#### 2.4.4.2 Polarizability and the point dipole model

Electronic polarization is a distortion in the electron density in response to an external electric field. The inclusion of explicit polarization has proven to be useful in classical simulations where they have been shown, for example, to stabilize the complex crystal structures of some oxides such as  $\alpha$ -alumina. It is suspected that in  $\alpha$ -alumina, the induced dipole and quadrupole moments of the anion stabilize corundum lattice.<sup>41</sup> Induced dipoles influence the interactions with small polarizable molecules such as water and  $O_2$ . Consequently, many current solvent models include explicit polarization effects. The inclusion of explicit electronic polarization is especially pertinent to this work, since two main interests are the study of oxidation and aluminum oxides.

The polarization response can be decomposed into several modes. In the classical response, the electron density is distorted from the equilibrium distribution in response

to additional potential generated by an external field. This response is generally long ranged and can be approximated with decent fidelity as a sum of atomic polarizations. At short bond distances, two additional modes of polarization comprise a significant portion of the total induced moment. At short separation distances, where the repulsion between electron densities of neighboring atoms is strong, the electron density distribution can be asymmetrically distorted away from the nuclei. This is what Dick and Overhauser labeled the short range interaction mode in their theory of dielectrics.<sup>80</sup> The effect increases inversely with separation distance. The second short range mode, what Dick and Overhauser referred to as exchange charge polarization, arises due to charge transfer between atoms in response to change in the overlap integrals between neighboring atoms. This exchange charge mode is explicitly modeled in COMB via the charge transfer scheme. No other modes are explicitly included since the COMB model relies on spherically symmetric atom centered density distributions.

As an example, the calculated polarizability tensor for molecular oxygen is anisotropic. Polarization parallel to the bond of the molecule is comprised of both short and long range contributions which in COMB are modeled with a redistribution of charge. Polarization perpendicular to the bond is only comprised of long range modes. These modes are not modeled in COMB which gives a polarizability of zero in all directions running perpendicular to the bond. Calculated values for the polarizability tensor determined via coupled cluster theory (CCSD(t))<sup>87, 88</sup> have a polarizability of  $\sigma_{zz}=2.0\text{\AA}^3$  along the bond and  $\sigma_{xx}=\sigma_{yy}=0.7\text{\AA}^3$  perpendicular to the bond for the molecule. The COMB model misses both the perpendicular response and quite possibly

the mitigating effects of the short range modes on the parallel response although the latter effects may be included indirectly in the dynamic charges equilibration.

One solution to capture the other polarization modes is to place a point dipole on each atom, similar to the fluctuation charge-fluctuating point dipole model by Sterne *et al.*<sup>89</sup> With this model, the dipole moment,  $\mu$ , is calculated directly from the electrostatic field generate by the atomic charges,  $\vec{E}_i^q$ , the neighboring induced dipoles and any external field,  $\vec{E}_{ext}$ .

$$\vec{\mu}_i = P_i \vec{E}(\vec{r}) = P_i \left[ \vec{E}_i^q + \vec{E}_{ext} + \sum_{j=1, j \neq i}^N T_{ij} \vec{\mu}_j \right], \quad (2-136)$$

$$\vec{E}_i^q = \frac{1}{4\pi\epsilon_0} \sum_{j \neq i}^N q_j \frac{\partial J_{ij}^{qq}}{\partial r} \frac{\vec{r}_{ij}}{|\vec{r}_{ij}|}, \quad (2-137)$$

$P_i$  is the polarizability tensor and  $T_{ij}$  is the dipole-dipole interaction tensor. For atoms, the polarizability tensor is isotropic and reduces to a scalar value. Induced dipoles calculated in this manner suffer the same instability at close approach as the variable charges.<sup>90</sup> Consequently,  $T_{ij}$  is employed as a damped function that diminishes as atoms overlap. For consistency, the same damping that is used with the Coulombic interactions is applied here:

$$T_{ij} = \frac{1}{4\pi\epsilon_0 |\vec{r}_{ij}|^3} \left( 1 - 3 \frac{\vec{r}_{ij} \cdot \vec{r}_{ij}}{|\vec{r}_{ij}|^2} \right) \left[ 1 - e^{-2\zeta_j r} (1 + 2\xi_j r_{ij} + 2\xi_j^2 r_{ij}^2) \right]. \quad (2-139)$$

The additional energy contributions are the dipole self energy, the dipole-charge interaction and the dipole-dipole interactions:

$$\begin{aligned}
U^{es}[(Q), (r)] = & \sum_i V_i^{Self}(q) + \frac{1}{2} \sum_i \sum_{j \neq i} q_i J_{ij}^{qq} q_j + \sum_i \sum_{j \neq i} q_i J_{ij}^{qz} Z_j + \frac{1}{2} \sum_i \sum_{j \neq i} V_{ij}(r_{ij}) \\
& + \sum_i \frac{\bar{\mu}_i^2}{2\alpha_i} + \sum_i \bar{\mu}_i \cdot \bar{E}_i^q + \frac{1}{2} \sum_i \sum_{j \neq i} \bar{\mu}_i T_{ij} \bar{\mu}_j
\end{aligned} \quad (2-138)$$

Since the induced dipoles contribute to the effective field, the point dipole model also requires that induced dipoles are solved self consistently. This leads to an additional iteration process during the charge equilibration that can be handled in two ways: either the dipoles are equilibrated self consistently during each charge timestep or the Lagrangian for the system is expanded to include dynamic point dipoles.<sup>9192</sup> The latter approach ensures the time average of the point dipoles, and therefore the Hamiltonian, is conserved, in which case the Lagrangian for the system becomes:

$$\begin{aligned}
L = & \sum_{i=1}^N \frac{1}{2} m_i \dot{r}_i^2 + \sum_{i=1}^N \frac{1}{2} M_{Q_i} \dot{Q}_i^2 + \sum_{i=1}^N \frac{1}{2} M_{\mu_i} \dot{\mu}_i^2 \\
& - U^{es}[(Q), (r)] - \Lambda_i \sum_{i=1}^N Q_i - U^{pol}[(\mu)]
\end{aligned} \quad (2-139)$$

$M_{\mu}$  is a fictitious mass on the dipoles. The dipole equations of motion can be determined and integrated using the velocity Verlet algorithm as is used throughout this work. In practice, the dipoles converge more rapidly than the charges. A tight convergence tolerance is achieved with one or two iterations of the dipole loop so either method achieves similar efficiencies. In either case, the point dipoles add computational cost and so are only solved for atoms where they contribute a significant portion to the interaction energy, i.e. the interaction between the surface and molecular oxygen.

#### 2.4.4.3 Atom in molecule corrections to the atomic self energies

The EE principle has a well-defined basis in conceptual DFT,<sup>93</sup> a body of work that seeks to explain chemical principles that govern reactivity in terms of DFT. While pursuing fundamental definitions for such concepts as electronegativity and chemical

hardness, that body of work suggests several improvements to consider in EE based potentials. One concept is the variation of atomic hardness when an atom is bound within a molecule or embedded in an ionic lattice.<sup>93</sup> In practice, EE methods are parameterized by either fitting the self energy coefficients to atomic gas phase ionization potentials and electron affinities or by fitting to bulk properties. In the former case, the difference between bulk and atomic properties is compensated by other terms within the potential. Here, the potential is fit to atomic values since the interest is in the interactions between atoms and small molecules with surfaces. To capture the change in atomic hardness as an atom is embedded in the bulk oxide, the hardness coefficient is augmented with a correction function that captures the change with its environment:

$$V_i^{Self}(q_i) = E_i^0(0) + \chi_i q_i + \left( J_i + \sum_{j \neq i}^N F_{ij}^{Field}(r_{ij}, q_j) \right) q_i^2 + K_i q_i^3 + L_i q_i^4 \quad (2-140)$$

Following the procedure outlined by Troufar *et al.*,<sup>94</sup> the environmental effect on the atomic hardness is determined by calculating the atomic self energy at the CCSD(t)/aug-cc-PVTZ<sup>95</sup> level in a symmetric field of point charges. The calculation is performed in a field of eight point charges arranged symmetrically around the atom at varying distance. The idea is to determine the effect of a confining potential on the atomic self energy function; the effect is converged with eight point charges. The sum of the point charges compensates the charge on the central atom so that the net charge of the system remains neutral, thus approximating charge being transferred from the central atom to its neighbors. The Coulombic interaction between the point charges and the central atom as well as between one another is subtracted from the total energy. Thus any change in the atomic self energy function is due solely to the field effect of the point charges on the atomic self energy. Figure 2-2 illustrates the calculated field effect

of the lattice on the atomic self energy of oxygen and copper. The effect is found to decay with radial distance as function of  $r^{-5}$ . A penalty function that captures the change in self energy due to the field strength is fit to the results of the calculation:

$$F_i^{Field}(r_{ij}, q_j) = \frac{1}{4\pi\epsilon_o} \sum_{j \neq i}^{NN} \left( \frac{P_1^J q_j}{r_{ij}^3} + \frac{P_2^J q_j^2}{r_{ij}^5} \right). \quad (2-141)$$

$P_1^J$  and  $P_2^J$  are adjustable parameters.

#### 2.4.5 Barrier functions

The last type of function included in the basic COMB model is barrier functions that restrict the model to regions that are well described by the potential. Functions of this type are not directly related to the chemical bonding but instead limit the potential to conditions where chemical bonding is appropriately described. Ideally, these functions should not interfere with the calculation but occasionally that is unavoidable.

The EE based dynamic charge scheme relies on a continuous self energy function. Such a function can be fit through all charge states until the valence shell limits. For atoms, once the valence shell maximum or minimum is reached the energy as functions of charge has a sharp discontinuity between valence shells. Therefore, the dynamic charge method is only appropriate when charges are limited to the valence shell. In this work, charges are constrained to valence shell with fourth order barrier functions of the form for  $q_i > Q_i^U$ :

$$V_i^{Barrier}(q_i) = P_i^{Qu} (Q_i^U - q_i)^4. \quad (2-142)$$

$Q^U$  is the charge corresponding to an empty valence shell.  $P^Q$  is a fitted parameter. An identical function is used to penalize partial charges below  $Q_i^L$ . Charge barriers of this type have also been shown to improve the stability of variable charge potentials.<sup>36</sup>

The second type of barrier function limits the allowed maximum coordination of the atoms. Variable charge schemes tend to favor dense oxide phases with high coordination. An additional barrier function on coordination is needed to de-stabilize the dense phases such as CuO in the NaCl crystal structure. The coordination correction used in the ReaxFF force field is applied here.<sup>16</sup>

$$V_i^{Coord}(\Delta N_i) = E_i^{Coord} \Delta N_i / (1 + \exp(\gamma_i^{Coord} \Delta N_i)), \quad (2-143)$$

$$\Delta N_i = CN_i - CN_i^*, \quad (2-144)$$

$$CN_i = \sum_{j \neq i}^{NN} F_c(r_{ij}, R_{s-ij}, S_{s-ij}). \quad (2-145)$$

$CN^*$  is the coordination number of the element in the ideal structure, and  $E^{Coord}$  and  $\gamma^{Coord}$  are fitted parameters.  $F_c$  is the same as Equation 2-135. The correction is only applied for metal-oxygen interactions so  $CN_i$  is the number of M-O bonds formed around atom  $i$ .

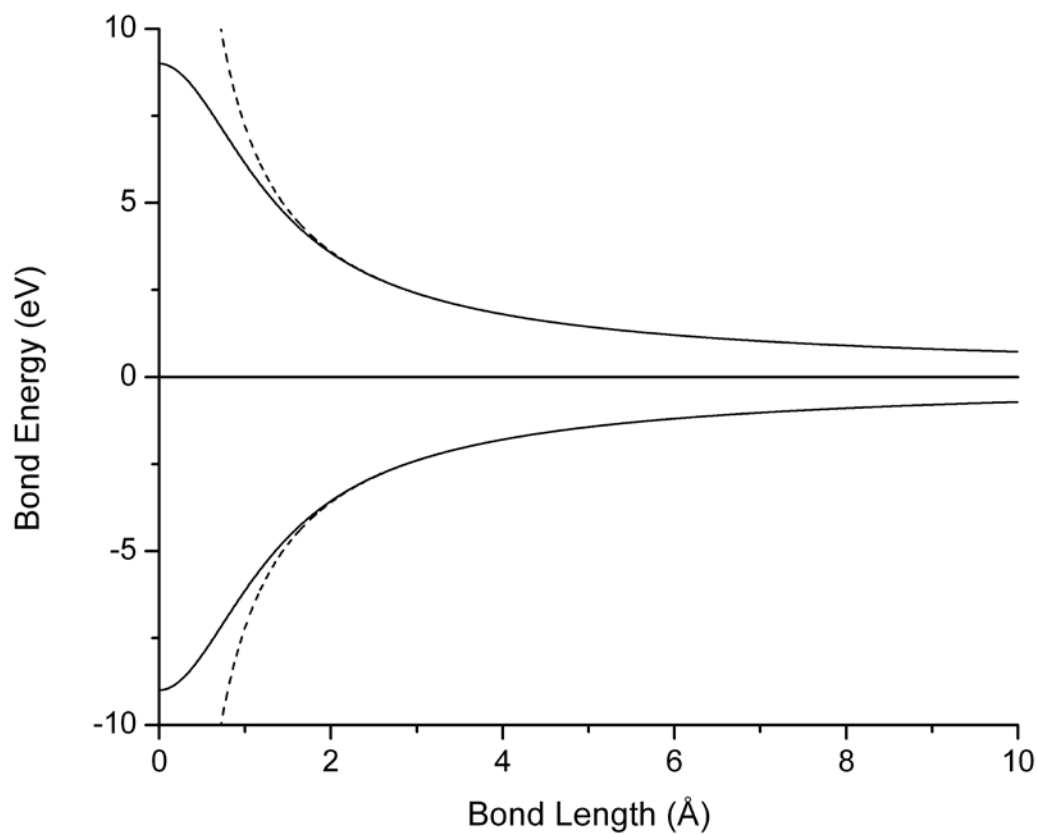


Figure 2-1. The interaction energy between two charged atoms is plotted vs. bond length. The interaction between like charges gives positive energies; opposite charges give negative energies. Solid lines are generated using spherical charge densities with  $\xi=2.0$ . Dashed lines correspond to point charges. At long separations, the functions are equivalent but begin to deviate near the range of typical bond lengths in solids.

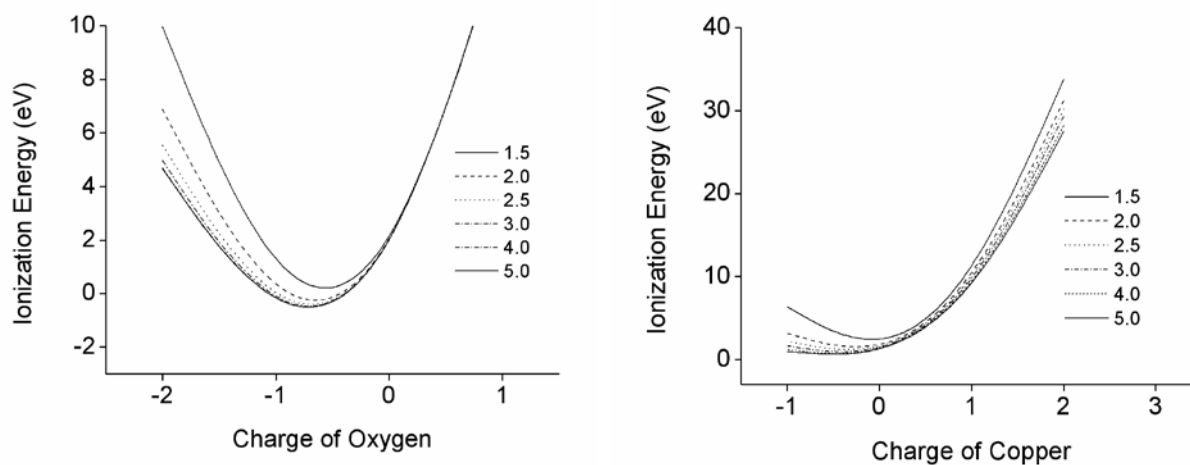


Figure 2-2. Self energy functions for O and Cu calculated in a field of eight point charges arranged symmetrically around each atom. Plots correspond to the radial distance ( $\text{\AA}$ ) between the point charges and the nuclear center. Calculations are performed at the CCSD(t)/cc-pVTZ level of theory.

CHAPTER 3  
A MULTILEVEL COMPUTATIONAL ANALYSIS OF FLUOROCARBON POLYATOMIC  
DEPOSITION ON DIAMOND\*

**3.1 The Computational Study of Polyatomic Deposition Reactions**

The strengths and weaknesses of several computational tools based on various levels of theory are discussed in some detail in the introductory chapter. Such comparisons are best illustrated with a comparative case study that explores the applicability of several levels of theory to a problem of interest. The study presented here compares findings from classical molecular dynamics simulations and density functional theory based simulations of fluorocarbon deposition on diamond. The energies are compared to higher quality multi-level post Hartree-Fock methods which have been shown to yield accurate values for energy in the system of interest. While the study suggests some interesting mechanistic phenomena about the deposition reaction, perhaps more importantly, it reveals the computational advantages of a classical approach and the consequence of approximations and the choices we make while developing classical potentials.

Fluorocarbon (FC) plasmas are widely used to chemically modify surfaces in industrial applications. For example, they are used to etch silicon wafers<sup>1-3</sup> and alter the properties of polymeric surfaces in order to increase their chemical inertness and resistance to oxidation.<sup>4-6</sup> The fluorination process alters the surface free energy and adhesive properties,<sup>7-9</sup> increases the hydrophobicity of the surface,<sup>10</sup> results in reduced coefficients of friction,<sup>10</sup> and produces higher dielectric constants in electronic devices.<sup>11</sup> Similarly, fluorinated diamond-like carbon (DLC) films may be synthesized from these

---

\* Reprinted with permission from Devine, I. Jang, T. Kemper, et al., J. Phys. Chem. C **114**, 12535 (2010).

plasmas. The resultant DLC films are formed at reduced temperatures compared to those formed from purely hydrocarbon precursors,<sup>6</sup> which enables their formation on temperature sensitive substrates. Thus, the properties of fluorinated surfaces and carbon films can be used for a wide range of applications and, consequently, have garnered significant attention over the past several decades.

From an experimental perspective, techniques such as solid-state NMR and x-ray photoelectron spectroscopy have established a direct, correlated relationship between products formed during deposition and the final properties of the surface.<sup>12-14</sup> Furthermore, the products formed on the surface are strongly influenced by the deposition conditions, including pressure, plasma and target temperature, deposition energy, and plasma composition.<sup>10,15-17</sup> Experimental capabilities have been further enhanced through mass selective ion beam techniques that add a level of direct control over the depositing species. With mass selective deposition, the incident particles are separated and accelerated based on the charge-to-mass ratio such that the surface products can be reasonably correlated against the mass and energies of the incident ions.<sup>2,3,18</sup>

What is missing from the above experimental repertoire is a means to explore the dynamic processes and surface chemical reactions that lead to product formation, areas where computational techniques provide increasingly significant insight. Often computational studies of surface reactions are constrained to single point calculations within a cluster model. This has been especially true with carbon surfaces, where charge transfer reactions require multi-reference methods with sophisticated treatments for electron correlation, such as complete active space, multi-configuration, self-

consistent field theory (CASSCF).<sup>19</sup> The higher quality results for geometries and relative energies that are achievable with a cluster model have been successfully used to explore property relationships, such as the relative stability of different structure reconstructions and relative adsorption energy versus surface terminations.<sup>20,21</sup> For example, *ab initio* methods applied to a cluster model have been used to map out the mechanisms responsible for chemical vapor deposition (CVD) film growth,<sup>22,23</sup> highlighting the critical role of the adsorption processes and hydrogen abstraction from hydrogenated surfaces.<sup>24,25</sup> The cluster model has also been used to identify the mechanisms of chemisorption and film growth with radicals on the diamond surface, which often prove intractable by other more efficient methods.<sup>26-29</sup> Chemically accurate calculations of bond enthalpies are limited to small cluster sizes, which leads to some deviation from the periodic solid due to a confinement of lattice strain through a smaller volume.<sup>29</sup>

Findings from mass selected experiments can be readily compared to the results of atomic-scale dynamic simulations. As a result of developments in efficient theoretical models, such as linear-scaling density functional theory (LS-DFT)<sup>30</sup> and reactive empirical potentials,<sup>31,32</sup> coupled with dramatic increases in computational power, it is now possible to carry out atomistic simulations of deposition across a range of theoretical rigor. Reactive empirical potentials can efficiently model reactions in systems containing a large numbers of atoms and dynamically simulate a statistically relevant number of deposition trajectories. However, since they are fit to properties of a training set, assumptions are necessarily made when extrapolating to systems beyond this data set. For example, the widely used reactive empirical bond order (REBO)<sup>31</sup> potential

does not include long-range Coulombic interactions and, so, is only able to model neutral molecules and radicals. It is fairly well established that during polyatomic ion deposition, and especially during accelerated deposition processes, both cationic and neutral radical species are present and participate in the reactions. Simulations of these processes using the second-generation version of the REBO potential<sup>31</sup> must assume that there is no difference in reactivity between cationic and radical states of the same molecule. This assumption may be reasonable at high deposition energies, where reactions predominantly involve fragmentation.<sup>16</sup> At lower deposition energies this assumption needs to be rigorously verified and its limits quantified.

The middle ground between predictive *ab initio* methods on small clusters and empirical simulations of large periodic systems is increasingly being filled with DFT, and especially DFT-based molecular dynamics (DFT-MD). In particular, linear-scaling DFT methods may be applied to systems containing several hundred, or even thousand, atoms using modern multi-core processors. The *SIESTA* method and code is a DFT code with linear scaling capabilities, where gains in efficiency are, in part, due to the reduced basis sets.<sup>96, 97</sup> This approach may lead to inaccuracies especially when simulating the interaction between a small polyatomic ion and a periodic solid system where basis set superposition error (BSSE) is likely. The numerical basis sets employed in the *SIESTA* method mitigates BSSE to some extent since the density of the neutral species is well described. Furthermore, the scalability of the *SIESTA* method requires a basis set that is truncated in spatial extent, which may lead to inaccuracies in the description of surface reactions at extended bond distances.

This work explores the surface reactions that occur during polyatomic FC ion deposition on hydrogen-terminated diamond surfaces using several different computational methods. In particular, classical MD simulations with the second-generation REBO potential and DFT-MD simulations are used to explore differences in reactivity between cations and free radicals in the ion beam. The results are compared to higher level quantum chemical calculations performed on small clusters with the intent of verifying the predictions of the MD simulations. The details of the simulations and each level of calculation used here are described in Section 3.2. The results for each level of theory are presented in Section 3.3, followed by a discussion in Section 3.4 that compares trends observed across all levels of theory. The conclusions of this work are given in Section 3.5.

The simulations in this work were actually performed over several years by a number of coauthors. As a good example of the computational cost of first principles simulations, the DFT-D simulations were initially started by Inkook Jang in 2005. At the time, a single simulation of one deposition event required nearly six months of processing time to complete using half of the most powerful machines available to us at the time. After several years, Inkook managed to finish the 10 runs in an initial test set. Since that time, Donghwa Lee ran the remaining DFT-MD simulations presented in the text. Since the initial work machines are much more powerful and the DFT-MD algorithms have been substantially optimized so now one trajectory requires only a month on one multi-core computer. Inkook also began the classical MD simulations but left the research group before their completion. Travis Kemper, finished that simulation work. All data analysis and the first principles calculations are the work of this author.

## 3.2 Computational Details

### 3.2.1 Classical molecular dynamics

A sampling of the reaction space is conducted using classical MD utilizing the second generation REBO<sup>98</sup> potential for carbon-based systems that has been extended to include fluorine.<sup>98</sup> Three hundred MD simulations are performed as single, isolated trajectories targeted over a small active region in the center of a larger periodic slab representing the diamond (111) surface. An 11,520 atom supercell is used to model the hydrogen terminated diamond (111) surface. Periodic boundary conditions (PBCs) are applied in two dimensions within the plane of the surface. The active region contains 128 carbon atoms within an area of  $10 \text{ \AA}^2$  on the diamond surface. A small active region is used to better enable comparisons to the more computationally intensive DFT-MD approach discussed in Section 2.2. The deposition energy in the classical MD simulations is 50 eV, which is in a hyperthermal range where smooth FC film growth is observed experimentally<sup>4</sup> but where effects due to the excited state potential energy surface are minimized.<sup>99</sup> The trajectory is normal to the surface with random variation across the active region. The depositing radicals are also randomly rotated relative to the surface. However, the radicals have little initial internal kinetic energy.

The classical simulations are performed at constant volume and temperature (NVT). The system temperature is maintained at 300 K via a Langevin thermostat.<sup>100</sup> No frictional force corrections are applied in the active region so that the thermostat does not interfere with the dynamics of the reactions. A Verlet algorithm is used to integrate the equations of motion with a time step of 0.1 fs. Finally, the simulations are carried out for 10 ps, which is sufficiently long for stable products to form.

### 3.2.2 Density functional theory- molecular dynamics

Deposition simulations are repeated using DFT-MD, which allows us to examine the deposition of both cations and radicals, albeit with a significant increase in computational expense. Specifically, the DFT implementation within the *SIESTA*<sup>97</sup> methodology and program is used. This approach improves the efficiency of traditional DFT-MD simulations for large periodic systems.<sup>101</sup> The *SIESTA* method is still subject to some of the errors associated with DFT in general, including the approximations present in the exchange and correlation functional, basis set incompleteness and BSSE, over-stabilization of partial charges, and static correlation errors, to name a few.<sup>29</sup> Consequently, an additional objective of this work is to verify the applicability of *SIESTA* DFT-MD for the simulation of FC deposition on diamond.

While the *SIESTA* method has improved efficiency compared to plane-wave based DFT implementations, it is still computationally expensive. Consequently, only 20 DFT-MD trajectories are considered using a supercell composed of the 10x10x13 Å active region used in the classical MD simulations. The supercell contains 128 carbon atoms with hydrogen terminated dangling bonds on the surface (see Figure 1a). In this case, the PBCs are applied in three dimensions, with 15 Å of vacuum added in the [111] direction. Two sets of 10 DFT-MD simulations are carried out; once set under neutral conditions, which corresponds to the deposition of CF<sub>3</sub> radicals, and one set with a positive charge applied to the system (that is compensated for using a uniform neutralizing background charge), which corresponds to the deposition of CF<sub>3</sub><sup>+</sup>. In each case the incident particles are deposited under the same conditions as during the classical REBO MD simulations (i.e. incident kinetic energies of 50 eV on a trajectory

normal to the surface). The simulations are again carried out within the NVT ensemble. However, in this case the temperature is maintained at 300K using a Nosé-Hoover thermostat applied to all the atoms.<sup>102-104</sup> Again, a Verlet algorithm is used to integrate the equations of motion with a time step of 0.1 fs. Simulations are performed for a total of 2 ps, at which point stable products have formed.

The nucleus and core electrons of each atom are represented with a Troullier and Martins<sup>105</sup> type norm-conserving pseudopotential. The valence electron Kohn-Sham states are expanded in a linear combination of atomic orbital type basis sets.<sup>96</sup> The basis set parameters for C and F are optimized to the relative energies of CF<sub>3</sub> and CF<sub>2</sub> radicals and their cations when compared to unrestricted coupled cluster calculations, uCCSD(t)/cc-pVTZ.<sup>88, 95, 106</sup> A double-zeta polarized basis (DZ2P) is employed where the polarization functions are explicitly included and determined according to soft confinement parameters. The optimized basis set is polarized with a *d* orbital on C and F. The soft confinement potential is set to 100 Ry (1360 eV) with an inner radius of 0.95 times the outer hard cut-off. A split norm fraction of 0.25 is used in the double-zeta construction for C and F, while the larger value of 0.5 is employed for H due to its greater variation in effective radius as a function of environment. A mesh cutoff of 250 Ry (3400 eV) is used to determine the fineness of the auxiliary grid basis for the expansion of the density.

The above basis set is a compromise between accuracy and efficiency, where a rather small basis set is necessary for computational efficiency in the periodic solid. This leads to a lower quality description of single molecules and, potentially, a significant BSSE when simulating surface reactions. However, because the basis functions are

generated from the numerical solutions of the atomic problem, the intrinsic BSSE is generally found to be smaller than for Gaussian basis sets, provided the radial confinement is not too great. The PBE functional is used to determine both the exchange and correlation contributions to the total energy in all the *SIESTA* DFT simulations and spin polarization is used.<sup>107</sup> The geometric parameters for  $\text{CF}_3$ ,  $\text{CF}_3^+$ ,  $\text{CF}_2$  and  $\text{CF}_2^+$  are presented in Table 1. It can be seen from the table that the DFT method with this basis set overestimates bond lengths by about 2.7% for both  $\text{CF}_3$  and  $\text{CF}_2$  cations and radicals, while it underestimates bond angles and improper torsions by 0.7%. The bond lengths and angles are marginally worse for  $\text{CF}_2$  and  $\text{CF}_2^+$ , with the largest deviations from reference calculations occurring for the  $\text{CF}_2$  radical.

### 3.2.3 Enthalpy calculations based on a cluster model

The heat of reaction at 0K ( $\Delta H^{0K}$ ) is calculated for smaller clusters as a benchmark with which to compare all the methods considered here, and to add some insight into the trends predicted in the classical and DFT-MD simulations. Standard references for the  $\square H^{0K}$  are calculated using the multilevel method G3MP2B3.<sup>108</sup> The computational cost of this method limits the total system size that can be examined to  $\text{CF}_3$  interacting with a ten carbon atom cluster (adamantane) that is illustrated in Figure 1b. These calculations are performed using the *GAUSSIAN03 (G03)* software package.<sup>109</sup>

In order to compare these calculations to the findings of the REBO-MD and DFT-MD simulations, a series of representative reactions are extracted from analysis of the reactions observed in the simulations. The  $\Delta H^{0K}$  for each of these representative reactions is then determined using both the G3MP2B3 within *G03* and the DFT approach. The DFT calculations performed on the clusters use the same basis set and

functional combination as during the DFT-MD simulations for both the geometry optimization and energy calculations. The REBO potential is parameterized without corrections for zero point vibrational energy (ZPE). Therefore, to compare results between methods no corrections for ZPE are made in this calculation. The G3MP2B3 method uses frequencies determined via B3LYP/6-31G(d) and scaled by a factor of 0.986 to calculate the zero point vibrational corrections.<sup>60, 110</sup> This contribution is, therefore, subtracted from the G3MP2B3 enthalpies to provide a direct comparison to REBO and DFT results.

Calculations performed with an adamantane substrate do not capture all the energy contributions to the reactions with periodic solids. Ideally, the cluster should be large enough to encompass the entire bonding region and maintain  $sp^3$  hybridization with carbon-carbon bonds around the bonding carbon atoms. The ideal cluster size to represent the diamond (111) surface was determined previously by Brown *et al.*<sup>58</sup> In that work, geometries were nearly fully converged within a 22-carbon atom cluster ( $C_{22}$ ), which is illustrated in Figure 1c. This cluster geometry maintains the diamond structure around the central carbon atom without freezing the terminal hydrogen atoms, which, consequently, minimizes contributions due to lattice strain to the total enthalpy calculation. This provides a more direct comparison between the various methods since the long-range forces vary between DFT and REBO.

The multilevel G3MP2B3 method is computationally too expensive to run efficiently with the  $C_{22}$  cluster. Density functional methods, however, are tractable with a decent basis set. Consequently, several hybrid functionals that have shown promise in calculating heats of reactions involving radicals<sup>111</sup> are evaluated against the G3MP2B3

results for adamantane. In each case, the B3LYP/6-31G(d) geometries are used. The reaction enthalpies are then calculated using the larger 6-311G(2d,p)<sup>112</sup> basis set. The specific functionals that are tested along with B3LYP include the BMK<sup>113</sup> functional, which has been found to yield promising results with free radical reactions,<sup>111, 114</sup> and the B98<sup>115</sup> functional, which has been found to produce reasonable bond dissociation energies for a large series of reactions and several molecular properties.<sup>114, 116</sup> In all the hybrid energy calculations using DFT with a Gaussian type basis sets, the integration grid is set to ultra fine (99,590 pts.) and Gaussian specified “tight” convergence limits are used in both the self-consistent field (SCF) iteration for energies ( $10^{-6}$  Hartree) and geometry optimizations.

### **3.3 Simulation Results**

#### **3.3.1 Classical MD simulations**

To sample the reaction space during radical deposition, 300 independent classical MD trajectories are performed. The simulations reveal that reactions during deposition are influenced by both the orientation of the deposited radical and the impact site on the diamond surface. Since the CF<sub>3</sub> radical has a pyramidal geometry, it reacts differently depending on whether the C atom or F atoms contact the surface initially. Reactions that involve the breaking of a C-F bond are only predicted when the F atoms of the FC are oriented towards the surface so that they make initial contact with a terminating H atom. The number of C-F bonds broken during initial impact depends on the number F atoms that make contact with H during the initial impact. When the radical approaches the surface with F atoms pointing towards the surface, fragmentation is likely to occur. Likewise, when the radical is oriented with the C atom pointing toward the surface, fragmentation reactions are predicted to occur less frequently. Most impacts that

produce reactions involve only one F atom contacting the surface and so lead to reactions involving the breaking on one C-F bond.

The location of the impact site on the surface also influences the reactions that occur. These impact sites can be categorized as an atop site, which is labeled *A* in Figure 3-2 and corresponds to a direct impact on a surface C atom or its terminal H atom, a subsurface site that corresponds to the recessed surface carbon atom, labeled *S* in Figure 3-2, and a hollow site, labeled *H* in Figure 3-2.

Each site has equal probability on the surface and, since the trajectories are randomly distributed across the surface, trajectories are equally distributed among all three sites. However, because the depositing FC is larger than the reaction sites, a majority of trajectories (60%) involve impact at the *A* site since it is the most prominent site on the surface. Likewise, the *S* site is more accessible than the *H* site, which results in the second highest incidence of impacts occurring at the *S* site (28%). Impacts that predominantly involve the *H* site are restricted to fairly specific orientations of the depositing molecule which are predicted to occur only 12% of the time. The impacts on the *A* sites are reactive and yield new products 80% of the time. In particular, of the *A* site reactions, 49% abstract a H atom from the surface and 45% result in CF<sub>3</sub> being bound to the surface with freely dissociated H. The impacts at the *S* site produce new products 32% of the time, with CF<sub>2</sub> and HF being the likely to occur. The CF<sub>2</sub> molecule is bound to the surface in about 50% of the reactions in which it is produced. These results are summarized in Table 3-2.

The dominant trend revealed by REBO-MD simulations is that the *A* site is significantly more reactive than the other surface sites. Secondly, all the products

formed from FC impact on this site involve the removal of H. This is consistent with the accepted mechanisms for growth of diamond films in which radical addition preferentially occurs at the A site following abstraction of atomic H from the surface.<sup>13,</sup>

117, 118

### 3.3.2 DFT-MD simulations

Ten trajectories are simulated with the DFT-MD approach at both neutral charge and with a positive (+1) charge applied to the system for a total of 20 DFT-MD simulations. The results for each charge state are given in Table 3. The orientation dependence that is observed during REBO-MD simulations hold true in the DFT-MD simulations as well. In particular, reactions that involve the breaking of a C-F bond are more likely to occur when the F atom of the deposition species is oriented towards the surface. However, in the DFT-MD simulations the FCs appear to be significantly more reactive than in the REBO-MD simulations, with reactions occurring during every deposition.

In comparing the DFT-MD results for the two charge states considered, we find qualitative similarities and differences in the reactivity of the cations and radicals despite the statistically low number of trajectories. For example, they clearly indicate that the  $\text{CF}_3^+$  cation is able to oxidize the diamond surface. The charge is applied to the system as a whole. As the cation approaches the surface, a Mulliken analysis indicates depletion of electron density from the surface carbon atoms and a neutral charge on the incident FC. The geometry of the FC cation also changes to the pyramidal configuration of the radical species indicating it has been reduced. This suggests that both FC species initially interact with the surface as radicals, which leads to several similarities in the observed reactions. For example, both species tend to form  $\text{CF}_2$  as a product with

similar probabilities (40% for the radical and 30% for the cation). They also both readily form HF when an F atom of the FC directly impacts a surface H atom. When significant fragmentation occurs, both species are able to add to the surface as  $CF_x$ , where  $x \leq 1$ .

When the cation oxidizes the diamond slab the surface appears to be less reactive than the neutral surface. This is illustrated by the observation that in 20% of the cation-deposition trajectories the only reaction observed is charge transfer to the cation without any bond breaking, whereas, in the radical deposition simulations, bonds are broken during every trajectory. Additionally, 30% of the cation-deposition trajectories result in H being dislodged from the surface without any occurrence of new bond formation; the pure dissociation of atomic H is observed in only 10% of the radical simulations. In 20% of the cation-deposition simulations, two H atoms are liberated and combine to form  $H_2$ . The cations also tend to fragment more extensively producing free atomic F and H species and unbound FCs. In two cationic simulations (20%), atomic F is predicted to migrate to the site of an under-coordinated C atom on the diamond surface and form a terminating C-F bond. The same reaction is seen just 1% of the time in REBO simulations and is not observed during DFT-MD simulations of radicals. Instead the radicals show a stronger propensity to form bonds with the C atom of the  $CF_3$  resulting in either new compounds, such as  $HCF_2$ , or surface bound FCs. In particular, such reactions are predicted in 50% of the radical-deposition simulations versus 20% of the cation-deposition simulations.

The statistics of the DFT-MD simulations are limited due the small number of trajectories explored and the large number of different reactions predicted. This is a necessary limitation of the method due to its computational cost. However, the results

do qualitatively indicate differences between species that can be further explored with calculations using methods of higher fidelity, as was done here.

### 3.3.3 Determination of $\Delta H^{0K}$ for reactions on adamantane ( $C_{10}$ )

The calculations are initially performed on the adamantane cluster illustrated in Figure 1b. Since the reactions of interest involve the A carbon site, calculations are performed on the flat surface of the cluster, as oriented in the figure. The products of radical deposition are illustrated in reactions 1-6 in Table 4, while the cation-deposition products are summarized in reactions 7-14 within the same table. Additionally, reactions 7 and 8 compare different charge transfers that involve the formation of  $CF_2$ , and reactions 11-13 explore different charge transfers involved in H dissociation from the diamond surface.

The most energetically favorable radical reaction at the G3MP2B3 level is the attachment of  $CF_2$  to the surface with the liberation of HF. The formation of  $HCF_3$  is less favorable by 0.34 eV, but is still exothermic. Attachment of  $CF_3$  to the surface is exothermic as well, but with an enthalpy that is 0.53 eV higher than the attachment of  $CF_2$ . The reaction enthalpy for the formation of unbound  $CF_2$ , reaction 5, is surprisingly high at 2.31 eV considering the prevalence of  $CF_2$  in the DFT-MD simulations. The 6.12 eV difference in energy between reactions 4 and 5 is the formation energy of HF. However, these are distinct reactions that are both observed in the DFT-MD simulations. In the case of reaction 5, HF is formed during the initial impact. In reaction 4, H and F are dissociated separately by the initial impact. Clearly, the hyperthermal deposition energy is driving these unfavorable reactions in the simulations. Similarly, the dislocation of H from the adamantane molecule (Reaction 6) requires 4.64 eV

suggesting that this reaction is also driven by the initial kinetic energy of the depositing species.

Reactions 7-14 reveal the most energetically favorable cation reaction to be the formation of the unbound  $\text{CF}_2$  diradical with a reaction enthalpy of  $-0.19$  eV. The liberation of H from the surface is less favorable by  $1.98$  eV but also reasonable considering the incident kinetic energy of  $50$  eV. The large positive enthalpies for reactions 12 and 13 indicate that H departs the surface as atomic H and leaves a cation site on the surface of the diamond cluster. Similarly, the large enthalpy for reaction 7, the formation of  $\text{CF}_2^+$ , shows the formation of the diradical with a cation site in the diamond cluster is more favorable by  $5.15$  eV. The large positive enthalpies for the bound products in reactions 9 and 10 suggest a decreased probability for these reactions.

For comparison, the calculation of reaction enthalpies is performed with several functionals, as well as with the *SIESTA* method, and the findings are given in Table 4. The results of calculations using *SIESTA* with the same functional and basis set as was used in the DFT-MD simulations agree with the results of calculations performed at the G3MP2B3 level with a mean absolute error of  $0.36$  eV for both radical and cation reactions. The most significant deviations occur for the attachment of the  $\text{CF}_3$  radical to the surface (reaction 2), where the *SIESTA* enthalpies are positive and  $0.38$  eV higher than the G3MP2B3 results, and for the oxidation of the diamond cluster (reaction 14), where the *SIESTA* DFT enthalpies are negative while all other methods give positive values. The B3LYP and B98 results are slightly more accurate with nearly identical

absolute errors of 0.23 and 0.22 eV, respectively. The BMK functional has the lowest absolute error with 0.10 eV and so is used exclusively in subsequent calculations.

### 3.3.4 Determination of $\Delta H^{0K}$ for reactions on $C_{22}$

Due to the small size of the adamantane cluster, the results are not directly comparable to those for the periodic diamond slab. This is because of the contribution to the reaction enthalpy due to lattice strain. In addition, the terminal H atoms on the neighboring A sites in the periodic slab are sufficiently close to form hydrogen bonds with a bound FC, such as in reaction 2. These secondary interactions are missing in calculations performed on an adamantane cluster.

For better comparison to the periodic slab, reaction enthalpies for the same reactions are calculated with the  $C_{22}$  cluster illustrated in Figure 1c. In this case, the energies are determined using the BMK functional for exchange and correlation contributions. We find that a large, polarized basis set is necessary to describe the bonding between the  $CF_3$  radical and the diamond cluster and to minimize the BSSE. Unfortunately, the cluster size demands that a mixed basis set must be used in the bonding region; the reacting species, surface H atom atoms and the internal C atoms are described with the 6-311G (2d,p) basis, while the external C atoms and terminal H atoms are described with the 6-31G(d) basis. The cluster naturally has a small non-zero dipole moment oriented into the surface along the surface normal, which the mixed basis set slightly enhances. The effects of the surface dipole are minimized in the enthalpy calculations since it is present in both the reactants and products, but we should expect some distortion of the results, especially when the products involve a charged species on the diamond cluster surface.

The calculated  $\Delta H^{0K}$  values for reactions on the  $C_{22}$  cluster are reported in Table 5. For the radical reactions, once again the formation of  $HCF_3$  is favorable. Surprisingly, the binding of the  $CF_3$  radical to the surface is exothermic by 0.92 eV with the BMK functional, which is larger by 0.95 eV than the results on adamantane. Reaction enthalpies for fragmentation into  $CF_2$  on the  $C_{22}$  cluster differ from the results from the adamantane calculations by only 0.02 eV, indicating that lattice strain due to the formation of a radical site in the cluster is nearly relaxed within the adamantane molecule. This finding agrees with earlier studies of radical formation on the diamond (111) surface, which found that the strain effect of radical formation is localized.<sup>119</sup>

Similarly, trends in the cationic reactions match those of previous calculations; the formation of the  $CF_2$  diradical is still exothermic and the binding of the cation to the surface is highly endothermic. A significant deviation occurs for reactions that result in the formation of a cation site in the diamond lattice. The enthalpy for reaction 7 drops by 0.46 eV and for reaction 11 by 0.41 eV due to a more relaxed lattice strain in the larger cluster, and stabilization of the surface charge by the surface dipole moment. Reaction 14, which considers charge transfer from the diamond cluster to the FC, is more favorable as well, apparently due to the increased stability of the positively charged diamond cluster.

Calculations are also performed on the  $C_{22}$  cluster using the *SIESTA* DFT approach and with the *REBO* potential, the results of which are also reported in Table 5. These results concur with those of the BMK calculations with a mean absolute deviation of 0.05 eV for *REBO* and 0.47 eV for *SIESTA*. Simulations using *REBO* suggest that the addition of  $CF_3$  to the surface is the predominant addition reaction. However, enthalpy

calculations predict that the addition of  $\text{CF}_2$  is energetically more favorable. The most significant deviation in the *SIESTA* based calculations is found for reaction 14 in which the oxidation of the diamond cluster by  $\text{CF}_3^+$  occurs. The *SIESTA* DFT calculations consistently predict lower reaction enthalpies when a positively charged diamond cluster is formed, which explains the significant decrease in enthalpy for reactions where this occurs.

### 3.4 Discussion of Results

The DFT-MD simulations and the enthalpy calculations on both clusters indicate a difference in the reactivity of cations vs. radicals; cations more efficiently remove H from the surface and radicals more readily form compounds. Calculations where the diamond surface is modeled with an adamantane cluster show that formation of a C-C bond between the depositing molecule and the diamond surface is more favorable with the  $\text{CF}_3$  radical and is energetically unlikely by 4.5 eV with the  $\text{CF}_3^+$  cation. The only energetically favorable reaction, in terms of enthalpy change, that is predicted by simulations of cation deposition is where the positively charged FC oxidizes the diamond target to form the  $\text{CF}_2$  diradical and a cationic site in the carbon cluster (reaction 6 vs. reaction 7). The reaction appears to be driven by the reduction of the energetic  $\text{CF}_3^+$  cation. The formation of a  $\text{CF}_2^+$  cation as a result of the collision requires 5.18 eV more energy than the formation of the  $\text{CF}_2$  diradical. The ionization potential of the diamond slab, which is 5.58 eV for the  $\text{C}_{22}$  cluster, is offset by the large favorable reduction potential of the  $\text{CF}_2$  radical.

The difference in reactivity between charge states is attributable to the cation oxidizing the diamond surface. A consistent trend through all levels of theory applied here is that the formation of molecular products during the initial impact, whether they

are surface-bound or free, is enhanced with the formation of HF on the surface. With the  $\text{CF}_3$  radical, HF and  $\text{CF}_2$  are readily formed whenever an F atom directly impacts an H atom. The oxidized surface inhibits the formation of HF and instead favors the dissociation of unbound H from the surface. HF does form during cation deposition, but more frequently it forms as a secondary product rather than during the initial impact. Similarly,  $\text{H}_2$  is predicted to be a common secondary product following the recombination of two free H atoms. This overall difference in reactivity, which is initially somewhat surprising given the high impact energy considered, is explained if cations and radicals follow different reaction pathways.

The difference in the reactivity between the two charge states has some interesting implications. Firstly, a beam that contains both charge states at impact will have competing reactions that could alter the composition and structure of the products that form. Secondly, the findings from mass-selected deposition experiments may not directly apply to more typical production techniques with lower concentrations of cations. Thirdly, classical potentials that do not include charge do not fully capture the chemical complexity of these deposition processes.

The actual effect of cations on film growth is not easily resolved. 60% of the cation trajectories result in the dissociation of atomic H from the diamond surface to produce free gaseous H atoms. The conventionally accepted mechanisms for growth on diamond films from radical precursors, under low energy conditions, propose a process in which atomic H is abstracted from the surface, leaving behind a radical site.<sup>118</sup> Radical precursors may then add directly to the surface at the residual radical sites. The suspected rate-limiting step in that proposed mechanism is the abstraction of H, at

which cationic precursors are predicted to be more effective. Furthermore, the presence of the resulting free atomic H may further enhance subsequent film formation since film growth rates from radical precursors have been shown to vary directly with the gas phase concentration H.<sup>120</sup> The distinction from radical based film growth, however, is that the cationic precursors oxidize the surface leaving behind a cationic site. The role of these cationic sites in subsequent film growth will have to be investigated further to understand their role during growth.

The DFT-MD and REBO-MD simulations support a similar two-step mechanism for film growth with  $\text{CF}_3$  as a radical precursor, where, the most energetically favorable initial reaction is the abstraction of H by the  $\text{CF}_3$  radical. However, the simulations also suggest an alternate mechanism where the FC radical adds directly to the surface. This one-step addition is predicted with almost equal probability to H abstraction in the REBO simulations. The reaction enthalpies for the single-step addition (reaction 3) show the reaction to be favorable when coupled to the formation of HF. However in REBO the formation of HF occurs less frequently. To further explore this mechanism and the discrepancy among the methods, the transition state for the single step addition of  $\text{CF}_2$  to adamantane from a  $\text{CF}_3$  radical precursor is found using the synchronous transit quasi Newton-Raphson algorithm within the G03 suite (QST2).<sup>109</sup> The search and optimization are performed using B3LYP//6-31G(d), as was the case in previous optimizations. The starting point positions of the reactants are varied to replicate several trajectories that produce the products in the MD simulations. A diagram of the optimized transition state is presented in Figure 3. Reactants arrive at the same saddle point regardless of whether the  $\text{CF}_3$  radical is oriented with its C atom up or down

relative to the cluster. The activation enthalpy, determined as the difference in energy between the saddle point geometry and the separate reactants, is found to be 7.2 eV. The activation enthalpy is smaller than the 50 eV deposition energy by a substantial amount, so the reaction is able to proceed.

The present multilevel analysis provides an opportunity to compare and contrast the computational methods considered, especially in a case such as this where different approximations are made within each method. The first question, when comparing cluster models to periodic systems, is how large must the system be to minimize the effects of lattice strain? In the case of radicals, the radical defect in the diamond structure is contained by its nearest neighbors with little change in enthalpy between the 10 and 22 carbon-atom clusters. In contrast, the bound products and the cationic defects require larger surfaces for a realistic description. To further test the size effect, single point calculations are performed using the periodic supercell from the MD simulations, the results of which are presented in Table 6. The calculations show comparable values to those on the  $C_{22}$  cluster, which indicates that the strains due to both a cationic defect in the diamond surface and the addition of  $CF_3$  to the surface are contained within the  $C_{22}$  cluster.

The predictions from the REBO-MD simulations and DFT-MD simulations exhibit a few critical differences. Firstly, the classical REBO simulations predict a higher prevalence of non-reactive trajectories; only 58% of the total REBO trajectories result in reactions compared to a 100% reaction probability in the DFT-MD radical simulations. Secondly, the products formed most often during the REBO simulations involved  $CF_3$ , whereas in DFT-MD the depositing  $CF_3$  radical or cation is never intact at the end of any

trajectory. Finally, the formation of HF is predicted to occur much less frequently in the REBO simulations than in the DFT-MD simulations.

The lack of HF formation in the REBO simulations is initially surprising given that the enthalpy calculations with the same potential favor the formation of HF and CF<sub>2</sub>. This discrepancy arises due to the short cutoff distance for covalent H-F interactions within the REBO potential. In particular, the H-F interactions are cut off smoothly between 1.4 and 1.8 Å. This consequently limits the formation of HF during the course of a dynamical simulation. This is illustrated in the transition state shown in Fig 3. The H-F bond length in this structure is 1.73 Å, which is near the end of the cutoff region of 1.8 Å; in this region the H-F interactions are severely damped and when just a 4% strain is placed on the bond, the interactions are terminated completely. In contrast, the C-F bond length of 1.78 Å is just outside the cutoff region for that interaction, which begins at 1.8 Å and terminates at 2.2 Å. Consequently, with REBO, the formation of a CF bond to form CF<sub>3</sub> is more likely from the transition state presented in Figure 3. This explains the greater occurrence of CF<sub>3</sub> remaining intact and the reduced prevalence of HF in the REBO simulations. The short-range cutoffs in the REBO formalism are necessary to spatially restrict the bond order contributions. This leads to an improved description of ground state properties, but the detrimental effect of these cutoffs in describing transition states here are apparent.

The enthalpy calculations presented here do not include corrections for *ZPE* as a convenient means to make comparisons between methods. This correction is one of several necessary corrections to first principles calculations needed to compare calculated enthalpies to experimental values. As a qualitative check, *ZPE* corrections

are calculated for the reactions in Table 5. The last column in Table 5 lists values for  $\Delta H^{0K}$  determined with the BMK functional and corrected for *ZPE*. The enthalpy contributions due to *ZPE* are calculated based on B3LYP//6-31G(d) frequencies scaled with the G3MP2B3 scaling factor (0.986). The results indicate that the *ZPE* corrections do not affect the qualitative trends of the calculated enthalpies, but do contribute, on the order of 0.25 eV, to the total enthalpy for the reactions.

An important consideration regarding the use of *ab initio* computational methods based on a LCAO basis sets is BSSE, which arises when reactions involve a small molecule bound to a larger cluster. Out of necessity, DFT-MD with the *SIESTA* method requires a modest basis set for efficiency; the resulting incompleteness of the basis set gives rise to a likely BSSE. To illustrate this, a counterpoise calculation<sup>121</sup> is performed for reaction 3 on the  $C_{22}$  cluster using *SIESTA* DFT with the same basis set as in the previous enthalpy calculations. The  $\Delta H^{0K}$  for this reaction is underestimated by 0.18 eV or 17.5% due to BSSE by this method, which is on the order of the reaction enthalpy for the addition of  $CF_2$  to the surface. Since the error applies mainly to the reactions that produce a bound product, it is significant and may alter the statistical findings of an MD simulation. In the cluster calculations an attempt is made to minimize this effect by using a larger basis set for all interacting atoms, which is more difficult to do in MD simulations. In practice, the BSSE may lead to an over-stabilization of bound products through the course of DFT-MD simulations, which must be taken into account when assessing these predictions. Nevertheless, the qualitative trends in the method are correct.

It should be noted that the REBO results are not subject to a BSSE error and may be more reliable where applicable. The enthalpy calculations with REBO clearly indicate that the potential accurately captures the relative energies of reactant and products involved in the radical reactions.

### 3.5 Concluding Remarks

The results indicate that the classical REBO potential and the DFT method within the *SIESTA* program are comparable in accuracy to DFT methods using commonly used functionals such as B3LYP when they are applicable. Besides the gain in efficiency, classical methods, such as the REBO potential, are not subject to BSSE and other sources of error specific to quantum-mechanical based theories. Unfortunately, the REBO potential is currently limited to charge neutral systems, which, as indicated here, pose a serious limitation to accurately describing experimental cationic deposition.

The study also shows that the applicability of REBO is limited since it does not accurately reproduce some of the critical transition states involved in the reactions. The current REBO formalism requires a cutoff between the first and second nearest neighbors to reproduce properties of the equilibrium ground state. This leads to inaccuracies when describing long range interactions such as bond breaking<sup>122</sup> or unusual bonding environments such as amorphous systems.<sup>123</sup>

The DFT–MD method within the *SIESTA* approach is reasonably efficient for a first principles electronic structure method. The absolute errors in reaction enthalpies are on the order of 0.5 eV, based on the present basis set and functional, which limit its applicability to qualitative analysis under high-energy conditions. The main advantage of DFT-MD over classical MD is its transferability, especially to various charge states. Undoubtedly, as improved functionals and wavefunction based-theories are

incorporated, and as gains in computational capacity allows for use of larger basis sets, the quantitative accuracy will improve.

The multilevel computational approach considered here suggests that the mechanism for the addition of FC radicals to the H-terminated diamond (111) surface does not necessarily depend upon H abstraction. We predict that cationic precursors are less likely to add to the surface unless significant fragmentation occurs. Instead, cationic fluorocarbons preferentially oxidize the diamond surface leaving behind cationic sites, which is likely to significantly influence subsequent film growth.

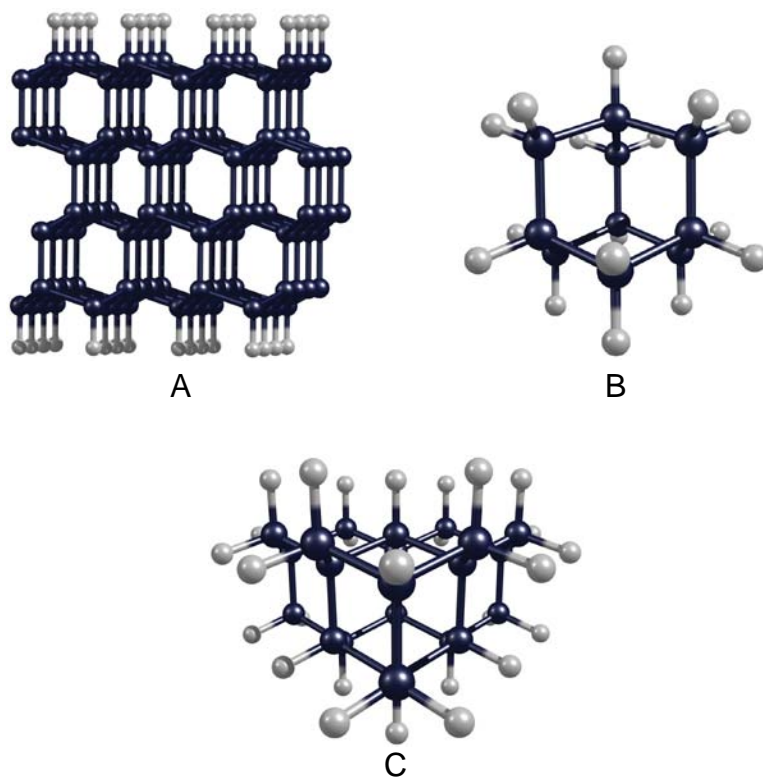


Figure 3-1. Target systems are used for calculation of reaction enthalpies. A) The periodic slab composed of a 160 atom supercell project in two directions is used for both classical and DFT MD simulations. B) The 10 carbon adamantane molecule allows for calculations up to the G3MP2B3 level on a  $sp^3$  hybridized carbon system. C) A 22 carbon atom cluster provides the proper orientation of the surface hydrogen atoms and  $sp^3$  hybridization around the bonding site.

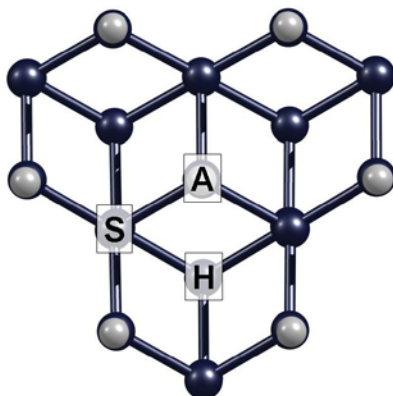


Figure 3-2. Impact sites on the diamond(111) surface. The atop site (A) corresponds to the top surface C atom; the subsurface site (S) is the recessed surface C atom. The hollow site (H) overlays the void in the surface plane.

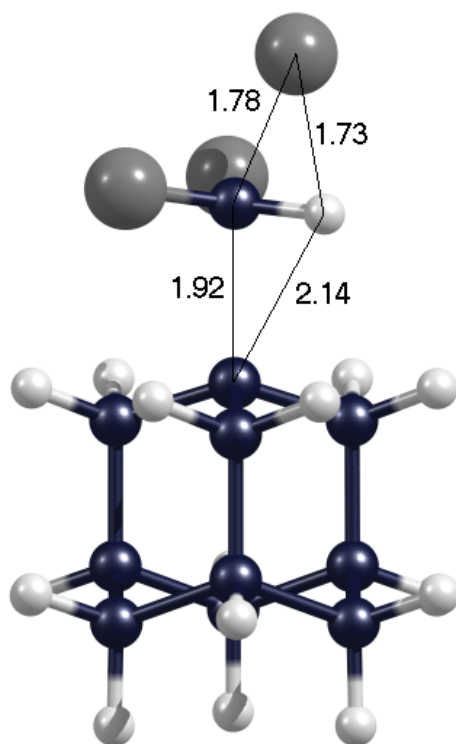


Figure 3-3. The geometry of the transition state when a  $\text{CF}_3$  radical reacts with adamantane to produce a  $\text{CF}_2$  fragment bound to the cluster surface and free HF. Black spheres are C, dark grey is F and light grey is H. Labels correspond to bond lengths in Å.

Table 3-1. Geometric parameters for CF<sub>2-3</sub> radicals and cations.

|                              | Bond Length (Å)     |                      | Bond Angle (Deg.) |         | Improper. Torsion (Deg.) |         |
|------------------------------|---------------------|----------------------|-------------------|---------|--------------------------|---------|
|                              | <sup>a</sup> SIESTA | <sup>b</sup> CCSD(T) | SIESTA            | CCSD(T) | SIESTA                   | CCSD(T) |
| CF <sub>2</sub>              | 1.344               | 1.297                | 103.3             | 104.9   | --                       | --      |
| CF <sub>2</sub> <sup>+</sup> | 1.249               | 1.215                | 123.4             | 124.9   | --                       | --      |
| CF <sub>3</sub>              | 1.345               | 1.314                | 111.0             | 111.3   | 124.0                    | 124.9   |
| CF <sub>3</sub> <sup>+</sup> | 1.259               | 1.230                | 120.0             | 120.0   | 180.0                    | 180.0   |

<sup>a</sup>Computed at the spin-polarized PBE/DZP (SIESTA) and<sup>b</sup>CCSD(T)/cc-pVTZ levels of theory.Table 3-2. Classical MD predicted reactions between CF<sub>3</sub> and diamond (111)

| Reaction  | Probability (%) | Reaction Site |
|---|-----------------|---------------|
| no reaction   | 42.0            | A,H,S         |
| $\cdot CF_3 + C_{Dia} \rightarrow HCF_3 + C_{Dia}$        | 13.7            | A             |
| $\cdot CF_3 + C_{Dia} \rightarrow CF_3C_{Dia} + H$        | 21.7            | A             |
| $CF_3 + C_{Dia} \rightarrow CF_3 + H + C_{Dia}$           | 10.0            | A             |
| $\cdot CF_3 + C_{Dia} \rightarrow CF_2C_{Dia} + H + F$    | 5.0             | A,S           |
| $\cdot CF_3 + C_{Dia} \rightarrow CF_2 + C_{Dia} + F + H$ | 4.0             | A,S           |
| $\cdot CF_3 + C_{Dia} \rightarrow CF_2 + C_{Dia} + F$     | 2.0             | S             |
| $\cdot CF_3 + C_{Dia} \rightarrow FC_{Dia} + CF_2 + H$    | 1.7             | S             |

The *Dia* subscript indicates the periodic hydrogen terminated diamond target.Table 3-3. DFT-MD predicted reactions between CF<sub>3</sub> and the diamond (111) surface.

| CF <sub>3</sub> Radical Reactions                           | Prob.(%) | CF <sub>3</sub> <sup>+</sup> Reactions                 | Prob.(%) |
|---|----------|--|----------|
| no reaction   | 0.0      | $CF_3^+ + C_{Dia} \rightarrow CF_3 + C_{Dia}$          | 20       |
| $\cdot CF_3 + C_{Dia} \rightarrow \cdot CF_3 + H + C_{Dia}$ | 10       | $CF_3^+ + C_{Dia} \rightarrow CF_3 + H + C_{Dia}$      | 10       |
| $\cdot CF_3 + C_{Dia} \rightarrow HF + F + CFC_{Dia}$       | 30       | $CF_3^+ + C_{Dia} \rightarrow CF_3 + 2H + C_{Dia}$     | 10       |
| $\cdot CF_3 + C_{Dia} \rightarrow HCF_2 + HF + C_{Dia}$     | 10       | $CF_3^+ + C_{Dia} \rightarrow CF_2 + 2H + F + C_{Dia}$ | 10       |
| $\cdot CF_3 + C_{Dia} \rightarrow CF_2 + HF + C_{Dia}$      | 20       | $CF_3^+ + C_{Dia} \rightarrow CF_2 + H + F + C_{Dia}$  | 10       |
| $\cdot CF_3 + C_{Dia} \rightarrow CF_2 + H + F + C_{Dia}$   | 20       | $CF_3^+ + C_{Dia} \rightarrow CF_2 + HF + C_{Dia}$     | 10       |
| $\cdot CF_3 + C_{Dia} \rightarrow C_2F_2 + H + F + C_{Dia}$ | 10       | $CF_3^+ + C_{Dia} \rightarrow 2HF + H + CFC_{Dia}$     | 10       |
|   |          | $CF_3^+ + C_{Dia} \rightarrow 2HF + CF + C_{Dia}$      | 10       |
|   |          | $CF_3^+ + C_{Dia} \rightarrow 2HF + F + H + CC_{Dia}$  | 10       |

The *Dia* subscript indicates the periodic hydrogen terminated diamond target.

Table 3-4. Reaction enthalpies (in eV) between CF<sub>3</sub> and adamantane (C<sub>10</sub>)

| Reaction   | SIESTA | *B3LYP | *B98  | *BMK  | G3MP2B3 |
|--|--------|--------|-------|-------|---------|
| 1. $\cdot CF_3 + C_{10} \rightarrow HCF_3 + \cdot C_{10}$          | -0.29  | -0.25  | -0.27 | -0.26 | -0.22   |
| 2. $\cdot CF_3 + C_{10} \rightarrow CF_3C_{10} + H$                | 0.35   | 0.29   | 0.17  | -0.03 | -0.03   |
| 3. $\cdot CF_3 + C_{10} \rightarrow CF_2C_{10} + HF$               | -0.17  | -0.12  | -0.16 | -0.24 | -0.56   |
| 4. $\cdot CF_3 + C_{10} \rightarrow CF_2 + F + H + \cdot C_{10}$   | 8.82   | 8.35   | 8.36  | 8.41  | 8.43    |
| 5. $\cdot CF_3 + C_{10} \rightarrow CF_2 + HF + \cdot C_{10}$      | 2.54   | 2.51   | 2.52  | 2.58  | 2.31    |
| 6. $\cdot CF_3 + C_{10} \rightarrow \cdot CF_3 + H + \cdot C_{10}$ | 4.45   | 4.51   | 4.50  | 4.60  | 4.64    |
| 7. $CF_3^+ + C_{10} \rightarrow CF_2 + HF + C_{10}^+$              | -0.56  | -0.38  | -0.31 | -0.29 | -0.19   |
| 8. $CF_3^+ + C_{10} \rightarrow CF_2^+ + HF + \cdot C_{10}$        | 5.14   | 4.73   | 4.82  | 4.96  | 4.96    |
| 9. $CF_3^+ + C_{10} \rightarrow CF_3C_{10} + H^+$                  | 4.24   | 4.94   | 4.98  | 4.58  | 4.52    |
| 10. $CF_3^+ + C_{10} \rightarrow CF_2C_{10} + H^+ + F$             | 10.1   | 10.4   | 10.5  | 10.2  | 10.1    |
| 11. $CF_3^+ + C_{10} \rightarrow CF_3 + H + C_{10}^+$              | 1.36   | 1.62   | 1.66  | 1.72  | 1.79    |
| 12. $CF_3^+ + C_{10} \rightarrow CF_3 + H^+ + \cdot C_{10}$        | 8.34   | 9.16   | 9.30  | 9.21  | 9.19    |
| 13. $CF_3^+ + C_{10} \rightarrow CF_3^+ + \cdot H + \cdot C_{10}$  | 4.45   | 4.51   | 4.50  | 4.60  | 4.64    |
| 14. $CF_3^+ + C_{10} \rightarrow \cdot CF_3 + C_{10}^+$            | -0.45  | 0.05   | 0.15  | 0.28  | 0.63    |
| Mean Absolute Error (eV)   | 0.36   | 0.23   | 0.22  | 0.10  | --      |

\*Energies are calculated with the 6-311G(2d,p) basis set. Geometries are optimized with B3LYP/6-31G(d).

T=0K

Table 3-5. Reaction enthalpies (in eV) between CF<sub>3</sub> and C<sub>22</sub>

| Reaction   | REBO  | SIESTA | <sup>1</sup> BMK | <sup>2</sup> BMK+ZPE |
|--|-------|--------|------------------|----------------------|
| 1. $\cdot CF_3 + C_{22} \rightarrow HCF_3 + \cdot C_{22}$              | -0.28 | -0.57  | -0.26            | -0.20                |
| 2. $\cdot CF_3 + C_{22} \rightarrow CF_3C_{22} + H$                    | 0.97  | 1.03   | 0.92             | 0.69                 |
| 3. $\cdot CF_3 + C_{22} \rightarrow CF_2C_{22} + HF$                   | 0.11  | 0.05   | 0.28             | 0.11                 |
| 4. $\cdot CF_3 + C_{22} \rightarrow \cdot CF_2 + F + H + \cdot C_{22}$ | 8.41  | 8.54   | 8.43             | 7.98                 |
| 5. $\cdot CF_3 + C_{22} \rightarrow \cdot CF_2 + HF + \cdot C_{22}$    | 2.58  | 2.26   | 2.60             | 2.41                 |
| 6. $\cdot CF_3 + C_{22} \rightarrow \cdot CF_3 + H + \cdot C_{22}$     | 4.58  | 4.17   | 4.61             | 4.38                 |
| 7. $CF_3^+ + C_{22} \rightarrow \cdot CF_2 + HF + C_{22}^+$            | --    | -1.44  | -0.77            | -1.05                |
| 8. $CF_3^+ + C_{22} \rightarrow \cdot CF_2^+ + HF + \cdot C_{22}$      | --    | 4.86   | 4.97             | 4.83                 |
| 9. $CF_3^+ + C_{22} \rightarrow CF_3C_{22} + H^+$                      | --    | 4.92   | 5.54             | 5.31                 |
| 10. $CF_3^+ + C_{22} \rightarrow CF_2C_{22} + H^+ + F$                 | --    | 10.3   | 10.7             | 10.3                 |
| 11. $CF_3^+ + C_{22} \rightarrow CF_3 + \cdot H + C_{22}^+$            | --    | 0.57   | 1.25             | 0.92                 |
| 14. $CF_3^+ + C_{22} \rightarrow \cdot CF_3 + C_{22}^+$                | --    | -1.53  | 0.03             | -0.30                |
| Mean Absolute Error (eV)   | 0.05  | 0.47   | --               | --                   |

<sup>1</sup>BMK/6-311G(2d,p) energies with B3LYP/6-31G(d) geometries<sup>2</sup>Values are corrected for contributions due to ZPE determined via G3B3MP2  
T=0KTable 3-6. Reaction enthalpies (in eV) between CF<sub>3</sub> and a periodic diamond slab.

| Reaction  | REBO | SIESTA |
|---|------|--------|
| 2. $\cdot CF_3 + C_{22} \rightarrow CF_3C_{22} + \cdot H$                     | 0.97 | 1.03   |
| 2. $\cdot CF_3 + C_{Diamond} \rightarrow CF_3C_{Diamond} + \cdot H$           | 0.96 | 1.03   |
| 5. $\cdot CF_3 + C_{22} \rightarrow \cdot CF_2 + HF + \cdot C_{22}$           | 2.58 | 2.26   |
| 5. $\cdot CF_3 + C_{Diamond} \rightarrow \cdot CF_2 + HF + \cdot C_{Diamond}$ | 2.54 | 2.28   |

CHAPTER 4  
METHODOLOGY FOR ATOMISTIC SIMULATIONS OF COPPER OXIDATION USING  
A CHARGE OPTIMIZED MANY-BODY (COMB) POTENTIAL

**4.1 Current Theoretical Models of Copper Oxidation**

Historically, copper has been used as a model system for the fundamental study of early stage oxidation and oxide film growth on transition metal surfaces.<sup>30, 31, 33, 34, 124-126</sup> Notable studies of copper oxidation have been published over the past six decades since copper was included in the original work of Cabrera and Mott.<sup>127</sup> Over that time, as the resolution of experimental capabilities has progressed, findings suggest an intriguingly complex oxidation mechanism that is not yet fully understood. Early studies based on macro-scale techniques suggest that oxidation proceeds via the formation of a uniform passivating film as illustrated by the Cabrera-Mott model.<sup>34, 124</sup> Subsequent electron microscopy experiments indicate a more complicated mechanism that proceeds through island formation, coalescence, and eventually film formation.<sup>32, 125, 128</sup> Current *in situ* electron microscopy experiments, which allow for the direct observation of initial oxidation in controlled atmospheres and are resolved at the atomic scale, have further refined our understanding of the oxidation mechanism. General findings that are consistent throughout a range of studies indicate that oxidation proceeds from chemisorption of atomic oxygen to the formation of an oxygen deficient induction layer that facilitates the growth of three dimensional Cu<sub>2</sub>O islands.<sup>30, 126, 129</sup> The current view is that island growth and coalescence is limited by the surface and interfacial diffusion of oxygen,<sup>30</sup> which is in contrast to the passive film models of oxidation such as Cabrera and Mott, where cation diffusion is rate limiting.<sup>127</sup>

While the current body of experimental work strongly supports a heteroepitaxial growth model limited by oxygen surface diffusion,<sup>30, 126, 130</sup> the details of the mechanism,

especially during the early stages, are not yet clear and are somewhat contradictory in the literature. For instance, *in situ* transmission electron microscopy (TEM) experiments indicated a relationship between island nucleation and step edges.<sup>128, 131</sup> However, a more recent study conducted at higher resolution found no significant dependence of nucleation and growth rates on surface defects and step edges, but did find a significant increase in growth rates at grain boundaries.<sup>35, 36</sup> Diffraction and electron microscopy experiments consistently indicate that Cu<sub>2</sub>O islands form with the [110] plane of the oxide at the interface regardless of the structure of the metal surface upon which it forms.<sup>125, 128</sup> Epitaxial growth oriented along the (110) direction of the metal is preferred.<sup>125, 128</sup> While the termination of the oxide is invariant with the metal surface, the shape of the islands does vary among copper surfaces.<sup>128</sup> More recently, *in situ* TEM experiments indicate that island morphology also varies with reaction temperature.<sup>36, 130</sup> This leads to the promising possibility that if the mechanism of oxidation can be resolved to the point where the dependence of island morphology on reaction conditions is understood that controlled oxidation could be used as a means to direct the morphology of engineered oxide nano-structures.

Resolving the oxidation mechanism requires a theoretical method with the fidelity and capability of efficiently modeling the structures of interest. One choice is an empirical potential that can be incorporated into a molecular dynamics (MD) or kinetic Monte Carlo scheme. First principles methods, such as density functional theory (DFT), have the necessary fidelity but are limited by both the size and the time scale of the problem. Because oxide growth is a diffusion limited process that is influenced by strains at the interface,<sup>37, 132</sup> atomic-scale simulation of the formation of a single small

island involves tens of thousands of atoms, which exceeds the current capacity of traditional DFT methods by at least an order of magnitude. Hence, to enable the study of oxidation on a meaningful length scale, high-fidelity analytical inter-atomic potentials must be used.

Simulations of oxide formation naturally fall under the scope of variable charge potentials that can simultaneously model the oxygen molecule, a metallic solid, and the evolving stoichiometry of the oxide as growth progresses. In choosing a potential form for a metal oxide system, a good first guess would be along the lines of an embedded atom method (EAM)<sup>13</sup> or second moment based potential such as Finnis-Sinclair<sup>21</sup> coupled with an electrostatic model. This exact scheme was pursued by Streit and Mintmire with their electrostatics+ (ES+) model for aluminum and alumina systems,<sup>22</sup> which coupled a variable charge electrostatic scheme to a Finnis-Sinclair bond order potential. The ES+ model has subsequently been extended with some refinement to several additional oxide and alloy systems.<sup>35, 36</sup>

In the case of copper oxide there is significant directionality in the bonding for the most relevant phases. Thus, a potential optimized for covalent interactions, such as the Tersoff's potential,<sup>11, 12</sup> may be used. Several recently published potentials link variable charge electrostatics with extended Tersoff type potentials. For example, Yasukawa *et al.* developed one such potential for the covalent Si-SiO<sub>2</sub> system.<sup>17</sup> This potential form was later refined by Yu *et al.* in their COMB potential to reproduce the SiO<sub>2</sub> phase order.<sup>18</sup> The ReaxFF family of force fields employs a similar approach<sup>16</sup> and has been adapted to several metal-oxide systems, which supports the applicability of this potential form to metal-oxides.<sup>19, 44, 133</sup> A main concern with using a Tersoff based potential is its

applicability to close-packed metals. However, as shown by Brenner, the functional form of Tersoff's bond order potential is algebraically similar to the Finnis-Sinclair's potential with the addition of an angular dependence in the bond order term.<sup>52</sup> The applicability of this potential form to model metallic systems comes from the work of Iwasaki *et al.*, who extended Yasukawa's potential to several metallic systems<sup>15</sup> and, more recently, by Yu *et al.* who developed a modified form of Yasukawa's potential for metallic copper based on Iwasaki's parameterizations.<sup>18</sup> Yu's and Iwasaki's parameterizations provide a starting point from which to develop an analytical potential for the oxide phases.

Copper forms pertinent oxides in two different oxidations states. Oxide islands and the initial oxide layer formed during oxidation of metallic copper are composed of cuprous oxide ( $\text{Cu}_2\text{O}$ ). The oxide forms in a cubic crystal structure with space group  $Pn\bar{3}m$  (Part A of Figure 1).<sup>134</sup> The structure can be viewed as a face centered cubic (FCC) lattice of cations, with anions occupying  $\frac{1}{4}$  of the tetrahedral sites at positions  $(\frac{1}{4}, \frac{1}{4}, \frac{1}{4})$  and  $(\frac{3}{4}, \frac{3}{4}, \frac{3}{4})$ , or as a body centered cubic (BCC) lattice of anions with cations occupying one half of the  $(\frac{1}{4}, \frac{1}{4}, \frac{1}{4})$  positions. This results in 2-fold coordination around each cation with a linear O-Cu-O bond angle. As oxidation proceeds, the oxide phase converts to the monoclinic cupric oxide,  $\text{CuO}$ , that has space group  $C2/c$  (Part B of Figure 1).<sup>135</sup> The linear O-Cu-O bond persists in the higher oxide although the cation is now four-fold coordinated.

## 4.2 Computational Methodology

The underlying potential used in this study is the COMB potential presented in Chapter 2. While the Yasukawa potential and the subsequent COMB formalism can be

parameterized to provide a classical approximation of chemical bonding in the ideal ground state structure, additional bond dependent interactions are required to reproduce the phase order of copper oxide and metallic copper. A similar requirement was found necessary by Yu in the developing the COMB potential for SiO<sub>2</sub> and Cu.<sup>18</sup>

In the current potential, dependence of the bond energy on bond angle and coordination resides solely in bond order function that, in turn, gets smaller with increasing charge. This tends to be problematic for copper oxides, which exhibit directionality in the bonding in both the Cu(I) and Cu(II) oxides. In both CuO and Cu<sub>2</sub>O, the O-CU-O bond angle remains 180° with low coordination around Cu. The bond order terms in  $b_{ij}$  alone are insufficient to stabilize these structures especially with the charge dependence. Instead, additional charge independent angular and coordination terms are added for each bond type.

In Yu's parameterization for metallic copper,  $b_{ij}$  has no angle dependence. Instead, that work uses angular functions based on the first, second and third order Legendre polynomials summed over the nearest neighbors (NN):

$$V_i^{LP}(\cos \theta_{ijk}) = K_{LP}^1 \left( 1 + \sum_{j \neq i, k \neq i}^{NN} \cos \theta_{ijk} \right) + K_{LP}^2 \left[ 1 + \frac{1}{2} \sum_{j \neq i, k \neq i}^{NN} (3.0 \cos^2 \theta_{ijk} - 1.0) \right] + K_{LP}^3 \left[ 1 + \frac{1}{2} \sum_{j \neq i, k \neq i}^{NN} (5.0 \cos^3 \theta_{ijk} - 3.0 \cos \theta_{ijk}) \right] \quad (4-1)$$

$K_{LP}$  are fit parameters. The angle functions in metallic copper stabilize the FCC lattice relative to HCP at nearest neighbor distances. The terms also allow for a better fit for stacking fault energies than what is typically achievable with empirical models. Equation 4-1 can also be used to stabilize the 180° O-Cu-O bond angle that is characteristic of

the two low energy oxide phases and so is incorporated in this work. The parameters,  $K_{LP}$ , are specific to the bond type, i.e. Cu-Cu-Cu in the base metal.

### 4.3 Potential Parameterization

The main goal of parameterization is to faithfully reproduce the surface and mechanical properties of the metal and the relative formation enthalpies of accessible oxide phases while maintaining a reliable degree of transferability to possible non-stoichiometric oxides that may arise during oxidation. To ensure transferability, parameters are determined as a weighted least squares best fit to properties of multiple phases with variation in coordination around the metal. The fitting process is also restricted somewhat in that the potential is an integral part of a family of potentials, which are intended to be compatible with one another. To gain some flexibility in the parameterization, values are defined based on the interaction type. This is a deviation from previous COMB potentials, where interaction parameters were determined from element specific values via mixing rules.<sup>18</sup> However, in that previous work, correction functions that were specific to the interaction type were added to improve the potential performance. Since any gain in transferability is compromised with the correction terms, there is no perceived benefit in restricting the parameterization to atomic based values. Furthermore, in practice, the mixing rules are found to be insufficient to describe critical interactions. For example, the angular coefficients for metals are very weak in the metallic phase. However, the oxide is characterized by a linear O-Cu-O bond that requires a stronger angular term than what is given by the mixing rules.

#### 4.3.1 Parameterization of atomic and metallic copper

The electrostatic self energy terms,  $V^{Self}$ , for copper are determined as a least squares best fit to first principles calculations for ionization potential and electron

affinities. When  $V^{Self}$  is truncated at the second order the values may be derived directly from the first ionization potential and electron affinity provided that the energy of the neutral atom is taken as the zero point. However, we have found that higher order terms are required to model energies beyond the first ionization potential, as is necessary for copper with two relevant oxidation states. The reference states are determined at the coupled cluster level of theory using singlet and doublet, and perturbative triplet excitations, CCSD(t).<sup>88</sup> A correlation consistent triple zeta basis set (cc-pVTZ)<sup>95</sup> is found to be sufficient to reproduce the first electron affinity and up to the third ionization potential to an accuracy that is within limits for empirical potentials. All *ab initio* calculations are performed with the *G03* computation suite.

The starting point for charge independent parameters are taken from Yu *et al.*<sup>18</sup> which in turn are derived from the Iwasaki potential.<sup>15</sup> The cubic phase of  $\text{Cu}_2\text{O}$  is basically an inter-penetrating network that may be stabilized by covalent Cu-Cu bonding.<sup>136, 137</sup> The Cu-Cu interaction in the oxide requires a longer cutoff than was used by Yu *et al.*, which in turn necessitates a refit of several parameters. The copper parameters at neutral charge are determined as the weighted least squares best fit to experimental cohesive energy and lattice parameter of the FCC ground state. The training data set also includes un-relaxed values for the  $C_{11}$ ,  $C_{12}$  and  $C_{44}$  elastic constants, (100), (110) and (111) surface energies and the vacancy formation energy,  $E_F^V$ . The energy vs. isometric strain for the FCC ground state as well as BCC and natural HCP structures are also included in the training data set. Unrelaxed values as well as the energy vs. strain curves were calculated with DFT using the *Vienna Ab-Initio Simulation Package ver. 4.6 (VASP 4.6)*.<sup>138</sup> Energies are determined using the

projector augmented plane wave method (PAW).<sup>74</sup> The PW91 generalized gradient approximation (GGA) is used for the exchange and correlation energies. Kinetic energy cutoff is set at 400 eV. Integration over the Brillouin zone is performed over a 10x10x10 Monkhorst-Pack  $k$ -point mesh. The energy vs. isometric strain is calculated over a range of  $\pm 5\%$  strain and fit to the Rose equation of state<sup>139</sup> which yields an energy vs. strain curve in which the bulk modulus is constant at each point. For fitting purposes, the curves are generated with ionic positions fixed relative to the lattice vectors. The natural equation of state, generated with relaxed ionic positions is used as a final check on the parameterization. Values for cohesive energy and elastic constants differ between calculated and experimental values. To rectify discrepancies between data, the calculated energies and the ground state lattice parameter are scaled to the experimental values using the procedure outlined by Mishin.<sup>140</sup> The lattice parameters for higher energy phases are not include in the training set. Only relative energies to the ground state structure are considered. The atomic specific parameters for copper are tabulated in Table 4-1 and interaction dependent parameters are listed in Table 4-2. Lastly, the bond dependent angular corrections are tabulated in Table 4-3.

#### 4.3.3 Parameterization of Molecular Oxygen

Oxygen parameters for the self energy function  $V^{self}(q)$  are determined as a best fit to the ionization potential and first and second electron affinity of atomic oxygen calculated at the CCSD(t)/cc-pVTZ level of theory. O-O interaction parameters are determined as weighted least squares best fit to energy vs. bond length curve for  $O_2$ ,  $O_2^{1-}$  and  $O_2^{2-}$  with the intent to capture the bond dissociation energy for the different charge states. Reference data for the energies vs. bond length for the anions are also calculated using coupled cluster theory at the CCSD(t)/cc-pVTZ level. Lastly the

polarizability tensor for  $O_2$ ,  $O_2^{1-}$  determined at via CCSD/cc-pVTZ are also include in the training data set. Atomic parameters for oxygen are presented in Table 4-1 and O-O interaction parameters are listed in Table 4-2.

#### 4.3.2 Parameterization of copper oxide

Energies for the oxide phases are fit to the enthalpy of formation,  $\Delta H_f$ , at 0K rather than the cohesive energy. This allows for a comparison between phases of different stoichiometry and charge states.  $\Delta H_f$  is determined as total energy of the oxide phase minus the energy of the reactants in their reference states:  $O_{2(g)}$  and  $Cu_{(s)}$ . Calculations are performed on ideal structures at 0K for comparison to first principles calculations where appropriate. The copper-oxygen interaction parameters and charge dependent copper parameters are fit using a weighted least squares best fit to  $\Delta H_f$  of the cuprite phase of  $Cu_2O$ ,  $CuO$  in the monoclinic ground state and high pressure NaCl and CsCl phases, and the meta-stable paramelaconite phase of  $Cu_4O_3$ . The energy vs. isometric strain and the unrelaxed elastic constants for  $Cu_2O$  are also included in the fitting data set. Additionally, the training set includes the  $\Delta H_f$  of a series of phases with varying coordination: the anti-fluorite of  $Cu_2O$  and  $CuO_2$  as fluorite,  $\alpha$ -cristobalite and  $\beta$ -cristobalite.

As in the case of the metallic phase, formation enthalpies were calculated using DFT using *VASP* 4.6. Energies are determined using the same functional, energy cutoff and k-point mesh as was used for the metallic phase. The equilibrium lattice parameters for the ground state are scaled to experimental values for cuprous and cupric oxide. Energy vs. isometric strain is determined relative to the scaled lattice constant. DFT typically underestimates the  $\Delta H_f$  for copper oxides with reported values around -1.24 eV

compared to experimental values of -1.75 eV.<sup>141, 142, 143</sup> This is mainly due to the over-binding of the O<sub>2</sub> reference state in DFT. In this work, the energy of the O<sub>2</sub> molecule is fit to a higher level of theory, which reproduces the experimental bond enthalpy. With the improved reference state energy for O<sub>2</sub>, the calculated  $\Delta H_f$  for Cu<sub>2</sub>O of 1.78eV deviates from experimental values by 1.6%.

The difficulties with the O<sub>2</sub> reference state in DFT also apply to defect formation enthalpies,  $\Delta H_f^{def}$ .<sup>144</sup> Consequently, values for  $\Delta H_f^{def}$  for point defects and surface energies that provide a reliable comparison to this potential are not available.  $\Delta H_f^{def}$  for point and planar defects are used a qualitative assessment of the final potential parameters.

Finally, charge dependent parameters are fit with the additional constraint that the electronegativity on each atom is equal with  $1.0 \times 10^{-6}$  eV/q in the ideal Cu<sub>2</sub>O structure. This ensures the ground state is a minimum in both real space and charge space. The full list of interaction parameters are tabulated in Table 4-2 and 4-3.

## 4.4 Results and Discussion

### 4.4.1 Properties of Metallic Copper

Properties of the metallic phase as predicted by the potential are compared in Table 4-4 to experimental values as well values calculated from first principles<sup>18</sup> with Mishin's EAM potential<sup>140</sup> and Yu's previous COMB potential<sup>18</sup>. The elastic properties and surface energies are fit to values determined with fixed nuclear positions. The values listed in Table 4-4 are determined with relaxed nuclear positions. The final parameter set reproduces the experimental elastic moduli and the  $C_{11}$  and  $C_{12}$  elastic

constants. However, the  $C_{44}$  elastic constant is significantly lower than the calculated values. This is a weakness of the potential that was also observed by Yu *et al.*<sup>18</sup>

The cohesive energy of the HCP and BCC simple cubic and diamond cubic phases are included in the training set. The values in Table 4-4 are based on optimized structures using the final parameter set. The simple cubic and diamond cubic phases are fit with fairly low weight which is reflected in the larger deviations from calculated values. However, the correct qualitative trends are maintained for these low coordination phases.

The surface energies are determined as the energy per unit area between the 3D periodic bulk and the 2D periodic bulk with vacuum between the surfaces of interest. The relative energies for the (111), (100) and (110) surfaces agree with the values calculated from first principles<sup>18</sup> with a mean error of 3.8%. The surfaces take on a slight charge when relaxed with dynamic charge equilibration that reflects the change in coordination at the surface. This is pictured in Figure 4-2 which shows close packed planes parallel to the (111) surface. The charge alternates between positive and negative with each subsequent plane down from the surface and returns to charge neutrality within seven lattice planes. The graph in Figure 4-2 shows the variation in planar average charge density as determined by the potential. Charge returns to neutral about 10 Å from the surface. As indicated in the figure, the (111) surface takes on a slight negative charge. The values in parentheses in Table 4-4 are determined with a charge of zero on each atom and no dynamic charge equilibration. The results are equivalent indicating the surface charge contributes insignificantly to the total surface energy.

The formation enthalpies for common point defects and the stacking faults in the (111) plane are calculated as a check of the potential. The results are listed in Table 4-4 and compared to published reference values. The calculations for both planar and point defects are performed on a  $36 \times 36 \times 36 \text{ \AA}^3$  supercell with periodic boundary conditions applied in three dimensions; the point defects are optimized at constant volume. The planar defect structures are allowed to relax their volume in the direction normal to the plane of the defect using a steepest descent algorithm. The energies are determined with dynamic charge equilibration. The point defect formation energy is determined relative to the reference state, which is defined as the total energy per atom in the perfect FCC lattice according to the following equation:<sup>21</sup>

$$E_F = nE_{Def} - (n \pm 1)E_{Cu} \quad (4-2)$$

Here,  $n$  is the number of atoms in the defect structure,  $E_{def}$  is the energy per atom in the defect structure, and  $E_{Cu}$  is the energy per atom in the perfect FCC lattice. The predicted formation energies for Cu vacancies and the octahedral interstitial agree with experimental values<sup>145</sup> and other methods. A calculation of the formation energies of the three dumbbell interstitials shows the 100 dumbbell to be the most energetically favorable interstitial, with a defect formation energy of 2.87 eV, in agreement with experimental values.<sup>145</sup>

Trends in the formation enthalpies for the stacking faults reflect trends predicted by the other reference methods. As shown in Table 4-4, the potential predicts a bigger formation energy for the intrinsic stacking fault than the previous COMB parameterization.<sup>18</sup> When compared to the COMB potential, the predicted formation energy is closer to experimental values but differs from DFT values<sup>18</sup> by a greater

degree. The predicted extrinsic stacking fault energy is improved; however, the unstable stacking fault energy is underestimated by the current parameter set relative to all other referenced methods. The stacking fault energies are directly influenced by the Legendre polynomial corrections. A careful fine-tuning of the parameters in subsequent versions of the potential may improve its performance in applications where improved mechanical properties of the metal are required. Here, the angular corrections for the metal are tuned to optimize properties of both the metal and the oxide phase.

As with surfaces, the unstable stacking fault and point defect energies take on a slight charge reflecting the change in coordination. The results of the calculations performed without variable charges are listed in parentheses alongside the charge optimized values in Table 4-4. The fact that the results are equivalent indicates that the effect of charge is very slight. The differences between this parameterization of the COMB potential and that of Yu *et al.* are, therefore, attributable to the refitting of the parameters rather than the inclusion of electrostatic interaction.

#### **4.4.2 Properties molecular oxygen**

The self energy functions for both elements are determined as the least squares best fit to calculated values for electron affinities and ionization potentials. The success of the fit is reflected values listed in Table 4-5.

The potential is able to capture the dissociation behavior of oxygen and its anions as shown in Figures 4-3. COMB predicts the lowest energy state of  $O_2$  to be the  $O_2^{-1}$  anion with a charge of  $-1/2$  on each atom. This concurs with higher level calculations, which predict the lowest energy charge state to be  $O_2^{-1}$ . The  $O_2^{-2}$  is unstable until it dissociates into separate  $O^{-1}$  anions, which also concurs qualitatively with *ab initio* results up to CCSD(t)/aug-cc-pVQZ level of theory. The bond enthalpy for the  $O_2^{-2}$

predicted by COMB deviates from calculated values more than other ions in the training set.

The polarizability of oxygen is fit along with the other electrostatic parameters. The starting point for the fit is the atomic polarizability calculated to be  $0.716 \text{ \AA}^3$  using CCSD(t)/cc-pVTZ. The fitted value of  $0.36 \text{ \AA}^3$  underestimates the atomic values but reproduces the components of the polarizability tensor of the  $\text{O}_2$  molecule that are perpendicular to the bond. The calculated polarizabilities for  $\text{O}_2$  along with calculated bond lengths and enthalpies are listed in Table 4-6.

#### 4.4.2 Properties Copper Oxide

The lattice parameter, formation enthalpy, bulk and shear moduli as well as the  $C_{11}$ ,  $C_{12}$  and  $C_{44}$  elastic constants for  $\text{Cu}_2\text{O}$  were included in the training data set. The accuracy of the fit is reflected in the results listed in Table 4-7. The potential is fit to elastic properties determined with rigid ionic positions; results in Table 4-7 are with relaxed positions. The  $C_{44}$  elastic constant exhibits a large drop due to ionic relaxation and consequently exhibits a larger deviation from the reference values.

For the oxide phases, defect formation enthalpies  $\Delta H_f^{def}$  must consider the chemical potential of species added or removed from the system<sup>142</sup> according to the following equation:

$$\Delta H_F^{Def} = E_{Def} - E_0^{Bulk} \pm \sum_i n_i \mu_i \quad . \quad (4-3)$$

Here,  $\mu_i$  is the chemical potential of species  $i$  and  $n_i$  is the number of atoms of species  $i$  added or removed from the perfect structure to form the defect.  $E_{Def}$  is the energy of the defect structure and  $E^{Bulk}$  is the energy of the perfect structure.  $\mu_i$  depends on the

conditions under which the defect is formed such that  $\mu_i = \mu^* - \Delta\mu$ , where  $\mu^*$  is the chemical potential of the reference state.<sup>142</sup>

For  $\text{Cu}_2\text{O}$  to form the relationship  $2\mu_{\text{Cu}} + \mu_{\text{O}} = \mu_{\text{Cu}_2\text{O}}$  must be true. Furthermore, if we neglect the small dependence on pressure of  $\mu_{\text{Cu}_2\text{O}}$ , then  $2\Delta\mu_{\text{Cu}} + \Delta\mu_{\text{O}} = \Delta H_{\text{f-Cu}_2\text{O}}$ . At the copper rich limit, where  $\text{Cu}_2\text{O}$  is in equilibrium with metallic Cu,  $\mu_{\text{Cu}}$  is equal to the chemical potential of metallic Cu,  $\mu_{\text{Cu(s)}}$ , which in COMB is taken as the total energy per atom in the perfect FCC lattice. At the oxygen lean limit  $\Delta\mu_{\text{Cu}}$  is zero and  $\Delta\mu_{\text{O}} = \Delta H_{\text{f-Cu}_2\text{O}}$ .

<sup>141, 142, 146</sup>

For comparison, values for  $\Delta H_{\text{f}}^{\text{def}}$  are determined at the oxygen lean limit for several point defects; the results are listed in Table 4-7. The relative energies for the oxygen defects,  $V_{\text{O}}$  and  $O_{\text{i}}$  agree qualitatively with the results of first principles calculations.<sup>141, 142, 146</sup> The formation enthalpy for  $V_{\text{Cu}}$  is higher than the experimental reference values. However, here and in the DFT reference values, the  $\Delta H_{\text{f}}^{\text{def}}$  is determined for the charge neutral defect meaning  $V_{\text{Cu}}$  is formed by removing a neutral Cu atom from the ideal crystal. This is unlikely in real systems where an ion is more likely to be removed. A lower energy charged defect most likely accounts for the discrepancy between the experimental and computational results.  $\Delta H_{\text{f}}^{\text{def}}$  for other defects agree qualitatively with the DFT values considering that  $\mu_{\text{O}}$  varies by 0.51 eV between DFT<sup>141</sup> and COMB. Furthermore, COMB allows for calculations on larger structures than are accessible with DFT, where the system is fully relaxed and free of strain,

In a manner similar to point defect calculations, the surface energies of the oxide consider the chemical potential of the species added or removed from the perfect crystal to form the surface.<sup>147</sup>

$$\gamma = \frac{1}{A} \left( G \pm \sum_i n_i \mu_i \right) . \quad (4-4)$$

Here,  $A$  is the surface area and  $\gamma$  is the surface free energy. In the COMB potential, the calculations are performed at 0K where contributions due to entropy are zero to compare with reported DFT values.  $\mu_{Cu}$  and  $\mu_O$  at the oxygen lean limit are used for comparison to reported values under similar conditions.<sup>147</sup> The results are given in Table 4-7 for several surfaces. The (111) surface is the only stoichiometric surface listed in Table 4-7. This surface also gives the smallest deviation between methods.

The properties of CuO are fit with light weight, as the Cu<sub>2</sub>O phase is the main focus of the potential. Modeling CuO is complicated by the symmetry breaking Jahn-Teller distortion that characterizes structures containing d<sup>9</sup> transition metals.<sup>148</sup> The effect can not be modeled with current DFT implementations.<sup>144</sup> Classical potentials have had better success in replicating the effect.<sup>148</sup> In the classical models, the Cu<sup>2+</sup> cation is modeled as an aspherical ion with a distorted neighbor shell. The COMB formalism has two means of replicating asymmetry in the neighbor shell: the Legendre polynomial angle correction and the point dipole model. In this work, the CuO geometry is not fit explicitly. However, the structure was characterized using the final parameter set to see if the COMB formalism offers any advantage in modeling these effects. Results generated with potential are listed in Table 4-8. Without polarization, the potential predicts a monoclinic structure for CuO with a  $\Delta H_f$  comparable to experimental

values.<sup>135</sup> The lattice parameters deviate significantly from the low temperature values.<sup>135</sup> However, the total volume of the structure is comparable to DFT results as shown in Figure 4-4. Polarization does not improve the results as shown the last column in Table 4-8.

Table 4-9 lists  $\Delta H_f$  for several oxide phases. The experimental  $\Delta H_f$  for CuO and Cu<sub>4</sub>O<sub>3</sub> are lower in energy than Cu<sub>2</sub>O<sup>149</sup> indicating that Cu<sub>2</sub>O is only stable under oxygen lean conditions. This is illustrated in Figure 4-4, which plots the energy per unit volume for the three low energy phases. In Figure 4-4 the volume and energy vs. isometric strain for the CuO and Cu<sub>2</sub>O structures compare well with values from DFT.

#### 4.4.3 Behavior of O<sub>2</sub> on the Cu surface

The behavior of O<sub>2</sub> on the Cu (100) surface as predicted by COMB is used as assessment of the potential. The enthalpy of adsorption,  $\Delta H^{Ads}$ , and dissociative adsorption of O<sub>2</sub> on the Cu(100) surface is determined by placing O<sub>2</sub> at several sites and minimizing the structure via a steepest descent algorithm.  $\Delta H^{Ads}$  is determined using an equation similar to Equation 4-13 for  $\Delta H^{Def}$ :

$$\Delta H^{Ads} = E_{Def} - E_{Cu(s)}^{(100)} - \sum_i n_i \mu_i \quad . \quad (4-5)$$

$E^{(100)}$  is the energy of the Cu substrate with a free (100) surface.  $\Delta H^{Ads}$  is determined under oxygen rich conditions, where  $\mu_O = 1/2 E_{O_2(g)}$  and  $\Delta \mu_O = 0.0$ .<sup>142</sup>

The upper row of images in Figure 4-6 shows the initial sites selected for study. The results are compared with values calculated via DFT in Table 4-10. When the initial position of the O<sub>2</sub> molecule is 2 Å above the metal surface, the molecule relaxes to a local minimum that is 2.18 Å above the surface with a  $\Delta H^{Ads}$  of -5.2 eV. The molecule

does not dissociate at this point and only a small charge of -0.092 is transferred to the molecule. When the O<sub>2</sub> is placed 1.8 Å above the surface, the molecule relaxes toward the surface and dissociates at some sites but not at others; the relaxed positions are shown in the lower row of Figure 4-6. The energies in Table 4-10 indicate that the lowest  $\Delta H^{Ads}$  occurs when an O<sub>2</sub> molecule is positioned at a bridge site and relaxes to a state where the O atoms are dissociated and absorbed into neighboring hollow sites. This corresponds to the position labeled Bridge 2 in Figure 4-6. The last row in Table 4-10 lists values of  $\Delta H_{Ads}$  determined with the point dipole contribution turned off. The overall effect of the fairly small, on the order of 0.1 eV. However, the final positions are symmetric, where the point dipoles are very small. The largest effect is seen at the least symmetric final positions. COMB values for  $E_{ads}$  are compared to values determined via first principles. The DFT results give the same relative trends and predict dissociation to the hollow sites as being most energetically favorable. However, the absolute energy values are substantially lower with COMB than as calculated by DFT. This is partly due to the low binding energy of the O<sub>2</sub> molecule in DFT, (-6.3 eV for DFT vs. -5.2 eV in COMB), which effects all enthalpy calculations involving O<sub>2</sub> as a reference state.

Oxygen coverage on the Cu(100) surface and the reconstructions that result have been the subject of numerous theoretical and experimental studies.<sup>25, 39, 150-170</sup> Experimentally, at low oxygen coverage at less than 0.3 monolayers (ML) the surface is characterized by micro-domains formed in a c(2x2) arrangement, which can be describe as a O atoms molecules occupying hollow sites. With a ML coverage of 0.3 and above, the oxidized (100) surface is believed reconstruct into a missing row  $(\sqrt{2} \times 2\sqrt{2})R45^\circ$ . As

a qualitative check quarter, half, and full monolayers (ML) of O<sub>2</sub> molecules are placed on the Cu surface oriented over the bridge sites. The ML covered structures are annealed for 5 ps at temperatures ranging for 0 to 450 K with a 50 K increment. Up to 0.5 ML coverage the O<sub>2</sub> molecules dissociate at the hollow sites at 0 K. The 0.25 ML covered surface is stable up to 500 K. However, oxygen begins to migrate to the subsurface layer at 300 K. The 0.5 ML is stable up to 300 K at which point, O begins to migrate to the first subsurface layer of the Cu substrate and the surface begins to reconstruct. With a full ML of coverage, no dissociation occurs at very low temperatures. The O<sub>2</sub> molecules remain intact up to 250 K where the surface begins to reconstruct. Half and full ML covered surfaces reconstruct, however, it can not be determined what surface they are moving towards on the time scale of the simulation. Instead, the  $(\sqrt{2} \times 2\sqrt{2})R45^\circ$  missing row reconstructed was annealed under the same conditions and found to be stable up to 500 K. The reconstructed surface at 300K is shown in Figure 4-7. The fact that COMB predicts this reconstructed surface to at least be a local minimum is encouraging as it means the potential can be used for the study of oxidation on the experimentally observed surface over a wide range of temperatures.

#### 4.4.4 Simulations of the Cu<sub>2</sub>O(111)||Cu(100) interface

The metal-oxide interface is not well characterized in the literature. This is partly due to the graded nature of the most interfaces, which forms from a reconstructed surface. One means of obtaining an atomically sharp interface is through the electrochemical deposition of Cu<sub>2</sub>O.<sup>171</sup> When deposited on the Cu (100) surface, Cu<sub>2</sub>O forms a film with initial growth in the (111) direction.<sup>171</sup> The resulting Cu<sub>2</sub>O(111)||Cu(100) interface is atomically sharp and suspected to be semi-coherent

although this exact structure has not been confirmed experimentally. As a final check of the potential, a model of the interface is relaxed and annealed at 50, 100, 200, 300 and 450 K. The model consists of a  $35.3 \times 31.4 \times 36.2 \text{ \AA}^3$  supercell containing a 20  $\text{\AA}$  thick slab of  $\text{Cu}_{(s)}$  interfaced with a 15.3  $\text{\AA}$  thick slab of  $\text{Cu}_2\text{O}$ . The periodic boundary conditions are applied in three dimensions; in other words, no vacuum space exists between the slabs, so the periodic image is one of alternating metal and oxide slabs stacked upon one another. The epitaxial relationship between the metal and oxide is  $\text{Cu}_2\text{O}(111)[11\bar{2}]||\text{Cu}(100)[001]$  which gives a lattice mismatch of 3.64% along the epitaxial direction. The slab is annealed under constant temperature and pressure (NPT) for 10ps at each temperature. An MD timestep 0.1 fs was used. The temperature is maintained via a Nose-Hoover thermostat.<sup>103</sup> The system cell is allowed to relax in three dimensions. During relaxation, the symmetry of the supercell is constrained to remain orthorhombic.

The interface is predicted to be stable at all the temperatures considered. The first interfacial layers in both phases rearrange beginning at 100 K suggesting either a lower energy epitaxial relationship or reconstruction exist. Figure 4-8 shows the interface after annealing for 10 ps at 300 K, and the view is along the Cu [100] or  $\text{Cu}_2\text{O}[11\bar{2}]$  direction. During the simulation there is no evidence of a phase transformation beyond the first layer or atomic diffusion between phases suggesting the potential is predicting the correct ground state configuration. There is also only a negligible charge transfer between phases, as indicated in Figure 4-9, which shows the planar average charge density with distance from the interface. The figure indicates that charge transfer is limited to the interfacial region of one Cu layer in the oxide and 1-2 layers in the metal.

## 4.5 Concluding Remarks

Based on results from the simulations and calculations, a potential composed of a short-range bond order potential coupled with variable charge electrostatics appears to be capable of simulating the ground state bonding environments of Cu as both a pure metal and when oxidized to the  $\text{Cu}_2\text{O}$ . The potential also captures the bonding behavior of oxygen as a pure element interacting with  $\text{Cu}_{(s)}$  and when incorporated in the  $\text{Cu}_2\text{O}$  oxide. This enables the large scale simulation of processes such as oxidation of the metal surface or phenomena across the metal oxide interface.

Less certain is the ability of this potential formalism to model bonding in  $\text{CuO}$ , where ligand field effects influence the structure. The potential does predict a monoclinic unit cell for the higher oxide with the correct volume and formation enthalpy. However, the lattice parameters deviate significantly from experimental results. Since the relative energy for the phases are consistent with experimental values, the potential is useful for studies of the initial stages of oxidation up until the formation of  $\text{CuO}$ . Future work should seek to improve the potential in this regard.

Lastly, the simulations performed in the course of this work are only intended to demonstrate the stability and capabilities of the potential formalism. The statistics are not sufficient to draw any quantitative conclusions about the materials themselves. Instead, a more thorough examination of the materials and processes simulated here are left for future work.

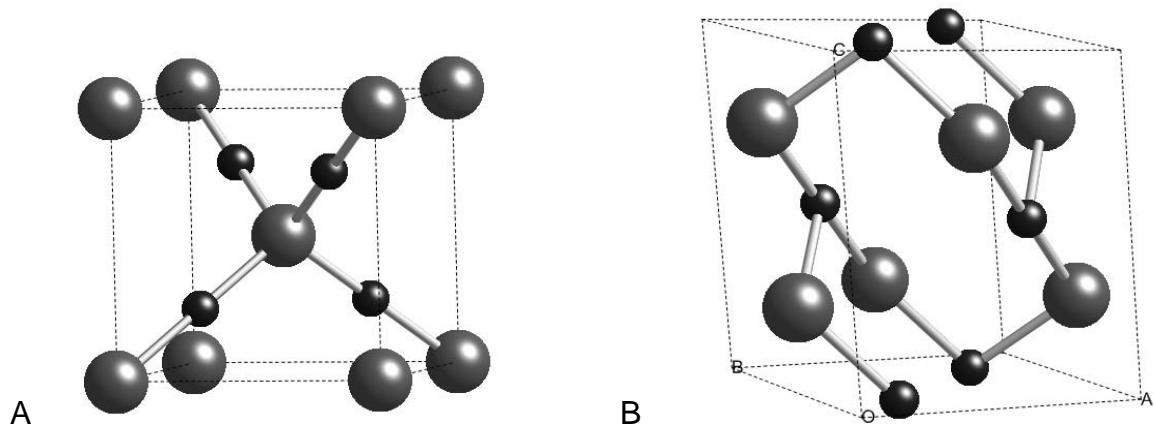


Figure 4-1. Crystal structures for the two low energy oxide phases of copper oxide. Large grey spheres represent and small black spheres are Cu. Cuprous oxide (A) forms a cubic lattice with  $a=4.27\text{\AA}$ . Cupric oxide (B) forms a monoclinic crystal structure with  $a=4.68\text{\AA}$ ,  $b=3.42\text{\AA}$   $c=5.13\text{\AA}$ , and  $\beta=99.6^\circ$ .

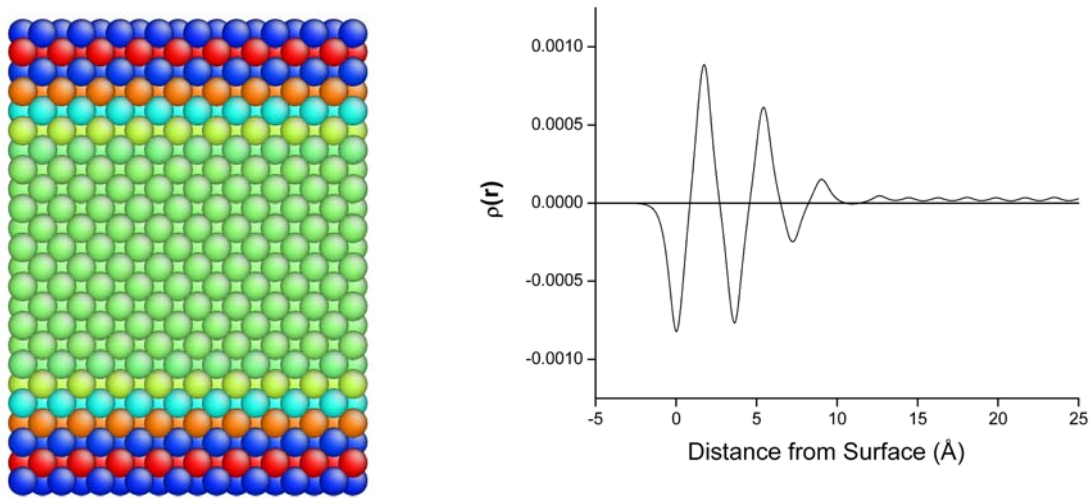


Figure 4-2. Surface charge in metallic copper. The copper surface exhibits negative charge. The charge normal to the  $[111]$  plane is shown. Color corresponds to charge with blue  $= -0.1$  and red  $= 0.1$  charge units. The plot shows the planar charge density distribution normal to the  $[111]$  surface.

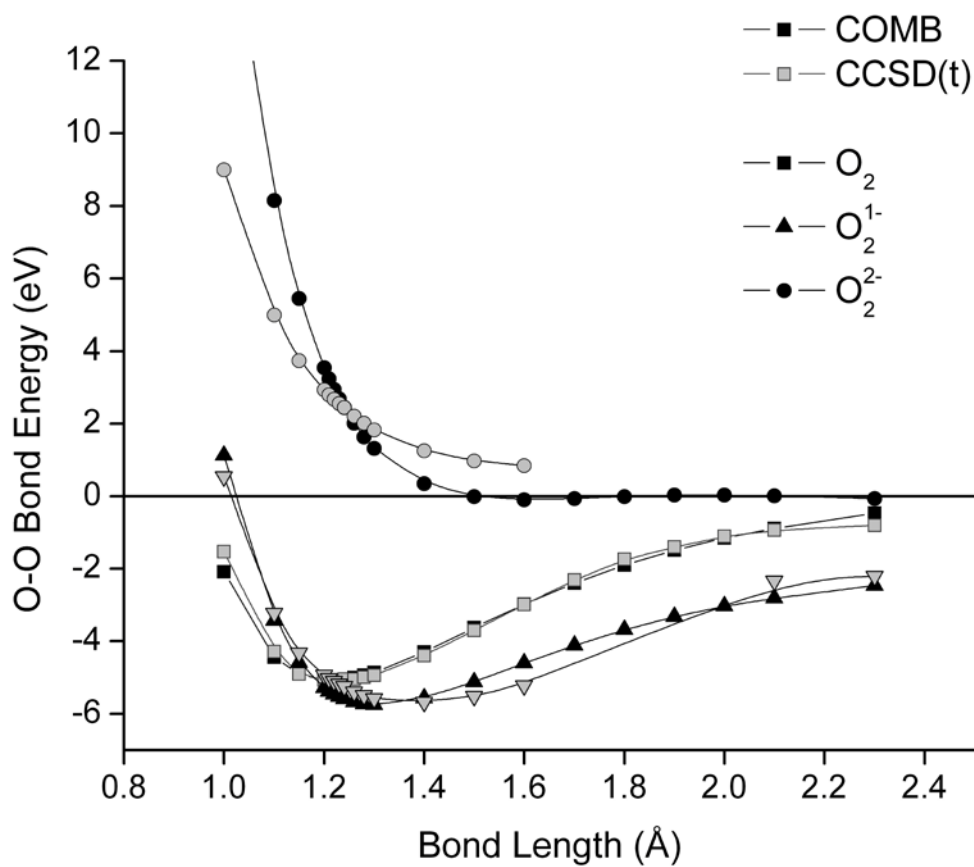


Figure 4-3. The bond dissociation energy of O<sub>2</sub> anions: Black marks are fit values. Grey marks are calculated (CCSD(t)/cc-pVTZ).

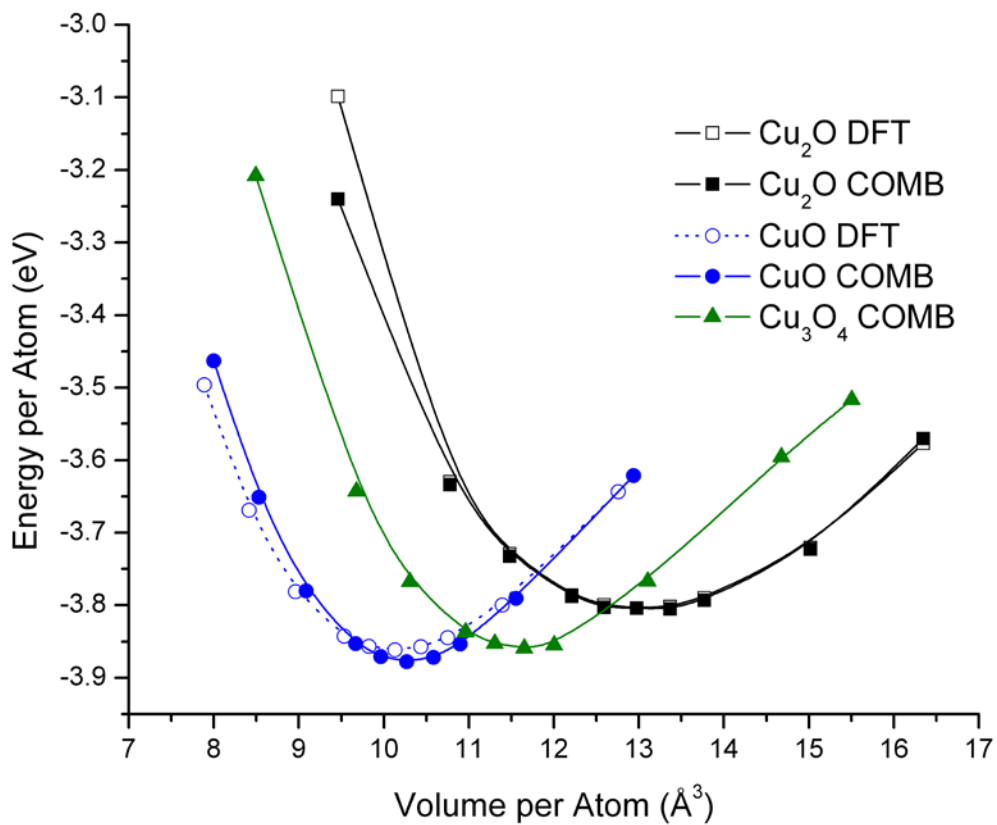


Figure 4-4. The energy per unit volume of the three low energy phases of copper oxide. Filled symbols represent COMB predicted values. Open symbols represent DFT values.

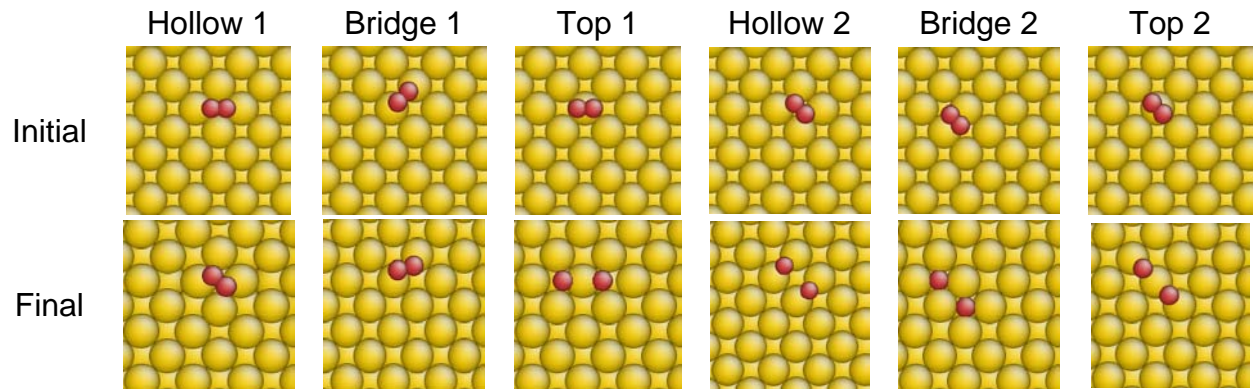


Figure 4-5.  $O_2$  is placed on the Cu(100) surface in the six orientations pictured and relaxed using the COMB potential. The final geometries are shown in the lower row. The small red spheres represent O and the large orange spheres are Cu. Initial orientations are 1.8 Å above the metal surface.

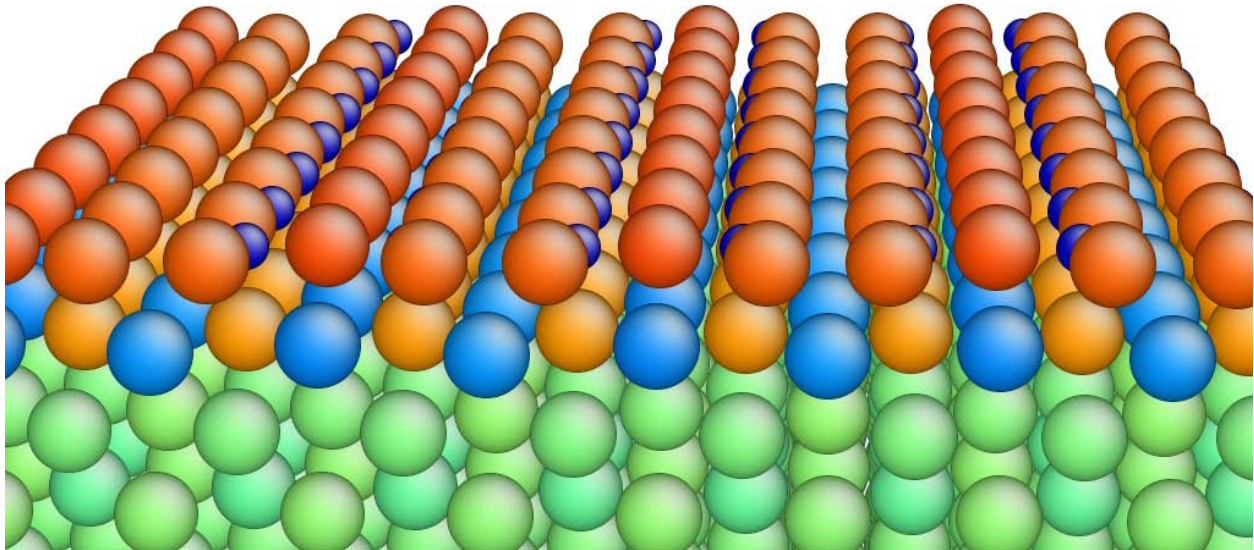


Figure 4-6. The relaxed reconstructed Cu(100) surface with 0.5 monolayer coverage of O<sub>2</sub>. The stable structure has a  $(\sqrt{2} \times 2\sqrt{2})R45^\circ$  missing row configuration. Color corresponds to charge with red=-1.3e and blue=1.3e. The larger spheres are Cu. The smaller spheres nestled in between rows Cu are oxygen. Note the alternating positively and negatively charged rows on Cu atoms on the Cu surface which help to stabilize the structure.

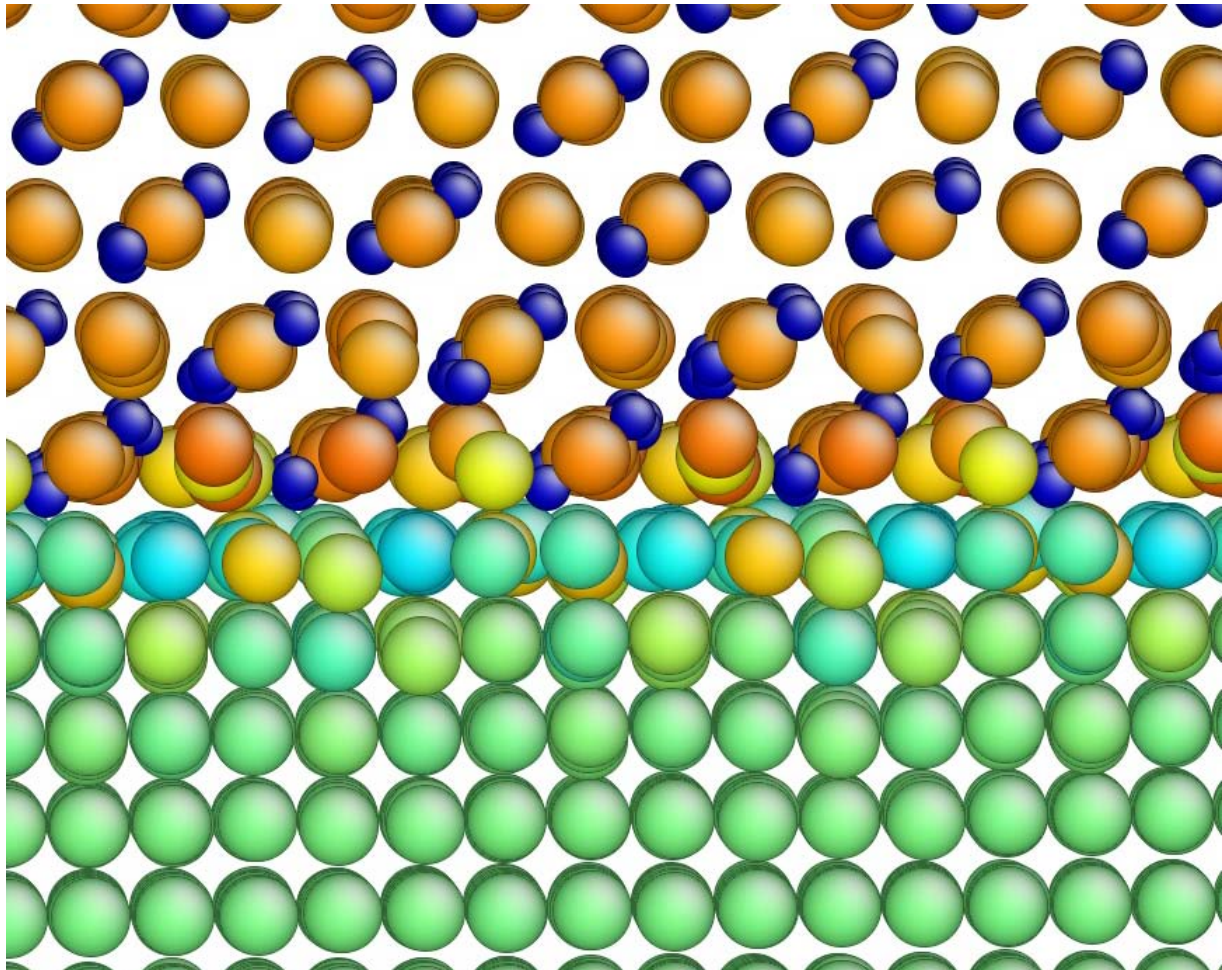


Figure 4-7. The  $\text{Cu}_2\text{O}(111)||\text{Cu}(100)$  interface viewed along the  $\text{Cu}[100]$  direction after annealing at 200 K for 10 ps. Color corresponds to charge with red =  $-1.3 e$  and blue =  $1.3 e$ . The larger spheres are Cu. The smaller spheres are O. The interfacial region where the lattices are disrupted is confined to the first Cu layer in the oxide and one to two layers in the metal.

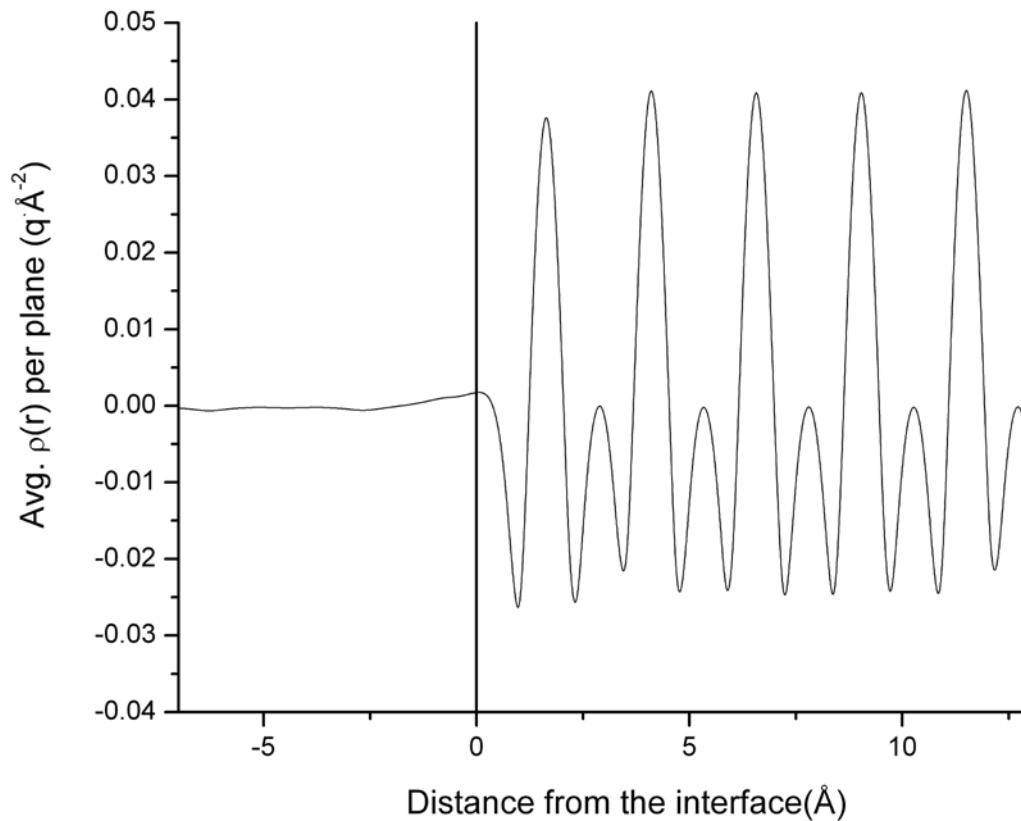


Figure 4-8. Planar average charge density across  $\text{Cu}_2\text{O}(111)||\text{Cu}(100)$  interface after annealing at 200 K for 10 ps. Values are calculated per atom giving the average charge density per atom in each plane parallel to the interface. The zero point in the graph corresponds to the original interface. The oxide phase is on the positive side of the zero point. There is a slight charge transfer between phases at the interface, which is limited to the first 2 planes in each phase.

Table 4-1. Atomic and electrostatic potential parameters

|  | Cu        | O         |
|--|-----------|-----------|
| $\chi$ (eV·q <sup>-1</sup> )                   | 3.768251  | 4.700782  |
| $J$ (eV·q <sup>-2</sup> )                      | 2.966470  | 5.064537  |
| $K$ (eV·q <sup>-3</sup> )                      | 0.515044  | 2.756183  |
| $L$ (eV·q <sup>-4</sup> )                      | 0.257522  | 0.992188  |
| $\xi$ (Å <sup>-1</sup> )                       | 1.476344  | 3.012029  |
| $Z$ (q)  | 0.293153  | 0.030819  |
| $P$ (Å <sup>3</sup> )                          | 0.335000  | 0.323757  |
| $P_1^J$ (eV·q <sup>-3</sup> ·r <sup>-3</sup> ) | -0.470698 | -0.054039 |
| $P_2^J$ (eV·q <sup>-4</sup> ·r <sup>-5</sup> ) | 1.086271  | 1.136518  |
| $D_u$ (Å)                                      | -0.307561 | -1.628749 |
| $D_l$ (Å)                                      | 0.000000  | 0.244020  |
| $Q_u$ (q)                                      | 2.000000  | 6.000000  |
| $Q_l$ (q)                                      | -6.000000 | -2.000000 |
| $CN^*$   | 2.200000  | 4.200000  |
| $\gamma^{Coord}$                               | 0.250000  | 0.249569  |
| $E_{Coord}$ (eV)                               | 0.597603  | 1.934556  |

Table 4-2. Bond dependent potential parameters

|                              | Cu-Cu     | O-O       | Cu-O      | O-Cu      |
|------------------------------|-----------|-----------|-----------|-----------|
| A (eV)                       | 712.3527  | 3523.359  | 598.29837 | 598.29837 |
| B (eV)                       | 102.82614 | 204.62585 | 102.51442 | 102.51442 |
| $\alpha$ (Å <sup>-1</sup> )  | 2.712035  | 5.516839  | 3.129308  | 3.129308  |
| $\lambda$ (Å <sup>-1</sup> ) | 1.467089  | 2.527568  | 1.433963  | 1.433963  |
| $\beta$                      | 0.231055  | 2.00000   | 0.231055  | 0.231055  |
| $\eta$                       | 1.000000  | 1.00000   | 1.000000  | 1.000000  |
| M                            | 1.000000  | 1.00000   | 1.000000  | 1.000000  |
| c (rad.)                     | 0.000000  | 43.560000 | 1.739680  | 2.043622  |
| d (rad.)                     | 1.000000  | 1.000000  | 1.000000  | 1.000000  |
| h (rad.)                     | 1.000000  | -0.220000 | -0.297973 | 0.449820  |
| $n_B$                        | 10.00000  | 10.0000   | 10.00000  | 10.00000  |
| $R_s$ (Å)                    | 3.200000  | 2.2000    | 3.200000  | 3.200000  |
| $S_s$ (Å)                    | 3.600000  | 2.8000    | 3.600000  | 3.600000  |

Table 4-3. Coefficients for Legendre polynomials

|                 | Cu-Cu-Cu | Cu-O-Cu  | O-Cu-O   |
|-----------------|----------|----------|----------|
| $K_{LP}^1$ (eV) | 0.073078 | 0.069535 | 0.635646 |
| $K_{LP}^2$ (eV) | 0.000000 | 0.000000 | 0.635646 |
| $K_{LP}^3$ (eV) | 0.019678 | 0.100428 | 0.000000 |

\*Parameters are equal to zero for all other bond angles.

Table 4-4. Properties of metallic copper

|  | Exp.                 | DFT <sup>g</sup> | EAM <sup>f</sup> | OMB <sup>g</sup> | COMB          |
|--|----------------------|------------------|------------------|------------------|---------------|
| $a$ (Å)  | 3.62 <sup>a</sup>    | 3.64             | 3.62             | 3.62             | 3.62          |
| $E_o$ (eV/atom)  | -3.54 <sup>b</sup>   | -3.50            | -3.54            | -3.54            | -3.54         |
| <i>Bulk Mod.</i> (GPa)                                     | 139 <sup>c</sup>     | 140              | 140              | 139              | 139           |
| $C_{11}$ (GPa)   | 170 <sup>c</sup>     | 173              | 173              | 170              | 171           |
| $C_{12}$ (GPa)   | 123 <sup>c</sup>     | 123              | 123              | 123              | 123           |
| $C_{44}$ (GPa)   | 75.8 <sup>c</sup>    | 80.1             | 76.2             | 49               | 47.7          |
| * $\alpha$ (10 <sup>6</sup> K <sup>-1</sup> )              | 16.5 <sup>b</sup>    |                  |                  | 14.5             | 16.9          |
| <u><math>\Delta E_o</math> Phase Transitions (eV/atom)</u> |                      |                  |                  |                  |               |
| HCP  |                      | 0.006            | 0.008            | 0.008            | 0.008         |
| BCC  |                      | 0.038            | 0.046            | 0.017            | 0.014         |
| Cubic  |                      | 0.47             | 0.43             | 0.49             | 0.38          |
| Diamond  |                      | 1.04             | 1.08             | 0.94             | 0.99          |
| <u><math>\Delta H_f</math> Point Defects (eV)</u>          |                      |                  |                  |                  |               |
| $V_{Cu}$   | 1.28 <sup>d</sup>    |                  | 1.27             | 1.21             | 1.17          |
| $Cu_{i-oct}$   | 2.8-4.2 <sup>e</sup> |                  | 3.06             | 2.41             | 4.93          |
| * $Cu_i$ 100 dumbbell                                      | 2.8-4.2              |                  |                  |                  | 2.48          |
| * $Cu_i$ 110 dumbbell                                      | 2.8-4.2              |                  |                  |                  | 6.91          |
| * $Cu_i$ 111 dumbbell                                      | 2.8-4.2              |                  |                  |                  | 8.58          |
| <u>Planar Defects (mJ·m<sup>-2</sup>)</u>                  |                      |                  |                  |                  |               |
| $\gamma_{(100)}$   | 1780 <sup>f</sup>    | 1478             | 1345             | 1599             | 1478 (1478)** |
| $\gamma_{(110)}$   | 1780                 | 1609             | 1475             | 1646             | 1519 (1519)   |
| $\gamma_{(111)}$   | 1780                 | 1294             | 1239             | 1295             | 1218 (1218)   |
| $\gamma_{ISF}$   | 61 <sup>g</sup>      | 34.3             | 36.2             | 44.4             | 46.3 (46.3)   |
| $\gamma_{USF}$   | 162                  | 210              | 161              | 224              | 105 (105)     |
| $\gamma_{Twin}$  | 24 <sup>g</sup>      | 19.2             | 18.2             | 45               | 23.2 (23.2)   |

\*Indicates predicted values. All other value are included in the training set

\*\*Values in parentheses are determined with charge equilibration

<sup>a</sup>Reference 143

<sup>b</sup>Reference 100

<sup>c</sup>Reference 172

<sup>d</sup>Reference 173

<sup>e</sup>Reference 145

<sup>f</sup>Reference 174

<sup>g</sup>Reference 18

Table 4-5. Ionization potentials (IP) and electron affinities (EA) in eV for Cu and O

| Cu                 | Ab Initio | COMB  |
|--------------------|-----------|-------|
| 1 <sup>st</sup> EA | 1.08      | 1.08  |
| 1 <sup>st</sup> IP | 7.43      | 7.43  |
| 2 <sup>nd</sup> IP | 20.3      | 18.6  |
| <b>O</b>           |           |       |
| 1 <sup>st</sup> EA | 1.40      | 1.40  |
| 2 <sup>nd</sup> EA | -6.08     | -6.08 |
| 1st IP             | 13.5      | 13.5  |

Table 4-6. Properties of molecular oxygen

|  | <i>Ab Initio/ Experimental</i> | COMB  |
|--|--------------------------------|-------|
| Bond Length (Å)  | 1.21*                          | 1.21  |
| Bond Energy (eV)                                       | -5.17*                         | -5.17 |
| <b>Polarizability of O<sub>2</sub> (Å<sup>3</sup>)</b> |                                |       |
| $\alpha^{11}$  | 2.0                            | 2.2   |
| $\alpha^{22}$  | 0.69                           | 0.65  |
| $\alpha^{33}$  | 0.69                           | 0.65  |

\*Reference 143

Table 4-7. Properties of Cu<sub>2</sub>O (cuprous oxide)

|  | Experiment         | First Principles        | COMB  |
|--|--------------------|-------------------------|-------|
| <i>a</i> (Å)   | 4.27 <sup>a</sup>  | 4.31 <sup>e</sup>       | 4.27  |
| <i>E<sub>coh</sub></i> (eV/Cu <sub>2</sub> O)            | 11.3 <sup>b</sup>  | 11.4 <sup>e</sup>       | 11.4  |
| $\Delta H_F$ (eV)  | -1.73 <sup>b</sup> | -1.24 <sup>e</sup>      | -1.75 |
| <i>Bulk Mod.</i> (GPa)                                   | 112 <sup>c</sup>   | 112                     | 111   |
| <i>Shear Mod.</i> (GPa)                                  |                    | 8.15                    | 8.27  |
| <i>C<sub>11</sub></i> (GPa)                              | 123 <sup>c</sup>   | 123                     | 122   |
| <i>C<sub>12</sub></i> (GPa)                              | 108 <sup>c</sup>   | 107                     | 105   |
| <i>C<sub>44</sub></i> (GPa)                              | 12 <sup>c</sup>    | 12.1                    | 57.3  |
| Cu Charge  |                    |                         | 0.54  |
| <u>Point Defects in Cu<sub>2</sub>O (eV)<sup>g</sup></u> |                    |                         |       |
| <i>V<sub>Cu</sub></i>                                    | 0.45 <sup>d</sup>  | 0.28-1.17 <sup>e</sup>  | 2.49  |
| <i>V<sub>Cu_split</sub></i>                              | 0.25 <sup>d</sup>  | 0.78 -1.24 <sup>e</sup> | 2.20  |
| <i>V<sub>O</sub></i>                                     |                    | 1.55 <sup>e</sup>       | 0.95  |
| <i>O<sub>i_tet</sub></i>                                 |                    | 1.36-1.47 <sup>e</sup>  | 0.71  |
| <i>O<sub>i_Oct</sub></i>                                 |                    | 1.69-1.9 <sup>e</sup>   | 2.26  |
| <i>CU<sub>i_tet</sub></i>                                |                    | 1.47 <sup>e</sup>       | 0.95  |
| <i>CU<sub>i_Oct</sub></i>                                |                    | 1.9 <sup>e</sup>        | 0.97  |
| <u>Surface Energies (mJ·m<sup>-2</sup>)<sup>g</sup></u>  |                    |                         |       |
| Cu <sub>2</sub> O(100):Cu                                |                    | 1570 <sup>f</sup>       | 1510  |
| Cu <sub>2</sub> O(100):O                                 |                    | 1070 <sup>f</sup>       | 1030  |
| Cu <sub>2</sub> O(110):Cu                                |                    | 1790 <sup>f</sup>       | 2380  |
| Cu <sub>2</sub> O(110):CuO                               |                    | 417 <sup>f</sup>        | 603   |
| Cu <sub>2</sub> O(111)                                   |                    | 785 <sup>f</sup>        | 783   |

<sup>a</sup>Reference 134

<sup>b</sup>Reference 143

<sup>c</sup>Reference 175, 176

<sup>d</sup>Reference 62

<sup>e</sup>Reference 141, 142, 146

<sup>f</sup>Reference 147

<sup>g</sup>Defect formation and surface energies correspond to oxygen lean conditions.

Table 4-8. Properties of monoclinic CuO

|                   | Experimental       | COMB  | COMB+Polar |
|-------------------|--------------------|-------|------------|
| <i>a</i> (Å)      | 4.68 <sup>a</sup>  | 4.36  | 4.33       |
| <i>b</i> (Å)      | 3.42 <sup>a</sup>  | 3.74  | 3.77       |
| <i>c</i> (Å)      | 5.13 <sup>a</sup>  | 5.04  | 5.05       |
| $\beta$ (Deg.)    | 99.6 <sup>a</sup>  | 97.1  | 97.1       |
| $\Delta H_F$ (eV) | -1.63 <sup>b</sup> | -1.68 | -1.68      |

<sup>a</sup>Reference <sup>135</sup>

<sup>b</sup>Reference <sup>143</sup>

Table 4-9.  $\Delta H_f$  (in eV) of copper oxides

|                                | Structure              | Experimental       | DFT/Simulation     | COMB  |
|--------------------------------|------------------------|--------------------|--------------------|-------|
| Cu <sub>2</sub> O              | Cuprite                | -1.73 <sup>a</sup> | -1.24 <sup>b</sup> | -1.75 |
| CuO                            | Tenorite               | -1.63 <sup>c</sup> | -1.11 <sup>b</sup> | -1.63 |
| Cu <sub>4</sub> O <sub>3</sub> | Paramelaconite         | -4.72 <sup>c</sup> | -5.74 <sup>c</sup> | -5.11 |
| CuO                            | CsCl                   |                    | -0.53 <sup>d</sup> | -0.31 |
| CuO                            | NaCl                   |                    | -1.24 <sup>d</sup> | -1.22 |
| CuO <sub>2</sub>               | $\alpha$ -Cristobalite |                    | -0.30 <sup>d</sup> | -1.58 |
| CuO <sub>2</sub>               | $\beta$ -Cristobalite  |                    | -0.34 <sup>d</sup> | -1.31 |
| CuO <sub>2</sub>               | Fluorite               |                    | -1.29 <sup>d</sup> | -0.49 |
| Cu <sub>2</sub> O              | Anti-Fluorite          |                    | -1.14 <sup>d</sup> | -0.44 |

<sup>a</sup>Reference 143<sup>b</sup>Reference 142<sup>c</sup>Reference 149<sup>d</sup>In house DFT calculationsTable 4-10.  $\Delta H_{Ads}$  (in eV) of O<sub>2</sub> on Cu(100) surface

|             | Hollow 1 | Bridge 1 | Top 1 | Hollow 2 | Bridge 2 | Top 2 |
|-------------|----------|----------|-------|----------|----------|-------|
| DFT         | -2.0     | -2.2     | -2.2  | -2.9     | -4.0     | -2.4  |
| COMB(Polar) | -5.7     | -6.4     | -6.7  | -5.6     | -7.6     | -6.2  |
| COMB        | -5.6     | -6.4     | -6.9  | -5.6     | -7.6     | -6.2  |

## CHAPTER 5 CHARGE OPTIMIZED POTENTIALS FOR ALUMINUM AND ALUMINUM OXIDE SYSTEMS: SUCCESSES, CHALLENGES AND OPPORTUNITIES

### 5.1 Background and Motivation

Aluminum is one the most widely used metals due mainly to its abundance and excellent strength to weight ratio, but also due, in part to the corrosion resistance afforded by a readily forming protective oxide layer.<sup>177</sup> Properties of the oxide layer have long been exploited to enhance the performance of the metal in numerous industrially significant applications such as thermal barrier coatings<sup>178</sup>, corrosion and wear resistant coatings<sup>177</sup>, as well as technologically important applications such as microelectronics and catalysis<sup>179, 180</sup>. In applications that rely on the protective qualities of the coating or where the metal interfaces with another material, performance and failure are often dependent upon interfacial properties and processes. Consequently over the past several decades a significant amount of fundamental and applied research has been devoted to exploring the properties of the metal-oxide interface.<sup>36, 40, 181-188</sup>

Given the significance of this interface, it is a reasonable undertaking to extend the COMB formalism to model these materials. Crafting a potential for composite interfaces with the efficiency and scalability to emulate life-size nano-scale devices is not a trivial task. The challenge is further complicated for Al-Al<sub>2</sub>O<sub>3</sub> systems since the complex crystal structures of aluminum oxides are not amenable to empirical models.<sup>39</sup> While the COMB formalism and similar models are sufficiently flexible to produce a working model of the some aluminas,<sup>40, 189, 190</sup> getting the correct phase order in the ground state requires a well designed potential and a delicate fine tuning of parameters. In the end, all current potentials for this material compromise the accuracy in some properties in

favor of others. The final model developed here is no different from existing potentials in that regard.

This project began as the initial test project for the development of COMB. At the start, the actual form of the potential was not established, so as a first guess, three existing potentials were incorporated in an existing in house code. This was a collaborative effort with three researchers: Alan McGaughey coded up the variable charge potential developed by Streitz-Mintmire, Jianguo Yu coded the Yasukawa potential upon which COMB is based, and Inkook Jang coded a Modified EAM potential. None of the potentials worked very well initially and required significant trial and error to find a reliable potential form. In time, the current COMB model developed as a combination of Streitz and Mintmire's electrostatic functions with Yasukawa's bond order formalism. This current version would not have been settled upon without going through the effort of coding and evaluating all three potentials. In addition to the COMB code, these three researchers and I have written all the fitting and analysis codes used to develop COMB models for new materials. This is a prohibitively burdensome task, which could not have been completed without the efforts of Alan, Jianguo and Inkook.

## **5.2 Challenges with Current Theoretical Models for Alumina**

Experimentally, an oxide layer forms on the metallic Al surface as an amorphous layer of roughly 3-6 nm thickness.<sup>127, 191</sup> The naturally occurring interface formed during thermal oxidation is difficult to characterize at the atomic scale, both computationally and experimentally, since the amorphous interface is graded with mixed stoichiometry over an interfacial region<sup>188</sup>. Consequently, the majority of work at the atomic scale involves ideal interfaces that represent the key aspects of the interface. For example, the most notable experimental characterizations of the solid/solid interface were

performed on the interface formed by the deposition of metallic Al on a crystalline  $\alpha$ - $\text{Al}_2\text{O}_3$  substrate rather than the thermally oxidized metal surface.<sup>181</sup> This approach was used by Medlin *et al.* who used high resolution transition electron microscopy (HR-TEM) to determine the structure and preferred orientation of Al films grown on the (0001) surface of  $\alpha$ - $\text{Al}_2\text{O}_3$ .<sup>188</sup> The work revealed an atomically sharp interface with three predominant heteroepitaxial orientations, with the preferred relationship of  $[\bar{1}10](111)_{\text{Al}} \parallel [10\bar{1}0](0001)_{\text{Al}_2\text{O}_3}$ . This orientation relationship aligns the closed packed planes of the metal with the closed packed oxygen sub-lattice in the oxide. The work of Medlin *et al.* was performed at 200 C; Vermeersch *et al.* report results from a similar experiment at room temperature where they found that growth of the metal film proceeds through the formation of a suboxide layer, to island formation and eventually, to coalescence and film formation.<sup>192</sup> At higher temperature Vermeersch *et al.* observed film growth with the heteroepitaxial relationship of  $[2\bar{1}1](111)_{\text{Al}} \parallel [2\bar{1}\bar{1}0](0001)_{\text{Al}_2\text{O}_3}$ , which is the secondary relationships found by Medlin.<sup>192</sup>

Computational studies based on first principles methods have explored the structure and adhesion of the ideal, atomically sharp interfaces. Batyrev *et al.* used DFT to examine the structure and work of adhesion of the close packed interface in the preferred orientation found by Medlin.<sup>86</sup> Zhang and Smith looked at variation in the stoichiometry and adhesion of this same interface with oxygen partial pressure and found that the ideal termination of the oxide depends on the chemical potential of oxygen.<sup>185</sup> In a similar DFT experiment, Siegle *et al.* compared works of adhesion ( $W_{\text{Sep}}$ ) in the preferred Medlin interface with several terminations of the  $\alpha$ - $\text{Al}_2\text{O}_3$  (0001) surface and found that when the oxide is terminated with a single layer of Al atoms, the

calculated  $W_{\text{Sep}}$  corresponds to experimentally measured values.<sup>184</sup> More recently Hinnemann and Carter looked at the initial stages of film formation by studying the adsorption of Al and O on the  $\alpha\text{-Al}_2\text{O}_3$  (0001) surface using DFT where they found Al prefers to adsorb at the three fold hollow sites with significant charge transfer from the metal atom to the terminal O atoms.<sup>182</sup>

The main limitation with first principles methods is the computational cost. Wilson and Finnis have shown that prediction of the correct structure of the alpha phase requires a high energy cutoff, at least 600 eV.<sup>41</sup> An interfacial study requires a large supercell with sufficient depth in both phases to converge the energy to a consistent point. The computational burden restricts the applicability of first principles methods to ideal, coherent, crystalline interfaces with the preferred orientation of

$[\bar{1}10](111)_{\text{Al}} \parallel [10\bar{1}0](0001)_{\text{Al}_2\text{O}_3}$ . First principles based analysis of semi-coherent interfaces or other heteroepitaxial arrangements is prohibitively expensive.

The development of empirical variable charge potentials that have the computational efficiency to model much larger systems have been pursued over that past decade in response to the limitations in first principles methods. The main difficulty in developing an empirical potential for the Al/Al<sub>2</sub>O<sub>3</sub> interface is finding a suitable potential for the oxide phase. The phase order in alumina has been a challenge for empirical potentials for several decades.<sup>39</sup> Historically, aluminum oxides have been modeled as ionic materials with polarizable ionic potentials, such as core shell or breathing core shell models<sup>80, 193</sup>. Gale *et al.* have shown that these simple polarizable models are unable to predict  $\alpha$ -alumina (corundum) as the low energy phase of Al<sub>2</sub>O<sub>3</sub>.<sup>39</sup>

Instead, the low energy phase is predicted by these potentials to have the more symmetric Bixbyite crystal structure.<sup>39</sup> The two crystal structures are illustrated in Figure 5-1. Part A of the figure shows the hexagonal unit cell of  $\alpha$  phase with space group  $R\bar{3}c$ .<sup>134</sup> The crystal is composed of a partially occupied layer of Al stacked in the (0001) direction and sandwiched between two close packed oxygen sub-lattices. The distinguishing feature of the crystal is short separation distance of 2.66 Å between one pair of cations associated with each Al atom. The smallest cation-cation separation in the oxide is actually smaller than the metallic bond distance in the FCC metal. Part B of Figure 5-1 shows the cubic Bixbyite crystal. The entire structure, with space group  $Ia\bar{3}$ , is built up as a 2x2x2 arrangement of subunits that are similar to a fluorite structure consisting of a close packed FCC Al lattice with O occupying  $\frac{3}{4}$  of the tetrahedral sites.<sup>134</sup> The symmetry is dictated by the relative arrangement of the unfilled tetrahedral sites. The local bonding around each atom is more symmetric in Bixbyite than corundum. Corundum has two Al-O bond lengths of 1.86Å and 1.97 Å, while the ideal Bixbyite structure has one. The bond angles in the Bixbyite structure are also more symmetric. The Al-O-Al bond angles are closer to the ideal tetrahedral angle of 109.47° as shown in Figure 5-2 which compares the distribution of the Al-O-Al bond angles in each material. Bixbyite also has 180° O-Al-O bond angles, which do not occur in the corundum structure.

Gale surmised that the corundum structure may be stabilized with a polarizable potential by including quadrupole moments in addition to the breathing mode on the anion.<sup>39</sup> Around the same time, using DFT, Wilson and Finnis found the Bixbyite structure is favored for alumina up to a cutoff energy of 600 eV beyond which the

corundum structure is predicted.<sup>41</sup> A plot of the difference in the electron density distribution between these two cutoffs reveals that the quadrupole moment of the anions is the distinguishable feature that differs between energy cutoffs.<sup>41</sup> The theory was further confirmed by Wilson who compared a series of classical polarizable potentials that sequentially added a breathing mode, dipole moments and quadrupole moments.<sup>41</sup> The experiment confirmed that the inclusion of the quadrupole moments of the anion can be used to stabilize the corundum structure.

While the quadrupole models successfully predict the correct phase order and appear to be the most transferrable potentials for aluminum oxide, they are limited by a reliance on fixed, formal charges in current versions.<sup>38, 41</sup> This excludes their use from applications containing mixed oxidation states such metal-oxide interfaces. Variable charge schemes reproduce some polarization effects, such as exchange charge polarization between bonded neighbors,<sup>80</sup> which raises the possibility that a potential of this type may be applicable to alumina. However, variable charge potentials for this system have had mixed success in this regard. The first reasonable model was developed Streitz and Mintmire who coupled a variable charge electrostatic potential with a charge independent Finnis Sinclair potential<sup>21</sup> to develop the Electrostatics Plus (ES+) model for Al and Al<sub>2</sub>O<sub>3</sub>.<sup>22</sup> This model fails to predict corundum as the low energy structure.<sup>40, 86</sup> In interface applications, it predicts disordered interfaces characterized by rapid inter-diffusion of O and Al between phases,<sup>22, 187</sup> processes that are not observed experimentally or via first principles calculations.<sup>184, 188</sup> Zhou improved the stability of the ES+ model with barrier functions on the charges and by replacing the short range potential with an EAM model fit to various oxygen coordination

environments.<sup>36</sup> Most recently, Zhang *et al.* published an extended Tersoff based variable charge potential (ReaxFF) for aluminum-alumina systems.<sup>40</sup> In that work, the authors found that neither bond bending nor torsion terms are required to predict the correct phase order of corundum. Instead, they found that correct structure is predicted when dispersion interactions and a penalty function for over coordination are included in the potential.

Zhang's ReaxFF model does not include bond angle dependent contributions and so should describe the same physical interaction as the ES+ model. The difference between these potentials is the inclusion of dispersion interactions and an additional coordination function, which seems to be the key interactions needed to describe the structure of the  $\alpha$  phase. Wilson's polarizable model also includes a large dispersion interaction between oxygen pairs. The quadrupole moments are a small contribution to the total energy, which appear to introduce a short range angular dependence to the energy. Considering the successes of Zhang's and Wilson's models, the COMB formalism appear to be sufficiently comprehensive to model both alumina and its interface with metallic Al.

## 5.2 Parameterization of the COMB Potential

The COMB formalism used in this work is identical to what was described in Chapter 2. The angular term developed in Chapter 4 (Equation 4-1) applies here as well. As with the Cu/CuO potential described in Chapter 4, parameters are determined as a weighted least squares best fit to properties of multiple phases with variation in coordination around the metal to achieve a degree of transferability suitable for the simulations of interfaces.

The same oxygen parameters that were developed in Chapter 4 are used in this study, as well. However, the O-O cutoff distance is extended from 2.2 Å to 3.0 Å so O-O interactions contribute to the energy of the oxide. The dispersion interaction between O-O pairs are also included using the following equation since Zhang and Wilson's methods both indicate the importance of these contributions:

$$V_{ij}^{vdW} = \frac{(P_i^{vdW} P_j^{vdW})^{\frac{1}{2}}}{r_{ij}^6}. \quad (5-1)$$

$P^{vdW}$  are fitted parameters specific to each element. In the final parameter set, the best fit is found with zero values for the dispersion coefficients.

#### 5.4.1 Parameterization of atomic and metallic Al

The electrostatic self energy terms,  $V^{Self}$ , for atomic Al are determined as a least squares best fit to the 1<sup>st</sup>, 2<sup>nd</sup> and 3<sup>rd</sup> ionization potentials and electron affinity calculated at the coupled cluster level of theory using singlet and doublet, and perturbative triplet excitations, CCSD(t).<sup>88</sup> A correlation consistent triple zeta basis set (cc-pVTZ) is found to be sufficient to reproduce the first electron affinity and up to the third ionization potential with sufficient accuracy.<sup>95</sup> All *ab initio* calculations are performed with the G03 computational suite.

The starting point for charge independent Al-Al bond parameters are taken from the Iwasaki potential.<sup>15</sup> The parameters are fit using a weighted least squares best fit to experimental cohesive energy and lattice parameter of the FCC ground state. The training data set also includes un-relaxed values for the  $C_{11}$ ,  $C_{12}$  and  $C_{44}$  elastic constants, (100), (110) and (111) surface energies and the vacancy formation energy. The energy vs. isometric strain for the FCC ground state as well as BCC and natural

HCP structures were also included in the training data set. Unrelaxed values as well as the energy vs. strain curves were calculated with DFT using VASP 4.6. Energies are determined using the PAW method. The PBE functional is used for the exchange and correlation energies. Kinetic energy cutoff is set at 700 eV. Integration over the Brillouin zone is performed over a 10x10x10 Monkhorst-Pack  $k$ -point mesh. The energy vs. isometric strain is calculated over a range of  $\pm 1\%$  strain and fit to the Rose equation of state<sup>139</sup> which yields an energy vs. strain curve in which the bulk modulus is constant at each point. For fitting purposes, the curves are generated with ionic positions fixed relative to the lattice vectors. The natural equation of state, generated with relaxed ionic positions is used as a final check on the parameterization. Values for cohesive energy and elastic constants differ between calculated and experimental values. To rectify discrepancies between data, the calculated energies and the ground state lattice parameter are scaled to the experimental values using the procedure outlined by Mishin<sup>140</sup>. The lattice parameters for higher energy phases are not include in the training set. Only relative energies to the ground state structure are considered. The atomic specific parameters for Al are tabulated in Table 5-1 and interaction dependent parameters are listed in Table 5-2.

The bond dependent angular corrections are fit to the intrinsic, unstable and twin stacking fault energies ( $\gamma_{SF}$ ,  $\gamma_{US}$  and  $\gamma_T$ ), as well as, the energy difference between the FCC and HCP phases and the elastic constants. Results are listed in Table 5-3.

Dispersion is not explicitly included in the Al-Al interactions since the current potential form cannot model the change in these interactions with charge. Explicit inclusion of dispersion between cation pairs would require the simultaneous fit of both

metal and oxide properties, which is considerably more expensive and requires a compromised solution for at least one phase. Instead, dispersion interactions in the charge neutral ground state are assumed to be included in the empirical parameterization on the Al-Al interactions. In the oxide, dispersion interactions are assumed to be smaller between the less polarizable cations, an effect that is captured by variation in the short range attraction terms with charge.

#### 5.4.2 Parameterization of aluminum oxide

The Al-O interaction parameters, charge dependent Al parameters and bond angles dependent terms are fit using a weighted least squares best fit to the  $\Delta H_f$  for  $\alpha$ - $\text{Al}_2\text{O}_3$ , Bixbyite and  $\theta$ - $\text{Al}_2\text{O}_3$ , as well as, AlO as NaCl.  $\text{O}_{2(g)}$  and  $\text{Al}_{(s)}$  are used as the reference states. The un-relaxed elastic constants, bulk and shear moduli for  $\alpha$ - $\text{Al}_2\text{O}_3$  as well as the energy vs. isometric strain are also included in the fit. As in the case of the metallic phase, relative energies of the reference systems are calculated using DFT. Again, the PBE functional is used for the exchange and correlation energies. Kinetic energy cutoff is set at 700 eV. Integration over the Brillouin zone is performed over a 6x6x6 Monkhorst-Pack  $k$ -point mesh. The equilibrium lattice parameters are scaled to experimental values for  $\alpha$ - $\text{Al}_2\text{O}_3$ . Energy vs. isometric strain is determined relative to the scaled lattice constant. The full list of interaction parameters are tabulated in Table 5-2.

$\Delta H_f^{def}$  for point and planar defects are used as qualitative assessment of the final potential parameters rather than included in the training data set since these values subject to the choice and accuracy of the reference states.<sup>194</sup>  $\Delta H_f^{def}$  is determined as a small energy difference between two bulk phases. In practice, large variations in these

values arise with small changes in the bulk energy, which make fitting to them particularly difficult.

All charge dependent parameters are fit with the constraints that the electronegativity of each site is equal within  $1.0 \times 10^{-6}$  eV/q, where q is a formal charge unit, in the  $\alpha$  phase at 0 K. Furthermore, the electronegativity in the ideal structure is fit to be equal to zero meaning atomic charges correspond to a minimum in the energy with respect to charge without constraints. This is an arbitrary condition where one could expect the actual oxide phase to be either electropositive or electronegative. However, by ensuring that the ideal structure corresponds to a minimum in the total energy, aberrant phases, such as Bixbyite, naturally form at higher energies. This condition is found to be necessary to raise the energy of the Bixbyite phase relative to the alpha phase.

## **5.5 Results and Discussion**

### **5.5.1 Properties of metallic aluminum**

Properties of the metallic phase as predicted by the potential are compared to experimental and calculated reference values in Table 5-4. The elastic properties and surface energies are fit to values determined with fixed nuclear positions. Values listed in Table 5- 4 are determined with relaxed nuclear positions. The cohesive energy of the HCP and BCC simple cubic and diamond cubic phases are included in the training set. The values in Table 5-4 are based on optimized structures using the final parameter set. The simple cubic and diamond cubic phases are fit with fairly low weight, which is reflected in the larger deviations from calculated values. Qualitative trends are maintained with these low coordination phases.

The surface energies are determined as the energy per unit area between the 3D periodic bulk and the 2D periodic bulk with vacuum between the surfaces of interest. Relative energies for the (111), (100) and (110) surface agree with values calculated from first principles<sup>40</sup> with a mean error of 1.0%. As with metallic Cu, in Chapter 4, surfaces take on a slight negative charge when relaxed with dynamic charge equilibration reflecting the under-coordination at the surface. The charge alternates between positive and negative with each subsequent plane down from the surface and returns to charge neutrality within 10 lattice planes. As with Cu, the surface charge does not make a detectable contribution to the total surface energy.

The formation enthalpies for a common point defects and the stacking faults in the [111] plane are calculated with relaxed ionic positions as a check. Results are listed in Table 5-4 with comparison to reference values. Calculations for both planar and point defects are performed on a 36x36x36 Å<sup>3</sup> super cell with periodic boundary conditions applied in three dimensions. Point defects are optimized at constant volume. Planar defect structures are allowed to relax their volume in the direction normal to the plane of the defect using a steepest descent algorithm. Energies are determined with dynamic charge equilibration.

The point defect formation energy is determined relative to the reference state defined as the total energy per atom in the perfect FCC lattice according Equation 4-1. The predicted formation energies for Al vacancies and the octahedral interstitial agree with experimental values and other methods.<sup>40, 140</sup> A calculation of the formation energies of the three dumbbell interstitials shows the 100 dumbbell to be the most energetically favorable interstitial, with a defect formation energy of 2.50 eV.

Trends in the formation enthalpies for the stacking faults reflect trends predicted by other methods as shown in Table 5-4, with the exception that the potential predicts a large formation energy for the unstable stacking fault. The stacking fault energies are directly influenced by the Legendre polynomial corrections. In this fit, the angle functions also affect the phase order, elastic constants and surface energies. The best solution results in a larger value for  $\gamma_{US}$ . Future re-fitting may address this weakness and improve the performance of the potential in regards to mechanical properties.

### **5.5.2 Properties of aluminum oxide**

The self energy functions in COMB are fit directly to the atomic ionization energies. The accuracy of the fit are reflected in the calculated values listed in Table 5-5. In previously published potentials, there are two approaches to fitting self energy functions. The method followed by Rappe and Goddard<sup>14</sup> and in the subsequent ReaxFF potential<sup>40</sup> fits the self energy to second order to atomic ionization values. Other potentials such as the ES+ model and the first generation COMB potential<sup>18</sup> fit the self energy term to properties of the bulk phases. Here, the approach of Rappe and Goddard is followed since one intended use of the potential is the study of oxidation, where interactions of single atoms with the surface are important. However, the function is terminated at fourth order rather at second order as in Rappe and Goddard.

The bulk and elastic constants are include in the training data set and so are fit directly. The final values are tabulated in Table 5-6 in comparison to experimental and first principles values, as well as published values determined with ReaxFF and the ES+ potentials. The values for the elastic constants and moduli in Table 5-6 are determined

with relaxed ionic positions. Overall, the bulk and elastic constants are comparable to other potential and the reference data.

Calculated values for  $\Delta H_f^{def}$  for charge neutral point defects are listed in Table 5-6 and compared to published calculations. The reference values are from Hine *et al.*<sup>194</sup> and are determined using Equation 4-3 under oxygen lean conditions at T=2371 K and  $p_{O_2}=0.2$  atm. Reference states are Al<sub>(s)</sub> and O<sub>2(g)</sub>. The values in Table 5-6 are not corrected for  $\Delta\mu_o$  as is the case in Hine *et al.*<sup>194</sup>

Zhang *et al.* have shown through first principles calculations that under oxygen lean conditions the preferred termination of the (0001) surface of  $\alpha$ -Al<sub>2</sub>O<sub>3</sub> the interface is with a single Al layer.<sup>185, 186</sup> This observation agrees with experimental data obtained on the clean surfaces under ultra-high vacuum.<sup>181, 195</sup> In the presence of hydrogen or at higher oxygen partial pressures, O terminated surfaces are favored.<sup>181</sup> The single Al terminated surface is stoichiometric and so provides a direct comparison between calculations without the need to consider the chemical potential of species added or removed to form the surface. For these reasons, the (0001) surface energy,  $\gamma_{(0001)}$ , of the single Al terminated surface is used as a check of the potential. The calculated value is 1.82 J·m<sup>-2</sup>. With first principles, functionals based on the local density approximation (LDA) tend to give higher values around 2.2 and GGA functionals give lower values around 1.6.<sup>184, 185</sup> The COMB result falls between these two levels of theory.

The COMB formalism stabilizes the corundum structure relative to Bixbyite by 0.74 eV/Al<sub>2</sub>O<sub>3</sub>, which is inline with first principles calculations.<sup>19</sup> The potential is fit to both the Bixbyite and  $\theta$  phases similarly to Wilson's and Zhang's potentials.<sup>19, 41</sup> These

other phases lie close in energy to the  $\alpha$  phase. The potential is unable to stabilize the  $\theta$  phase relative to Bixbyite as shown in Figure 5-3, which plots the energy vs. volume for several oxide phases. In Figure 5-3, the  $\theta$  phase remains continuously above the  $\alpha$  curve indicating that, with this parameterization, the  $\theta$  phase would never form. This is a weakness of the current model, which indicates limited transferability of the potential to other phases.

The rocksalt structure of AlO is included in the fit. A coordination correction function (Equation 2-129) is required to destabilize this phase relative to the  $\alpha$ . This structure is predicted to be the lowest energy configuration in terms of energy per atom with the ES+ model. Calculations using the ES+ potential within our in house code predict this phase to be 0.71 eV/atom lower in energy than the  $\alpha$  phase, which leads to rapid diffusion of Al atoms from the bulk metal into the oxide during interfacial simulations. A similar effect occurs within COMB if the coordination based correction functions are set to zero.

Polarizability is introduced via the point dipole model described in Chapter 2. As a check of the effect of polarization, the Bixbyite phase was optimized with polarization both enabled and disabled. When the point dipole model is active, the Bixbyite structure is further destabilized by 0.23 eV/ $\text{Al}_2\text{O}_3$ , indicating that the point dipoles have some effect on the phase order. The time per iteration is roughly doubled with the point dipoles enabled for the entire system. Since polarization is not necessarily required to stabilize corundum, polarization is disabled in all subsequent calculations.

### 5.5.3 Properties of the Al(111)|| $\alpha$ -Al<sub>2</sub>O<sub>3</sub>(0001) interface

To test the reliability of the potential in interfacial applications,  $W_{Sep}$  was determined for the several variations of the  $[\bar{1}10](111)_{Al}||[10\bar{1}0](0001)_{Al_2O_3}$  interface.  $W_{Sep}$  is a measure of the interfacial energy defined as:

$$W_{Sep} = E_{Al_2O_3+Slab}^{Tot} - E_{Al_2O_3}^{Tot} - E_{Al-Slab}^{Tot} \quad (5-2)$$

The calculation is performed on a supercell consisting of a periodic slab of Al metal interfaced with a slab of Al<sub>2</sub>O<sub>3</sub>. Periodic boundary conditions are applied in three dimensions so the structure actually consists of alternating films of Al and Al<sub>2</sub>O<sub>3</sub> sandwiched together. Each slab is 40Å thick. Previous theoretical studies on this interface conclude that the most stable interface under oxygen lean condition is formed with a single Al atom terminating the oxide layer.<sup>40, 184-186</sup> The same interface termination is used here for comparison to these studies

There are six possible variations of the single Al terminated interface. The first layer of the Al slab (Al<sub>1</sub>), can be oriented over three unique sites on the  $\alpha$ -Al<sub>2</sub>O<sub>3</sub>(0001) surface relative to the oxygen sub-lattice. These sites are illustrated in Figure 5-4 where the Al slab can be aligned with an FCC (F) or HCP (H) orientation or directly on top (O) of the terminal oxygen layer. Furthermore, as shown in Figure 5-5 with each configuration of the first Al layer, the second Al layer in the slab (Al<sub>2</sub>) can be oriented over either of the two sites not occupied by Al<sub>1</sub>. The combination results in six variations in interfacial structure.

The six interfaces were annealed at 50 K for 10 ps and optimized using a steepest decent algorithm. The  $W_{Sep}$  and the relaxed interfacial separation distance,  $D_o$ , are compared to other published values in Table 5-7. The resulting values indicate

that the potential predicts very little reconstruction of the interface in comparison to DFT.<sup>184</sup> The values for both  $D_o$  and  $W_{Sep}$  are comparable to unrelaxed interfaces.

Additionally, the highest and lowest energy interfaces are plotted in Figure 5-6. The two images are nearly identical, showing very little reconstruction and some charge transfer between phases. The average distribution of atomic planes normal to the interface for the low energy interface is plotted in Figure 5-7. The distribution indicates very little alteration of the structure at the interface. Average charge density per unit area is also plotted in Figure 5-7. The density plot indicates a slight charge transfer between phases at the interface.

The current parameterization predicts less reactivity at the interface than is indicated by first principles calculations. Annealing at high temperature does not initiate reconstruction suggesting that the interfacial geometries predicted by first principles based methods lie high in energy than what is predicted by COMB.

### **5.5 Concluding Remarks**

This work has demonstrated that the COMB formalism has sufficient flexibility to model aluminum oxides. The main challenge in modeling this material is predicting the correct ground state structure. COMB is able to be parameterized to favor the correct ground state configuration. In the version presented here, less emphasis was placed on the other naturally occurring low energy phase such as  $\theta$ . The lack of emphasis, in turn, leads to the  $\theta$  phase being too high in energy to the point where it does not form. In a similar way, the parameterization may have raised the energy of the DFT predicted relaxed interfaces thus inhibiting any reconstruction at the interface. However, further investigation is required before any conclusion can be made in that regard.

The potential reproduces the properties of the metal and its surfaces. It also makes use of the O<sub>2</sub> parameterization developed in Chapter 4 for copper oxides. Together, both parameterizations extend the applicability of the current potential to the study of oxidation of Al.

The main difference between ReaxFF and the ES+ model, according to the published models, is the inclusion of dispersion interactions and the over coordination penalty functions in ReaxFF. Both of these interactions are considered in this work. The coordination functions are set to only affect over-coordinated anions in the oxide, which, in turn, destabilizes the NaCl phase. The best fit for the dispersion interactions is zero in this work, which suggests any dispersion contributions are already incorporated in other interactions. In this work, the Bixbyite phase is penalized with angular terms that also penalize all other phase. In future work, a better solution may arise with a bit more emphasis on the other oxide phases and a better representation of dispersion interactions.

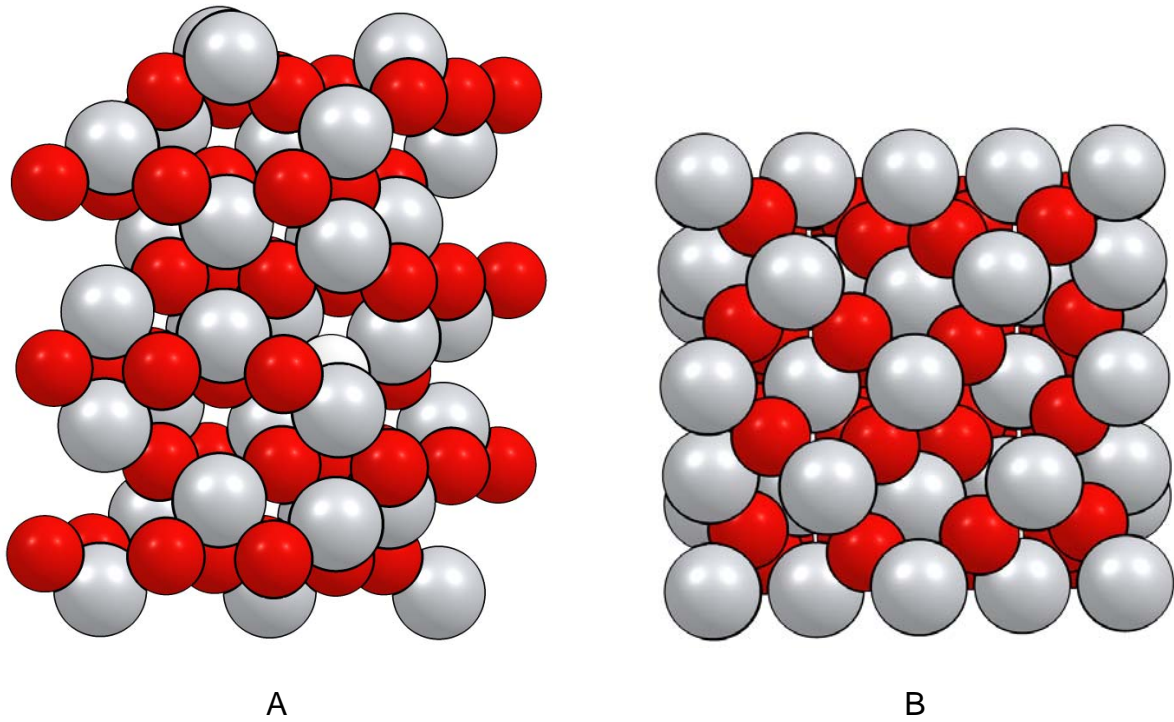


Figure 5-1. The crystal structure of  $\alpha\text{-Al}_2\text{O}_3$  (A) has a hexagonal unit cell of space group  $R\bar{3}c$ . Most empirical potentials incorrectly predict the cubic Bixbyite (B) crystal structure with space group  $Ia\bar{3}$  to be the ground state structure of  $\text{Al}_2\text{O}_3$

## Al-O-Al Bond Angle Distribution

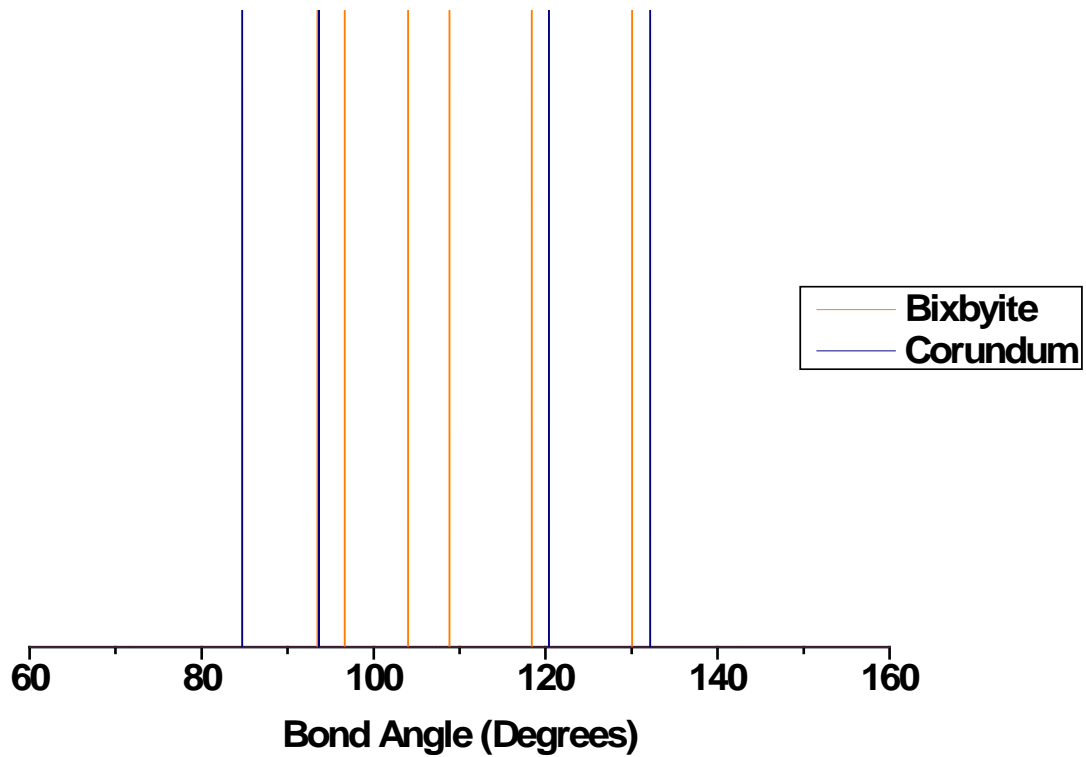


Figure 5-2. The Al-O-Al bond angle distribution in corundum (blue) and Bixbyite (orange). The bond angles around O in the Bixbyite structure are closer to the ideal tetrahedral angle of  $109.47^\circ$  than in corundum.

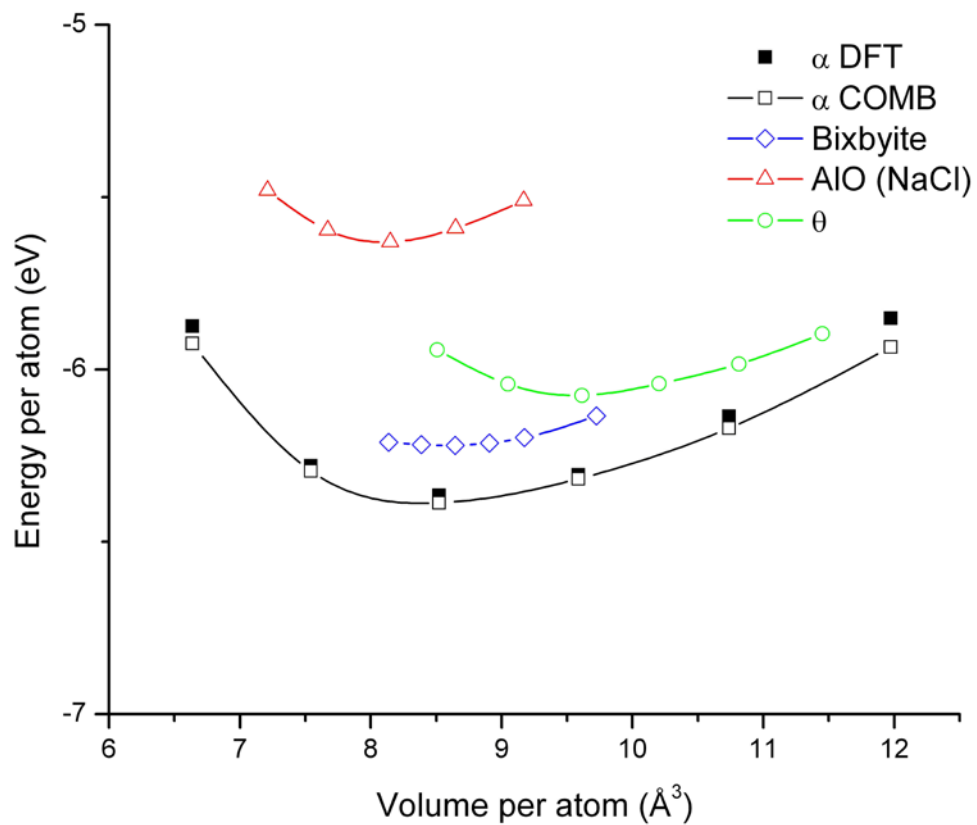


Figure 5-3. The energy vs. volume of several aluminum oxide phases. The ground state is the  $\alpha$  phase (black). Solid black point are determined with DFT (PBE). Open symbols are values determined using the COMB potential. Bixbyite (blue) is shifted above the ground state but lies below  $\theta$ - $\text{Al}_2\text{O}_3$  (green). AlO in the NaCl lattice (red) is shifted up with a coordination penalty function.

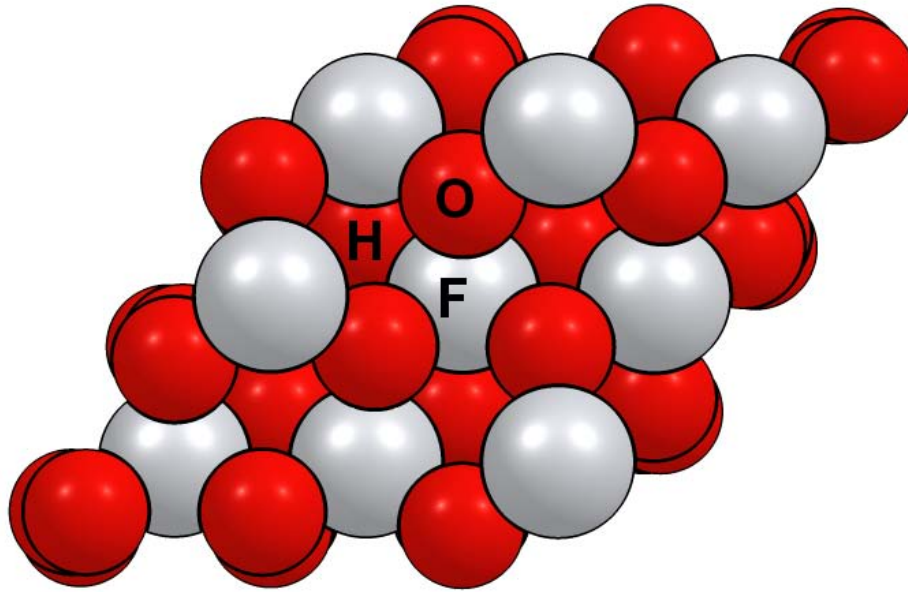
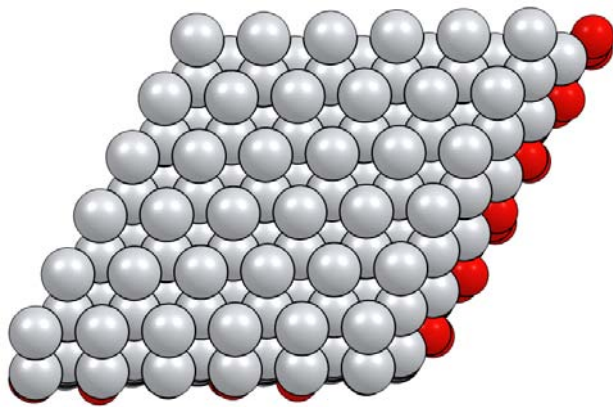
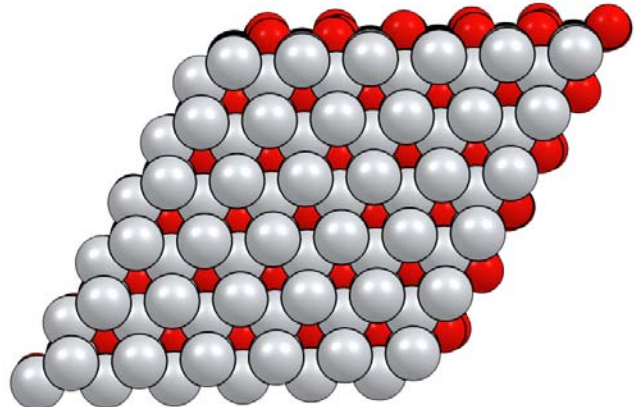


Figure 5-4. A closed packed plane of Al atoms can add to the  $\alpha$ - $\text{Al}_2\text{O}_3$  (0001) at three locations. Relative to the oxygen sub-lattice, atoms can be added with an FCC (F) orientation, HCP (H) orientation or directly on top (O) of the O atoms on the surface.

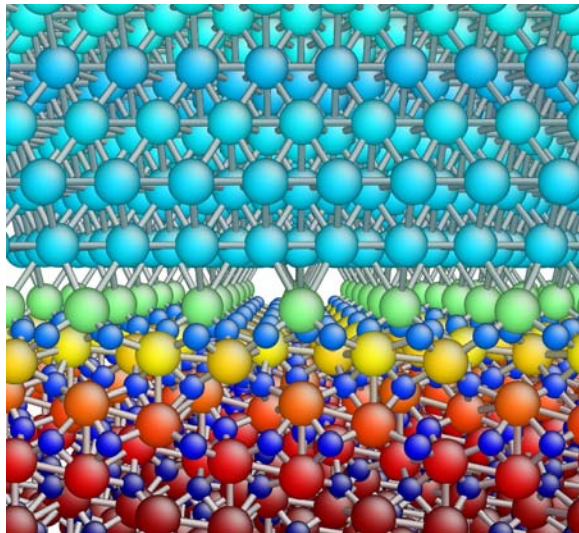


A.  $Al_1^O Al_2^H$

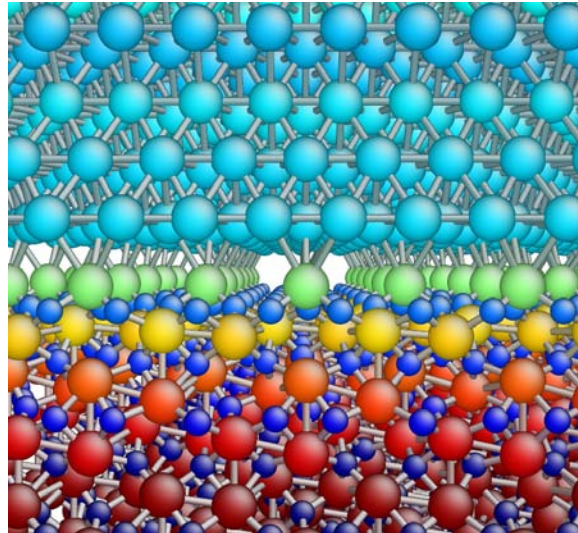


B.  $Al_1^O Al_2^F$

Figure 5-5. A second layer of Al atoms in the FCC metal film can be oriented over either of the two remaining sites. The surface in A is formed by aligning the first Al layer in the metal over the O sites,  $Al_1^O$  and the second Al layer over the H sites,  $Al_2^H$ . The surface in B has the second Al layer aligned over the F sites,  $Al_2^F$ .



A.  $Al_1^H Al_2^O$



B.  $Al_1^O Al_2^F$

Figure 5-6. The interfaces with the highest (A) and lowest (B)  $W_{sep}$  as predicted by the COMB potential. Color corresponds to charge ranging from red=1.5 and blue=-1.5 formal charge units.

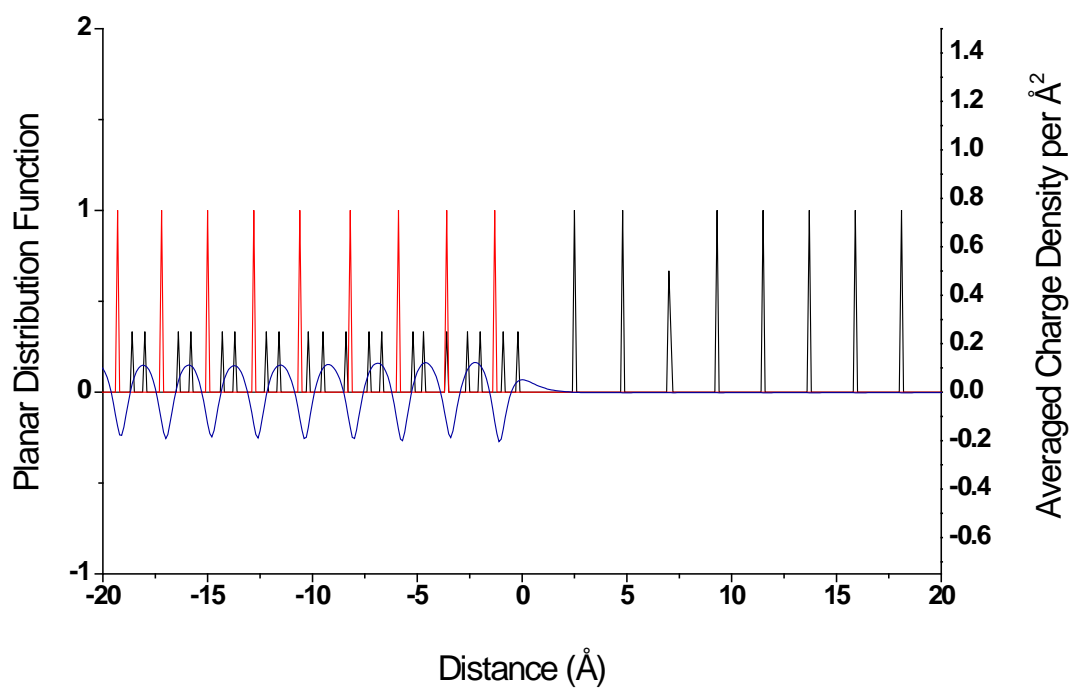


Figure 5-7. The charge density (blue line) and separation distance per plane of atoms across the  $Al_1^H Al_2^O$  interface at 0 K. The red line represents the distance between planes of O atoms and black corresponds to Al.

Table 5-1. Atomic and electrostatic potential parameters

|  | Al        | O         |
|--|-----------|-----------|
| $\chi$ (eV·q <sup>-1</sup> )                   | 4.478988  | 4.700782  |
| $J$ (eV·q <sup>-2</sup> )                      | 3.246069  | 5.064537  |
| $K$ (eV·q <sup>-3</sup> )                      | 0.000000  | 2.756183  |
| $L$ (eV·q <sup>-4</sup> )                      | 0.000000  | 0.992188  |
| $\xi$ (Å <sup>-1</sup> )                       | 0.618852  | 3.012029  |
| $Z$ (q)  | 0.146428  | 0.030819  |
| $P$ (Å <sup>3</sup> )                          | 0.335000  | 0.323757  |
| $P_1^J$ (eV·q <sup>-3</sup> ·r <sup>-5</sup> ) | 0.612118  | -0.054039 |
| $P_1^J$ (eV·q <sup>-4</sup> ·r <sup>-5</sup> ) | 0.006107  | 1.136518  |
| $D_u$ (Å)                                      | -0.011615 | -1.628749 |
| $D_l$ (Å)                                      | 0.679563  | 0.244020  |
| $Q_u$ (q)                                      | 3.000000  | 6.000000  |
| $Q_l$ (q)                                      | -5.000000 | -2.000000 |
| CN*  | 6.000000  | 4.000000  |
| $P^{VdW}$                                      | 0.000000  | 0.000000  |
| $\gamma^{Coord}$                               | 0.500000  | 0.250000  |
| $E^{Coord}$                                    | 0.000000  | 4.887383  |

Table 5-2. Interaction dependent potential parameters

|                              | Al-Al    | O-O       | Al-O      | O-Al      |
|------------------------------|----------|-----------|-----------|-----------|
| A (eV)                       | 379.6596 | 3523.359  | 1023.282  | 1023.282  |
| B (eV)                       | 70.79098 | 204.6259  | 132.1803  | 132.1803  |
| $\alpha$ (Å <sup>-1</sup> )  | 2.197639 | 5.516839  | 1.399757  | 1.399757  |
| $\lambda$ (Å <sup>-1</sup> ) | 1.223328 | 2.527568  | 3.452255  | 3.452255  |
| $\beta$                      | 0.168176 | 2.000000  | 0.168176  | 2.000000  |
| $\eta$                       | 1.000000 | 1.000000  | 1.000000  | 1.000000  |
| M                            | 1.000000 | 1.000000  | 1.000000  | 1.000000  |
| C (rad.)                     | 0.000705 | 43.56000  | 1.832422  | 0.000747  |
| D (rad.)                     | 0.305736 | 1.000000  | 1.000000  | 1.000000  |
| H (rad.)                     | 0.047803 | -0.220000 | -0.131031 | -0.415250 |
| $n_B$                        | 10.00000 | 10.00000  | 10.00000  | 10.00000  |
| $R_s$ (Å)                    | 3.000000 | 3.000000  | 2.200000  | 2.200000  |
| $S_s$ (Å)                    | 3.400000 | 3.400000  | 2.600000  | 2.600000  |

Table 5-3. Coefficients for Legendre polynomials

|                 | Al-Al-Al | Al-O-Al   | O-Al-O    |
|-----------------|----------|-----------|-----------|
| $K_{LP}^1$ (eV) | 0.015581 | -0.165976 | -0.477644 |
| $K_{LP}^2$ (eV) | 0.039822 | 0.279429  | 0.966470  |
| $K_{LP}^3$ (eV) | 0.072865 | 0.247754  | 0.050423  |

Table 5-4. Properties of metallic aluminum

|   | Experiment or<br>DFT                    | <sup>f</sup> ES+ | <sup>g</sup> ReaxFF | COMB |
|---|---|------------------|---------------------|------|
| <u>FCC Properties</u>                             |   |                  |                     |      |
| $a$ (Å)   | 4.05 <sup>a</sup>                       | 4.05             | 4.01                | 4.05 |
| $E_o$ (eV/atom)                                   | 3.36 <sup>b</sup>                       | 3.39             | 3.36                | 3.36 |
| $B$ (GPa)   | 79 <sup>c</sup>                         | 83               | 79                  | 79   |
| $C_{11}$ (GPa)                                    | 114 <sup>c</sup>                        | 94               | 119                 | 114  |
| $C_{12}$ (GPa)                                    | 62 <sup>c</sup>                         | 77               | 57                  | 62   |
| $C_{44}$ (GPa)                                    | 32 <sup>c</sup>                         | 34               | 50                  | 36   |
| <u>Phase Transitions (eV/atom)</u>                |   |                  |                     |      |
| $\Delta E_o$ HCP                                  | 0.03 <sup>d</sup>                       |                  | 0.00                | 0.03 |
| $\Delta E_o$ BCC                                  | 0.11 <sup>d</sup>                       |                  | 0.05                | 0.12 |
| $\Delta E_o$ Diamond                              | 0.67 <sup>d</sup>                       |                  | 0.70                | 1.38 |
| $\Delta E_o$ Cubic                                | 0.33 <sup>d</sup>                       |                  | 0.37                | 0.61 |
| <u><math>\Delta H_f</math> Point Defects (eV)</u> |   |                  |                     |      |
| $V_{Al}$  | 0.68 <sup>d</sup>                       |                  | 0.85                | 1.52 |
| $I_{oct}$   | 2.79 <sup>d</sup>                       |                  |                     | 3.33 |
| 100 dumbell*                                      |   |                  |                     | 2.50 |
| 110 dumbell*                                      |   |                  |                     | 7.69 |
| 111 dumbell*                                      |   |                  |                     | 8.58 |
| <u>Planar Defects (mJ·m<sup>-2</sup>)</u>         |   |                  |                     |      |
| $\gamma$ (100)                                    | 980 <sup>e</sup> , 943 <sup>g</sup>     |                  | 576                 | 948  |
| $\gamma$ (110)                                    | 980 <sup>e</sup> , 1000 <sup>g</sup>    |                  | 576                 | 1100 |
| $\gamma$ (111)                                    | 980 <sup>e</sup> , 870 <sup>g</sup>     |                  | 576                 | 805  |
| $\gamma_{SF}$                                     | 166 <sup>e</sup> , 120-144 <sup>h</sup> |                  |                     | 135  |
| $\gamma_{USF}$                                    | 168 <sup>d</sup>                        |                  |                     | 858  |
| $\gamma_{Twin}$                                   | 75 <sup>e</sup>                         |                  |                     | 68   |

\* Indicates predicted values not included in the training set.

<sup>a</sup>Reference 157

<sup>b</sup>Reference 143

<sup>c</sup>Reference 172

<sup>d</sup>Reference 140

<sup>e</sup>Reference 196

<sup>f</sup>Reference 22

<sup>g</sup>Reference 40

<sup>h</sup>Reference 197, 198

Table 5-5. Ionization potentials and electron affinities (in eV) for Al and O

| Al                        | <i>Ab Initio</i> <sup>a</sup> | COMB  |
|---------------------------|-------------------------------|-------|
| <i>EA</i>                 | 1.23                          | 1.08  |
| 1 <sup>st</sup> <i>IP</i> | 7.73                          | 7.72  |
| 2 <sup>nd</sup> <i>IP</i> | 12.6                          | 14.2  |
| 3 <sup>rd</sup> <i>IP</i> | 36.6                          | 20.7  |
| <b>O</b>                  |                               |       |
| 1 <sup>st</sup> <i>IP</i> | 13.1                          | 13.1  |
| 1 <sup>st</sup> <i>EA</i> | 1.40                          | 1.40  |
| 2 <sup>nd</sup> <i>EA</i> | -6.08                         | -6.08 |

<sup>a</sup>Calculated with CCSD(t)/cc-pVTZ

Table 5-6. Properties of  $\alpha$ -Al<sub>2</sub>O<sub>3</sub>

|  | Experiment<br>1 <sup>st</sup> Principles | <sup>f</sup> ES+ | <sup>9</sup> ReaxFF | COMB  |
|--|--|------------------|---------------------|-------|
| <i>a</i> (Å)   | 4.76 <sup>a</sup>                        | 4.76             | 4.81                | 4.75  |
| <i>c</i> (Å)   | 13.0 <sup>b</sup>                        | 13.0             | 13.1                | 12.9  |
| <i>E<sub>coh</sub></i> (eV/Al <sub>2</sub> O <sub>3</sub> )                          | 31.8 <sup>b</sup>                        | 31.8             | 38                  | 31.9  |
| <i>Bulk Mod.</i> (GPa)   | 254 <sup>c</sup>                         | 250              | 248                 | 256   |
| <i>C<sub>11</sub></i> (GPa)  | 497 <sup>c</sup>                         | 537              |                     | 546   |
| <i>C<sub>12</sub></i> (GPa)  | 164 <sup>c</sup>                         | 180              |                     | 175   |
| <i>C<sub>13</sub></i> (GPa)  | 111 <sup>c</sup>                         | 106              |                     | 88.2  |
| <i>C<sub>14</sub></i> (GPa)  | -24 <sup>c</sup>                         | -30              |                     | -27.8 |
| <i>C<sub>33</sub></i> (GPa)  | 498 <sup>c</sup>                         | 509              |                     | 507   |
| <i>C<sub>44</sub></i> (GPa)  | 147 <sup>c</sup>                         | 130              |                     | 195   |
| <i>C<sub>66</sub></i> (GPa)  | 168 <sup>c</sup>                         | 179              |                     | 201   |
| Al Charge  |  | 2.86             |                     | 0.95  |
| <u>Defects in <math>\alpha</math>-Al<sub>2</sub>O<sub>3</sub> (eV)</u>               |  |                  |                     |       |
| <i>V<sub>Al</sub></i>  | 8.44 <sup>d</sup>                        |                  |                     | 4.46  |
| <i>V<sub>O</sub></i>   | 6.09 <sup>d</sup>                        |                  |                     | 0.90  |
| <i>O<sub>i</sub></i>   | 8.84 <sup>d</sup>                        |                  |                     | 3.61  |
| <i>Al<sub>i</sub></i>  | 16.8 <sup>d</sup>                        |                  |                     | 10.8  |
| $\gamma_{(0001)}$ (J m <sup>-2</sup> )   | 1.59/2.12 <sup>e</sup>                   | 2.67             | 1.0                 | 1.82  |
| <u><math>\Delta E</math> for Meta-Stable Oxides (eV/Al<sub>2</sub>O<sub>3</sub>)</u> |  |                  |                     |       |
| Bixbyite   | 0.97 <sup>a</sup>                        |                  | 0.66                | 0.74  |
| $\theta$   | 0.38 <sup>a</sup>                        |                  | 0.19                | 1.84  |

<sup>a</sup>Reference 199

<sup>b</sup>Reference 143

<sup>c</sup>Reference 200

<sup>d</sup>Reference 194

<sup>e</sup>Reference 184 (GGA/LDA)

<sup>f</sup>Reference 22

<sup>9</sup>Reference 40

Table 5-7. Interfacial separation distance,  $D_o$  (in Å) and  $W_{sep}$  (in J·m<sup>-2</sup>) for the relaxed single Al terminated Al(111)/α-Al<sub>2</sub>O<sub>3</sub>(0001) interfaces.

|                                       | $Al_1^F Al_2^O$ | $Al_1^F Al_2^H$ | $Al_1^H Al_2^F$ | $Al_1^H Al_2^O$ | $Al_1^O Al_2^F$ | $Al_1^O Al_2^H$ |
|---------------------------------------|-----------------|-----------------|-----------------|-----------------|-----------------|-----------------|
| <sup>a</sup> $W_{sep}$ <i>Expt</i>    | 1.13            |                 |                 |                 |                 |                 |
| <sup>b</sup> $W_{sep}$ <i>DFT*</i>    | 1.36            | 1.36            | 0.69            | 0.69            | 1.18            | 1.18            |
| <sup>c</sup> $W_{sep}$ <i>ReaxFF*</i> | 1.74            | 1.74            | 1.31            | 1.31            |                 |                 |
| $W_{sep}$ <i>COMB</i>                 | 1.31            | 1.31            | 1.31            | 1.39            | 1.29            | 1.38            |
| <sup>b</sup> $D_o$ <i>DFT*</i>        | 0.70            | 0.70            | 2.57            | 2.57            | 1.62            | 1.62            |
| $D_o$ <i>COMB</i>                     | 2.55            | 3.01            | 2.55            | 2.54            | 2.56            | 2.54            |

\*Values do not distinguish between Al<sub>2</sub> orientations

<sup>a</sup>Reference 86

<sup>b</sup>Reference 184

<sup>c</sup>Reference 40

## CHAPTER 6 CURRENT CAPABILITIES AND FUTURE POSSIBILITIES OF CHARGE OPTIMIZED MANY BODY POTENTIALS

Development of empirical potentials is an active area of research in computational materials science and engineering. This is particularly true since device design has reached the nano-scale where fully atomistic simulations of actual life-sized systems are feasible. Often such applications involve the interface between two different functional materials. As the size of a multifunctional device is reduced, the material contained within the surface and interfacial regions constitutes an increased portion of the total device and, commensurately, performance is increasingly influenced by surface and interfacial effects.<sup>173</sup> Computational simulations hold promise for providing insight into complex interfacial and surface processes and their impact on device performance. Computational applications such as these rely heavily upon classical analytical potentials. The availability of suitable potential energy functions is currently the main limitation to simulations of realistically complex systems

Chapter 3 of this work presents a comparison between the empirical REBO potential and first principle methods. The primary conclusion to draw, in regards to methodology, is all levels of theory have significant strengths and weakness that must be balanced and accounted for. In that work, the higher quality methods are limited to small systems and low quality statistics, yet are more reliable in their predictions. DFT results suggest that CF<sub>3</sub> and CF<sub>3</sub><sup>+</sup> react differently at deposition energies of 50 eV. At that energy, CF<sub>3</sub> adds to the surface and forms bonds while CF<sub>3</sub><sup>+</sup> fragments and removes more H from the surface. The REBO potential does not include electrostatic interactions and so can not resolve the difference in reactivity between these species.

An assumption is that at high deposition energies, both species will react similarly. This assumption is shown to be invalid at 50 eV.

DFT-MD also reveals a single step addition of CF<sub>0-2</sub> to the diamond surface when coupled with the formation and evolution of HF. The REBO potential failed to predict this key reaction and several other HF forming reactions. The discrepancy is attributable to the short interaction distance between H and F in REBO. The bond lengths in key transition states are found to be at the extreme limits of interaction distance in REBO.

The efficiency of REBO allows for a sampling size that is several orders of magnitude larger than DFT methods. The improved statistics with the REBO model have the potential to significantly enhance the quality of the results. Unfortunately, through comparison to higher level methods, the limitations of the model and their implications in the results are revealed. More importantly, weaknesses in the model can be addressed in the next generation of the methodology, which for the REBO potential, involves the addition of variable charge electrostatics and the increased interaction distances.

The extension of COMB to hydrocarbons is currently an active project. As the COMB model is extended to systems with challenging chemistry and an abundance of structures, the transferability of the method will be challenged. The current version of the model is designed to give the best chance of success in expanding to these systems. As shown in Chapter 2, the potential is derived from the same DFT functionals as the current hydrocarbon potentials.<sup>16, 24, 25</sup> Brenner attributes the transferability of REBO to this basis in DFT.<sup>52</sup> Furthermore, additional functions that, so

far, have been required to fit new systems, are chosen to correct interactions that are lost in the approximations of the initial derivation.

This project initially began with three potentials, Yasukawa's potential<sup>17</sup>, Streitz and Mintmire's ES+ model,<sup>22</sup> and a modified embedded atom method (MEAM).<sup>201, 202</sup> The idea at the time was to compare these three potentials for application to multi-phase systems. The Yasukawa potential is essentially a Tersoff potential coupled with a variable charge scheme. The short range interactions vary with charge. However, in that potential, the electrostatic functions are based on a point charge model with interactions cutoff just past the second neighbor shell, which causes several instabilities in application. The ES+ model has electrostatic interactions are determined as functionals of charge density with truly long interaction distances. Unfortunately, the electrostatics are coupled to and Finnis-Sinclair short range potential which cannot describe covalent systems. MEAM is an improved second moment model that includes angular terms to model covalent systems but lacks electrostatic interactions.<sup>201</sup> Of the three approaches, the Yasukawa potential, while flawed, performed the most reliably.

With the hindsight gained from the derivation in Chapter 2, it is clear that the Yasukawa formalism succeeds because it adds back some of the interactions that are approximated away in ES+ and MEAM. ES+ is based on the rigid atom approximation and, as a consequence, is unreliable in complex systems. Yasukawa addresses the short range effects that are neglected with the rigid ion approximation. In the COMB formalism, the long range electrostatic interactions that are missing in Yasukawa's potential<sup>17</sup> are added back along with several long range interactions that are lost with

a rigid atom approximation. After much trial in error, it seems this current course of development is the most promising.

The adaptability of the COMB potential is demonstrated by fitting the potential for two metal-metal oxide systems. First, demonstrated in Chapter 4 is the development of a potential for the Cu/CuO system, which involves multiple oxidation states of Cu. The initial oxide phase formed under oxygen lean conditions is the meta-stable cubic phase of Cu<sub>2</sub>O. As oxidation proceeds and at higher temperatures, monoclinic CuO forms. The potential is parameterized to model the initial stages of oxidation through the growth of Cu<sub>2</sub>O islands. The results of the fit suggest the potential is well suited for this task. The bulk and mechanical properties are accurately reproduced compared with experimental and first principles based data. Surface energies and defect formation enthalpies are also consistent with first principles calculations. The potential reproduces the relative phase order and formation enthalpies for the low energy oxide phases. The potential captures the dissociation energy of molecular oxygen and its anions, which, in turn, leads to a prediction of adsorption energy consistent with DFT. The potential also predicts an adsorption induced missing row reconstruction as the stable oxidized surface at standard temperature, consistent with experiment. The ability of this potential formalism to be adapted to both metallic phases and the oxides both as solid phases and single molecules and with reconstructed surfaces demonstrates a remarkable flexibility in the functional form.

In Chapter 5, the potential is adapted to model Al/□Al<sub>2</sub>O<sub>3</sub> interfaces. The low energy phase of the oxide, □Al<sub>2</sub>O<sub>3</sub>, forms in the hexagonal corundum crystal structure, which is stabilized by subtle polarization effects in the electron density distribution. Most

classical potentials fail to predict the correct ground state crystal structure and instead predict a cubic Bixbyite structure. The COMB model is able to correctly predict corundum as the ground state structure. This is a distinction that is not easily made even with first principles methods. Similar to Cu/CuO system, the potential also reproduces the bulk and mechanical properties of both metallic and oxide phases as well as the surface energies and defect formation enthalpies in both phases. It predicts atomically sharp interfaces between Al(111) surface and crystalline  $\alpha$ -Al<sub>2</sub>O<sub>3</sub>(0001), which is consistent with the results of DFT calculations. However, the potential does not reproduce interfacial reconstructions as predicted by DFT. Interfacial works of separation are comparable to DFT calculated values. However, trends in relative energies of different variations of the interface are not captured, indicating the potential is best used for bulk phase calculations and perhaps studies of oxidation in this material.

In other efforts the potential has been extended to model all the low energy polymorphic phases of SiO<sub>2</sub><sup>18</sup> including amorphous phases and Hf-HfO<sub>2</sub><sup>184</sup>. These systems also pose unique challenges that have not been addressed with less flexible models. For example, most potentials for HfO<sub>2</sub> fail to predict the correct phase order.<sup>184</sup> The flexibility and transferability of the COMB formalism as demonstrated here and in these other works is quite encouraging.

## 6.1 The COMB Code

The COMB project was initiated to address the growing need for new efficient computational methods. The implied tasks in that objective are to first develop a potential formalism with sufficient flexibility to model many materials of interest and secondly to concurrently develop the tools and procedures to efficiently fit the potential

to new materials. The two tasks are somewhat interrelated where now the COMB project consists of both a potential form and a suite of FORTRAN90 codes.

In addition to the flexibility of the current model, the code itself is designed with the machinery in place to efficiently add additional interaction as the needs arise. For example, a possible improvement for  $\text{Al}_2\text{O}_3$  would be to add the quadrupole moments. The code to add higher order polarization modes along the lines of the compressible ion models<sup>26</sup> has already been added with the point dipole model. There are some technical issues to address, such as how polarizability varies with charge. However, the administrative coding of how the interactions are processed and information passed is complete. For entirely new interactions, such as four bodied energy contributions that arise in hydrocarbon models, the architecture to pass information, even in parallel, is in place. The loop structure would have to be created for the four bodied interactions. However, the code is modularized and fully declared with no implicit variables to assist modification.

The current code exists as two versions: one parallel and one serial. The parallel version breaks the calculation up into equal spatial regions. For example, a 2x2 spatial decomposition breaks the system up in two dimensions into a 2x2 grid. Each section of the grid is assigned a processor that only processes that part of the system. A 2x2 system should, therefore, process nearly four times faster than the same system on one processor. The parallel code is designed for running large systems with the focus on computational efficiency. The code scales linearly with system size depending on the number of processor used.

A serial code processes the calculation on one processor, which allows for smaller systems that are used mainly for potential development. Fitting a potential requires many sequential calculations. A well designed serial code efficiently processes each calculation as quickly as possible, whereas, in a parallel code; emphasis is placed on processing many calculations simultaneously. The two code formats together are able to handle both development and production.

## 6.2 The Fitting Problem

The models developed here are fit to a mix of measured and calculated values. The preference is to fit to empirical data augmented with first principles calculations when empirical values are not obtainable. This is a philosophical choice. Several potentials are fit entirely to calculated data sets.<sup>16, 202</sup> However, for the systems modeled here, the first principles values are not always accurate or correct.<sup>144</sup> There are arguments for either approach.<sup>140</sup> A model fit to experimental data is fit to a more accurate data set than what is achievable with first principles calculations. A model fit with precision to the more accurate data set will reproduce those values more accurately. However, experimental data sets are small and transferability beyond the data set is never ensured, even with a precise fit. In contrast, the only limit on the size of a training data set based on first principles calculations is computer time. Given enough resources, a training data set that maps the DFT potential energy surface could, in principle, be generated. Any model fit to such an extensive data set could be as transferable as DFT, yet only as accurate as DFT. With the current state of the art, the best approach is to fit to a mix of experimental and calculated data points. Brenner concluded in his review of bond order potentials that while it is quite possible that no purely empirical potential will ever be truly transferable, no potential derived entirely

from first principles will be truly accurate.<sup>52</sup> Brenner's point is appreciated in this work, considering systems such as CuO, where being as accurate as DFT is not very accurate.

Perhaps, as important as developing the potential is designing the fitting process. A large part of the success of the ReaxFF models is that it has been extended to so many systems. Within the COMB suite are series of codes designed to do multi-dimensional minimizations. The algorithms are standards from the numerical recipes.<sup>203</sup> The fitting codes work with the actual serial version of the COMB code. They call the same energy and force subroutines that are used in the production codes and use the same variable names and data types so that parameters can be quickly tested and put to use.

Each phase of a multiphase system can be fit separately. For example all metal-metal interactions can be fit to bulk metallic phases. Self energies parameters are fit to atomic values. The different interaction can also be optimized separately; charge dependent and charge independent parameters can be optimized to a degree separately. Versions of the fitting codes have been optimized to specifically fit these separate phases. Fitting a potential is a challenging task. The COMB suite has evolved to where the basic tools need to run simulations, analyze results and fit new systems are in place.

### **6.3 Future Applications**

In addition to hydrocarbon systems, the COMB model is currently being extended to Zn and ZnO, U and UO<sub>2</sub>, Ti and TiO<sub>4</sub>. This gives an idea of the diverse range of materials and applications to which the model can be applied. The next phase of development will be to extensively run applications and comparative studies. This is an

area with fairly sparse data, as the model has just recently been finalized. The best test is to get the code into production and get feedback on its strengths and failings. As it stands, the COMB model and suite has the potential to greatly expand computation to systems that cannot be studied by any other means, which in turn, could tremendously enhance the choice and selection of materials for the next generation of multi-functional devices.

## LIST OF REFERENCES

- 1 P. Mutti, G. Ghislotti, S. Bertoni, et al., Appl. Phys. Lett. **66**, 851 (1995).
- 2 T. Shimizu-Iwayama, S. Nakao, and K. Saitoh, Appl. Phys. Lett. **65**, 1814 (1994).
- 3 Q. Zhang, S. C. Bayliss, and D. A. Hutt, Appl. Phys. Lett. **66**, 1977 (1995).
- 4 L. Hanley, Y. Choi, E. R. Fuoco, *et al.*, Nucl. Inst. Meth. Phys. Res. B **203**, 116 (2003).
- 5 K. Kimura and S. Iwasaki, J. Appl. Phys. **83**, 1345 (1998).
- 6 P. F. Trwoga, A. J. Kenyon, and C. W. Pitt, J. Appl. Phys. **83**, 3789 (1998).
- 7 K. S. Seol, A. Ieki, Y. Ohki, et al., J. Appl. Phys. **79**, 412 (1996).
- 8 M. L. Brongersma, A. Polman, K. S. Min, *et al.*, Appl. Phys. Lett. **72**, 2577 (1998).
- 9 K. S. Zhuravlev, A. M. Gilinsky, and A. Y. Kobitsky, Appl. Phys. Lett. **73**, 2962 (1998).
- 10 R. A. Buckingham, Proc. R. Soc. Lond. A. **168**, 264 (1938).
- 11 J. Tersoff, Phys. Rev. B **37**, 6991 (1988).
- 12 J. Tersoff, Phys. Rev. B **38**, 9902 (1988).
- 13 B. J. Garrison, E. J. Dawnkaski, D. Srivastava, *et al.*, Science **255**, 835 (1992).
- 14 A. K. Rappe and W. A. Goddard, J. Phys. Chem. **95**, 3358 (1991).
- 15 T. Iwasaki and H. Miura, J. Mater. Res. **16**, 1789 (2001).
- 16 A. C. T. van Duin, S. Dasgupta, F. Lorant, *et al.*, J. Phys. Chem. A **105**, 9396 (2001).
- 17 A. Yasukawa, JSME Intl. J. A **39**, 313 (1996).
- 18 M. B. J. Wijesundara, Y. Ji, B. Ni, *et al.*, J. Appl. Phys. **88**, 5004 (2000).
- 19 Q. Zhang, T. Cagin, A. van Duin, *et al.*, Phys. Rev. B **69** (2004).
- 20 X. W. Zhou and F. P. Doty, Phys. Rev. B **78** (2008).
- 21 M. W. Finnis and J. E. Sinclair, Philo. Mag. A **50**, 45 (1984).

- 22 F. H. Streitz and J. W. Mintmire, Phys. Rev. B **50**, 11996 (1994).
- 23 G. C. Abell, Phys. Rev. B **31**, 6184 (1985).
- 24 D. W. Brenner, Phys. Rev. B **42**, 9458 (1990).
- 25 D. W. Brenner, O. A. Shenderova, J. A. Harrison, *et al.*, J. Phys.: Condens. Matter **14**, 783 (2002).
- 26 T. R. Shan, B. D. Devine, T. W. Kemper, *et al.*, Phys. Rev. B **81** (2010).
- 27 W. Kohn and L. J. Sham, Phys. Rev. **140**, A1133–A1138 (1965).
- 28 P. Hohenberg and W. Kohn, Phys. Rev. B **136**, B864 (1964).
- 29 A. J. Cohen, P. Mori-Sanchez, and W. T. Yang, Science **321**, 792 (2008).
- 30 R. G. Parr and W. Yang, *Density-Functional Theory of Atoms and Molecules* (Oxford University Press, New York, 1989).
- 31 R. H. Milne and A. Howie, Philo. Mag. A **49**, 665 (1984).
- 32 R. Guan, H. Hashimoto, and T. Yoshida, Acta Crystal. B **40**, 109 (1984).
- 33 L. O. Brockway and I. M. Adler, J. Electrochem. Soc. **119**, 899 (1972).
- 34 A. Ronnquist and H. Fischmeister, J. Inst. of Metals **89**, 65 (1960).
- 35 R. Drautz, D. A. Murdick, D. Nguyen-Manh, *et al.*, Phys. Rev. B **72** (2005).
- 36 D. G. Pettifor, M. W. Finnis, D. Nguyen-Manh, *et al.*, Mater. Sci. Eng. A **365**, 2 (2004).
- 37 G. W. Zhou and J. C. Yang, Mater. at High Temperatures **20**, 247 (2003).
- 38 M. Schwartzman, A. Mathur, Y. Kang, *et al.*, J. Vac. Sci. Tech. B **26**, 2394 (2008).
- 39 B. Devine, I. Jang, T. Kemper, *et al.*, J. Phys. Chem. C **114**, 12535 (2010).
- 40 Q. Zhang, T. Cagin, A. van Duin, *et al.*, Phys. Rev. B **69** (2004).
- 41 M. Wilson, M. Exner, Y. M. Huang, *et al.*, Phys. Rev. B **54**, 15683 (1996).
- 42 D. G. Pettifor, Phys. Rev. Lett. **63**, 2480 (1989).
- 43 Oleinik, II and D. G. Pettifor, Phys. Rev. B **59**, 8500 (1999).

- 44 D. Raymond, A. C. T. van Duin, M. Baudin, *et al.*, Surf. Sci. **602**, 1020 (2008).
- 45 D. A. Murdick, X. W. Zhou, H. N. G. Wadley, *et al.*, Phys. Rev. B **73** (2006).
- 46 B. A. Gillespie, X. W. Zhou, D. A. Murdick, *et al.*, Phys. Rev. B **75** (2007).
- 47 R. Drautz, X. W. Zhou, D. A. Murdick, *et al.*, Prog. Mater. Sci. **52**, 196 (2007).
- 48 S. Znam, D. Nguyen-Manh, D. G. Pettifor, *et al.*, Philo. Mag. **83**, 415 (2003).
- 49 S. Ryu, C. R. Weinberger, M. I. Baskes, *et al.*, Modelling and Simulation in Materials Science and Engineering **17** (2009).
- 50 J. Uddin, M. I. Baskes, S. G. Srinivasan, *et al.*, Phys. Rev. B **81** (2010).
- 51 T. Hammerschmidt, R. Drautz, and D. G. Pettifor, Intl. J. Mater. Res. **100**, 1479 (2009).
- 52 D. W. Brenner, Phys. Status Solidi B **217**, 23 (2000).
- 53 P. A. M. Dirac, Proc. R. Soc. Lond. A **117**, 610 (1928).
- 54 A. Szabo and N. Ostlund, *Modern Quantum Chemistry* (Macmillan, New York, 1982).
- 55 P. A. M. Dirac, Proc. R. Soc. Lond. A **112**, 661 (1926).
- 56 W. Heisenberg, Zeitschrift Fur Physik **40**, 501 (1926).
- 57 M. Born and R. Oppenheimer, Annalen Der Physik **84**, 0457 (1927).
- 58 R. C. Brown, C. J. Cramer, and J. T. Roberts, J. Phys. Chem. B **101**, 9574 (1997).
- 59 M. Born and K. Huang, *Dynamical Theory of Crystal Lattices* (Oxford University Press, Oxford, 1954).
- 60 Ditchfie.R, W. J. Hehre, and J. A. Pople, J. Chem. Phys. **54**, 724 (1971).
- 61 P. A. M. Dirac, Proc. R. Soc. Lond. A **111**, 405 (1926).
- 62 W. Pauli, Zeitschrift Fur Physik **31**, 765 (1925).
- 63 J. C. Slater, Phys. Rev. **35**, 0210 (1930).

- 64 P. A. M. Dirac, Proc. Camb. Philo. Soc **26**, 376 (1930).
- 65 D. R. Hartree, Proc. Camb. Philo. Soc **24**, 89 (1928).
- 66 V. Fock, Z. Phys. **61**, 126 (1930).
- 67 R. S. Mulliken, J. Chem. Phys. **23**, 2338 (1955).
- 68 R. S. Mulliken, J. Chem. Phys. **23**, 2343 (1955).
- 69 R. S. Mulliken, J. Chem. Phys. **23**, 1833 (1955).
- 70 R. S. Mulliken, J. Chem. Phys. **23**, 1841 (1955).
- 71 P. O. Lowdin, Adv. Quantum Chem. **5**, 185 (1970).
- 72 A. Freedman and C. D. Stinespring, Appl. Phys. Lett. **57**, 1194 (1990).
- 73 C. A. Coulson, Proc. R. Soc. Lond. A **169**, 413 (1939).
- 74 P. E. Blochl, Phys. Rev. B **50**, 17953 (1994).
- 75 E. Fermi, Atti Accad. Naz. Lincei, Cl. Sci. Fis., Mat. Nat., Rend. **6**, 602 (1927).
- 76 A. K. George, A. S. Harry, B. J. Berne, et al., J. Comp. Chem. **23**, 1515 (2002).
- 77 R. P. Feynman, Phys. Rev. **56**, 340 (1939).
- 78 W. Matthew, C. Foulkes, and R. Haydock, Phys. Rev. B **39**, 12520 (1989).
- 79 J. Harris, Phys. Rev. B **31**, 1770 (1985).
- 80 B. G. Dick and A. W. Overhauser, Phys. Rev. **112**, 90 (1958).
- 81 D. Wolf, P. Keblinski, S. R. Phillpot, et al., J. Chem. Phys. **110**, 8254 (1999).
- 82 S. W. Rick, S. J. Stuart, and B. J. Berne, J. Chem. Phys. **101**, 6141 (1994).
- 83 W. C. Swope, H. C. Andersen, P. H. Berens, *et al.*, J. Chem. Phys. **76**, 637 (1982).
- 84 F. Cyrot-Lackmann, J. Phys. Chem. Solids **29**, 1235 (1968).
- 85 D. W. Brenner, Phys. Rev. Lett. **63**, 1022 (1989).
- 86 I. Batyrev, A. Alavi, and M. W. Finnis, Faraday Discussions, 33 (1999).

- 87 L. A. Curtiss, K. Raghavachari, P. C. Redfern, *et al.*, Chem. Phys. Lett. **314**, 101 (1999).
- 88 G. D. Purvis and R. J. Bartlett, J. Chem. Phys. **76**, 1910 (1982).
- 89 M. Sternberg, P. Zapol, and L. A. Curtiss, Molec. Phys. **103**, 1017 (2005).
- 90 B. T. Thole, Chem. Phys. **59**, 341 (1981).
- 91 J. Applequist, J. R. Carl, and K. K. Fung, J. Am. Chem. Soc. **94**, 2952 (1972).
- 92 D. Vanbelle and S. J. Wodak, Comp. Phys. Comm. **91**, 253 (1995).
- 93 P. Geerlings, F. De Proft, and W. Langenaeker, Chem. Rev. **103**, 1793 (2003).
- 94 H. Toufar, K. Nulens, G. O. A. Janssens, *et al.*, J. Phys. Chem. **100**, 15383 (1996).
- 95 T. H. Dunning, J. Chem. Phys. **90**, 1007 (1989).
- 96 J. M. Soler, E. Artacho, J. D. Gale, *et al.*, J. Phys: Condens. Matter **14**, 2745 (2002).
- 97 E. Artacho, E. Anglada, O. Dieguez, *et al.*, J. Phys.: Condens. Matter **20**, 064208 (2008).
- 98 I. Jang and S. B. Sinnott, J. Phys. Chem. B **108**, 18993 (2004).
- 99 L. Hanley and S. B. Sinnott, Surf. Sci. **500**, 500 (2002).
- 100 S. A. Adelman and J. D. Doll, J. Chem. Phys. **64**, 2375 (1976).
- 101 R. Car and M. Parrinello, Phys. Rev. Lett. **55**, 2471 (1985).
- 102 W. G. Hoover, Phys. Rev. A **31**, 1695 (1985).
- 103 S. Nose, J. Chem. Phys. **81**, 511 (1984).
- 104 S. Nose, Molec. Phys. **52**, 255 (1984).
- 105 N. Troullier and J. L. Martins, Phys. Rev. B **43**, 1993 (1991).
- 106 J. A. Pople, M. Head-Gordon, and K. Raghavachari, J. Chem. Phys. **87**, 5968 (1987).

- 107 J. P. Perdew, K. Burke, and M. Ernzerhof, Phys. Rev. Lett. **77**, 3865 (1996).
- 108 A. G. Baboul, L. A. Curtiss, P. C. Redfern, *et al.*, J. Chem. Phys. **110**, 7650 (1999).
- 109 G. W. T. M. J. Frisch, H. B. Schlegel, G. E. Scuseria, *et al.*, (Gaussian, Inc., Wallingford CT., 2004).
- 110 A. D. Becke, J. Chem. Phys. **98**, 5648 (1993).
- 111 Y. Zhao and D. G. Truhlar, J. Phys. Chem. A **112**, 1095 (2008).
- 112 A. D. McLean and G. S. Chandler, J. Chem. Phys. **72**, 5639 (1980).
- 113 A. D. Boese and J. M. L. Martin, J. Chem. Phys. **121**, 3405 (2004).
- 114 E. I. Izgorodina, D. R. B. Brittain, J. L. Hodgson, *et al.*, J. Phys. Chem. A **111**, 10754 (2007).
- 115 H. L. Schmider and A. D. Becke, J. Chem. Phys. **108**, 9624 (1998).
- 116 K. E. Riley, B. T. Holt, and K. M. Merz, J. Chem. Theory Comp. **3**, 407 (2007).
- 117 D. G. Goodwin, Appl. Phys. Lett. **59**, 277 (1991).
- 118 S. J. Harris, Appl. Phys. Lett. **56**, 2298 (1990).
- 119 M. Page and D. W. Brenner, J. Am. Chem. Soc. **113**, 3270 (1991).
- 120 D. G. Goodwin, J. Appl. Phys. **74**, 6895 (1993).
- 121 S. F. Boys and F. Bernardi, Molec. Phys. **19**, 553 (1970).
- 122 L. Pastewka, P. Pou, R. Perez, *et al.*, Phys. Rev. B **78** (2008).
- 123 M. Mrovec, M. Moseler, C. Elsasser, *et al.*, Prog. Mater. Sci. **52**, 230 (2007).
- 124 F. W. Young Jr, J. V. Cathcart, and A. T. Gwathmey, Acta Metal. **4**, 145 (1956).
- 125 K. Heinemann, D. B. Rao, and D. L. Douglass, Oxidation of Metals **9**, 379 (1975).
- 126 G. W. Zhou and J. C. Yang, Surf. Sci. **531**, 359 (2003).
- 127 N. Cabrera and N. F. Mott, Reports on Progress in Physics **12**, 163 (1948).
- 128 R. H. Milne and A. Howie, Philo. Mag. A **49**, 665 (1984).

- 129 K. Tanaka, T. Inomata, and M. Kogoma, *Thin Solid Films* **386**, 217 (2001).
- 130 L. Sun and J. C. Yang, *J. Mater. Res.* **20**, 1910 (2005).
- 131 R. H. Milne, *Surf. Sci.* **232**, 17 (1990).
- 132 G. Zhou, *J. Appl. Phys.* **105**, 104302 (2009).
- 133 K. Chenoweth, A. C. T. van Duin, P. Persson, *et al.*, *J. Phys. Chem. C* **112**, 14645 (2008).
- 134 R. W. G. Wyckoff, *Crystal Structures* (Interscience Publishers, New York, 1963).
- 135 N. E. Brese, M. Okeeffe, B. L. Ramakrishna, *et al.*, *J. Solid State Chem.* **89**, 184 (1990).
- 136 K. Takahashi, A. Itoh, T. Nakamura, *et al.*, *Thin Solid Films* **374**, 303 (2000).
- 137 E. Ruiz, S. Alvarez, P. Alemany, *et al.*, *Phys. Rev. B* **56**, 7189 (1997).
- 138 G. Kresse and J. Hafner, *Phys. Rev. B* **47**, 558 (1993).
- 139 J. H. Rose, J. R. Smith, F. Guinea, *et al.*, *Phys. Rev. B* **29**, 2963 (1984).
- 140 Y. Mishin, D. Farkas, M. J. Mehl, *et al.*, *Phys. Rev. B* **59**, 3393 (1999).
- 141 A. Soon, X. Y. Cui, B. Delley, *et al.*, *Phys. Rev. B* **79** (2009).
- 142 H. Raebiger, S. Lany, and A. Zunger, *Phys. Rev. B* **76** (2007).
- 143 D. R. Lide, *CRC Handbook of Chemistry and Physics* (CRC Press, Boca Raton, FL, 2005).
- 144 D. O. Scanlon, B. J. Morgan, and G. W. Watson, *J. Chem. Phys.* **131** (2009).
- 145 M. Sprik, *J. Phys. Chem.* **95**, 2283 (1991).
- 146 M. Nolan, *Thin Solid Films* **516**, 8130 (2008).
- 147 A. Soon, M. Todorova, B. Delley, *et al.*, *Phys. Rev. B* **75** (2007).
- 148 S. M. Woodley, P. D. Battle, C. R. A. Catlow, *et al.*, *J. Phys. Chem. B* **105**, 6824 (2001).

- 149 K. J. Blobaum, D. Van Heerden, A. J. Wagner, *et al.*, J. Mater. Res. **18**, 1535 (2003).
- 150 F. Besenbacher and J. K. Norskov, Prog. Surf. Sci. **44**, 5 (1993).
- 151 E. A. Colbourn and J. E. Inglesfield, Phys. Rev. Lett. **66**, 2006 (1991).
- 152 T. Fujita, Y. Okawa, Y. Matsumoto, *et al.*, Phys. Rev. B **54**, 2167 (1996).
- 153 H. Iddir, D. D. Fong, P. Zapol, *et al.*, Phys. Rev. B **76** (2007).
- 154 K. W. Jacobsen and J. K. Norskov, Phys. Rev. Lett. **65**, 1788 (1990).
- 155 F. Jensen, F. Besenbacher, E. Laegsgaard, *et al.*, Phys. Rev. B **42**, 9206 (1990).
- 156 T. Kangas and K. Laasonen, Surf. Sci. **602**, 3239 (2008).
- 157 M. Kittel, M. Polcik, R. Terborg, *et al.*, Surf. Sci. **470**, 311 (2001).
- 158 K. Lahtonen, M. Hirsimäki, M. Lampimäki, *et al.*, J. Chem. Phys. **129**, 124703 (2008).
- 159 T. Lederer, D. Arvanitis, G. Comelli, *et al.*, Phys. Rev. B **48**, 15390 (1993).
- 160 G. H. Liu and R. G. Parr, J. Am. Chem. Soc. **117**, 3179 (1995).
- 161 I. Merrick, J. E. Inglesfield, and H. Ishida, Surf. Sci. **551**, 158 (2004).
- 162 M. Ahonen, M. Hirsimäki, A. Puisto, *et al.*, Chem. Phys. Lett. **456**, 211 (2008).
- 163 I. K. Robinson, E. Vlieg, and S. Ferrer, Phys. Rev. B **42**, 6954 (1990).
- 164 M. Sotto, Surf. Sci. **260**, 235 (1992).
- 165 S. Stolbov, A. Kara, and T. S. Rahman, Phys. Rev. B **66** (2002).
- 166 S. Stolbov and T. S. Rahman, Phys. Rev. Lett. **89** (2002).
- 167 M. Wuttig, R. Franchy, and H. Ibach, Surf. Sci. **224**, L979 (1989).
- 168 M. Wuttig, R. Franchy, and H. Ibach, Surf. Sci. **213**, 103 (1989).
- 169 H. C. Zeng, R. A. McFarlane, and K. A. R. Mitchell, Surf. Sci. **208**, L7 (1989).
- 170 X. Duan, O. Warschkow, A. Soon, *et al.*, Phys. Rev. B **81** (2010).

- 171 J. K. Barton, A. A. Vertegel, E. W. Bohannon, *et al.*, Chem. Mater. **13**, 952 (2001).
- 172 G. Simons and H. Wang, *Single Crystal Elastic Constants and Calculated Aggregate Properties* (MIT Press, Cambridge, MA, 1977).
- 173 R. W. Balluffi and A. P. Sutton, Intergranular and Interphase Boundaries in Materials, Part 1, **207**, 1 (1996).
- 174 Y. Mishin, M. J. Mehl, D. A. Papaconstantopoulos, *et al.*, Phys. Rev. B **63**, 224106 (2001).
- 175 M. M. Beg and S. M. Shapiro, Phys. Rev. B **13**, 1728 (1976).
- 176 J. Hallberg and R. C. Hanson, Phys. Status Solidi **42**, 305 (1970).
- 177 V. E. Henrich and P. A. Cox, *The Surface Science of Metal Oxides* (Cambridge University Press, New York, 1994).
- 178 N. P. Padture, M. Gell, and E. H. Jordan, Science **296**, 280 (2002).
- 179 B. C. Gates, Mater. Chem. **245**, 301 (1995).
- 180 C. T. Campbell, Surf. Sci. Rep. **27**, 1 (1997).
- 181 J. A. Kelber, Surf. Sci. Rep. **62**, 271 (2007).
- 182 B. Hinnemann and E. A. Carter, J. Phys. Chem. C **111**, 7105 (2007).
- 183 T. J. Campbell, G. Aral, S. Ogata, *et al.*, Phys. Rev. B **71** (2005).
- 184 D. J. Siegel, L. G. Hector, and J. B. Adams, Phys. Rev. B **65** (2002).
- 185 W. Zhang and J. R. Smith, Phys. Rev. Lett. **85**, 3225 (2000).
- 186 J. R. Smith and W. Zhang, Acta Mater. **48**, 4395 (2000).
- 187 T. Campbell, R. K. Kalia, A. Nakano, *et al.*, Phys. Rev. Lett. **82**, 4866 (1999).
- 188 D. L. Medlin, K. F. McCarty, R. Q. Hwang, *et al.*, Thin Solid Films **299**, 110 (1997).
- 189 G. Paglia, A. L. Rohl, C. E. Buckley, *et al.*, J. Mater. Chem. **11**, 3310 (2001).
- 190 G. Paglia, A. L. Rohl, C. E. Buckley, *et al.*, Phys. Rev. B **71** (2005).

- 191 P. Lamparter and R. Kniep, *Physica B* **234**, 405 (1997).
- 192 M. Vermeersch, R. Sporken, P. Lambin, *et al.*, *Surf. Sci.* **235**, 5 (1990).
- 193 U. Schroder, *Solid State Comm.* **4**, 347 (1966).
- 194 N. D. M. Hine, K. Frensch, W. M. C. Foulkes, *et al.*, *Phys. Rev. B* **79** (2009).
- 195 R. Di Felice and J. E. Northrup, *Phys. Rev. B* **60**, R16287 (1999).
- 196 L. E. Murr, *Interfacial Phenomena in Metals and Alloys* (Addison-Wesley, Reading, MA, 1975).
- 197 K. H. Westmaco and R. L. Peck, *Philo. Mag.* **23**, 611 (1971).
- 198 R. H. Rautioaho, *Phys. Status Solidi B* **112**, 83 (1982).
- 199 W. H. Gitzen, *Alumina as a Ceramic Material* (The American Ceramic Society, Columbus, OH, 1970).
- 200 J. B. Wachtman, W. E. Tefft, D. G. Lam, *et al.*, *J. Res. Natl. Bur. Stnds. A.* **64**, 213 (1960).
- 201 M. I. Baskes and R. A. Johnson, *Modeling and Simulation in Materials Science and Engineering* **2**, 147 (1994).
- 202 M. I. Baskes, S. G. Srinivasan, S. M. Valone, *et al.*, *Phys. Rev. B* **75** (2007).
- 203 W. H. Press, *Numerical Recipes in FORTRAN 77: The Art of Scientific Computing* (Cambridge University Press, Cambridge, 1992).

## BIOGRAPHICAL SKETCH

Bryce David Devine received a bachelor's degree in chemistry from Boston University in 1992. Following his undergraduate education, he was commissioned as an officer in the US Army and served 5 years as a paratrooper in Ft. Richardson, Alaska. After his military service, Bryce worked as an industrial chemist for several years, during which time he was awarded three patents for his work on metal oxide coatings. In the fall 2004, Bryce was afforded the opportunity to pursue his graduate studies at the University of Florida under the advisement of Prof. Susan Sinnott. He earned his PhD in materials science and engineering in December 2010.